Numerical simulation and modelling of phase-change materials

Aina Rakotondrandisa

Normandie Université

THÈSE

Pour obtenir le diplôme de doctorat

Spécialité MATHÉMATIQUES APPLIQUÉES

Préparée au sein de l'Université de Rouen Normandie

Modélisation et simulation numérique de matériaux à changement de phase

Présentée et soutenue par
Aina RAKOTONDRANDISA

Thèse soutenue publiquement le 27 / 09 / 2019 devant le jury composé de		
M. Ionut DANAILA	Professeur / Université de Rouen Normandie	Directeur de thèse
M. Zakaria BELHACHMI	Professeur / Université de Haute Alsace	Rapporteur
M. Patrick Le QUÉRÉ	Directeur de Recherche C.N.R.S / LIMSI	Rapporteur
M. Pascal FREY	Professeur / Sorbonne Université	Examinateur
M. Frédéric HECHT	Professeur / Sorbonne Université	Examinateur
M. Stéphane Le MASSON	PhD-HDR / Orange Labs	Examinateur
Mme. Luminita DANAILA	Professeur / Université de Rouen Normandie	Examinatrice
M. Francky LUDDENS	Maître de Conférence / Université de Rouen Normandie	Membre invité

Thèse dirigée par Ionut DANAILA, Laboratoire de Mathématiques Raphaël Salem

UNIVERSITÉ DE ROUEN NORMANDIE

MIIS

LMRS

Remerciements

C'est avec une grande émotion que j'adresse premièrement mes remerciements à mon directeur de thèse, Ionut Danaila. Je tiens à lui exprimer ma gratitude pour la confiance, la patience, ainsi que l'intérêt qu'il m'a témoigné tout au long de ce travail de thèse. L'enthousiasme et le dynamisme qu'il a su communiquer au sein du groupe calcul scientifique ont été pour moi des sources de motivations. J'ai beaucoup appris au-delà de l'aspect scientifique par la rigueur qu'il a su transmettre : "on vise la qualité professionnelle en toute chose"! Merci de m'avoir accordé cette opportunité.

Ma reconnaissance va aussi à Zakaria Belhachmi et Patrick Le Quéré d'avoir accepté d'être les rapporteurs de ma thèse, ainsi qu'à Pascal Frey, Frédéric Hecht, Stéphane Le Masson, Luminita Danaila, et Francky Luddens, qui m'ont fait l'honneur de participer au jury de cette thèse et de porter une attention avisée sur mon travail.

Je profite également de ce moment pour remercier le projet M2NUM [1] pour le financement des trois ans de travaux de thèse. Cela m'a offert l'opportunité d'assister à de nombreux congrès et conférences nationaux et internationaux. Merci également au centre de calcul régional CRIANN [2] d'avoir accordé des heures de calculs, indispensables notamment pour les calculs tri-dimensionnels.

Je témoigne de ma reconnaissance à Pierre Calka, le directeur du laboratoire LMRS [3]. Sans son accord et sa confiance, ce travail n'aurait pu être mené à son terme. Merci au laboratoire pour le financement de nombreux déplacements pour ne citer que "l'atelier de résolution de problèmes industriels" à Montréal ou encore "l'école de printemps inter-disciplinaire en simulation numérique et optimisations de code" à Lyon. Merci à tout le personnel administratif : Edwige Auvray, Hamed Smail, Sandrine Halé, Marc Jolly, et Saada Benamar, pour leur coopération et leur aide au quotidien. Merci à l'équipe du midi, pour votre bonne humeur et les moments conviviaux. Un grand merci spécialement à toute l'équipe calcul scientifique, ceux qui y sont encore, ceux qui étaient de passage, ou ceux qui sont partis mais que j'ai pu côtoyer durant cette thèse : Francky Luddens, Guillaume Vergez, Lei Bian, Corentin Lothodé, et Geoges Sadaka. Je tiens à mentionner spécialement Georges Sadaka pour le grand travail qu'il a effectué sur la partie 3D du code. J'ai conscience d'avoir eu la chance de travailler auprès de personnes exceptionnelles - pas que sur le plan scientifique.

Je remercie aussi les développeurs du logiciel éléments finis FreeFem++ et des libraires FFDDM et HPDDM, Frédéric Hecht, Pierre-Henry Tournier et Pierre Jolivet, pour toute l'aide dont ils ont fait preuve pour me guider dans l'utilisation du logiciel.

J'adresse en particulier mes remerciements à Luminita Danaila, que j'ai eu l'opportunité d'avoir en cours de mécanique des fluides et de turbulence depuis les années de Master à l'Université de Rouen Normandie, pour sa grande pédagogie et sa gentillesse. Je suis reconnaissant pour toute la patience et la compréhension dont elle a fait preuve, notamment durant la rédaction du papier sur le cycle complet fusion-solidification.

Je tiens aussi à exprimer ma gratitude à l'église protestante malgache de Rouen (FPMA) pour leur soutien indéfectible depuis ces sept années que je suis à Rouen. Merci pour l'amour

[1] **M**odélisation **M**athématique: applications et simulations **NUM**ériques
[2] **C**entre **R**égional **I**nformatique et d'**A**pplications **N**umériques de **N**ormandie
[3] **L**aboratoire de **M**athématiques **R**aphaël **S**alem

que vous avez témoigné envers moi et ma famille ainsi que pour vos prières.

Un proverbe malgache dit : ”Ny hazo no vanon-ko lakana, ny tany naniriany no tsara” *(si l'arbre est bon pour en faire une pirogue, c'est parce qu'il a poussé sur une bonne terre)*. J'emprunte ce proverbe pour remercier toute ma famille, la terre qui m'a façonné et qui m'a éduqué, à commencer par Dada sy Neny. Merci pour les sacrifices que vous avez faits pour que je puisse effectuer et terminer mes études : les sacrifices financiers mais aussi les sacrifices liés à la distance (on ne s'est revu qu'une fois sur douze ans). Je suis entièrement reconnaissant aussi envers toute ma famille de La Réunion, d'Évreux, de Montpellier, et de Grand-Couronne, qui m'ont hébergé depuis ma première année à l'université jusqu'au début de la thèse. Je n'oublie pas non plus ma belle famille qui a témoigné de son soutien inconditionnel durant cette thèse. Merci pour tout!

Enfin, c'est à ma femme Mioratiana et mon fils Manantsoa, que je dédie ce travail de thèse. Aucun mot ne suffira pour vous exprimer toute ma reconnaissance. Je vous aime!

Aina Rakotondrandisa

Rouen, mercredi 02 octobre 2019

Contents

1 Introduction

1.1 Green energy management and phase-change materials

Climate change is more than ever experienced in our daily life: irregular melt of sea, deterioration of ozone layer, non-seasonal precipitations, etc. Our dependency on fossil fuels during the last decades for energy production have caused severe environmental issues. As shown in Fig. 1.1a, coal and natural gas were the main energy sources for electricity production in the world in 2017 (Dudley, 2018). Today, we must face with the fact that these fossil fuels are going to an end and admit that their large utilization has induced considerable impact on our environment.

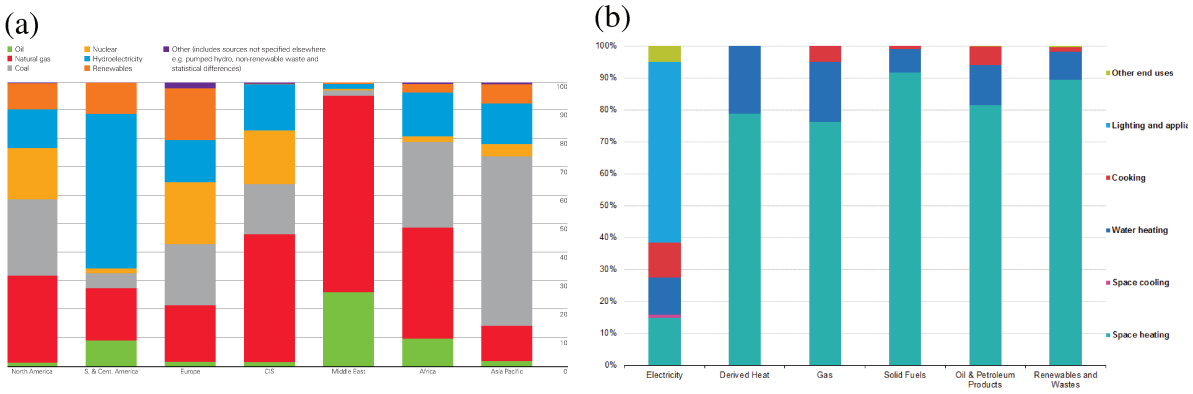

Figure 1.1: (a) Electricity generation by different energy sources in 2017 on different continents by Dudley (2018). (b) Energy use distribution in residential buildings in Europe by Dudley (2018).

Research on environment-friendly energy sources, such as biomass, wind or solar, have attracted many considerations recently. Even though solar or wind energy are now operational, their main drawback remains the gap between their availability and the consumer's demand. Solar energy is not available during the night for example, while wind energy is intermittent over the year. The energy demand varies with time and the energy suppliers have to deal with this constraint.

A current solution to deal with this discrepancies between availability and demand is the use of energy storage systems. The idea is to store the available energy in one form or another and release it latter for a particular need, since energy availability and demand rarely concur. The energy storage process is a crucial point for renewable and sustainable energy. The latter can be divided into five classes: magnetic, biological, chemical, mechanical and thermal energy storages. The main feature of the aforementioned energy storage technologies relies on energy charging and discharging process. In most cases however, thermal energy is the energy form widely used. Even the electricity production is monitored by heat,

since it generates high temperatures and pressures. Storing thermal energy is hence an efficient and fundamental way to store the energy. This can be realised by rising a substance's temperature (sensible heat energy storage) or by changing a substance's phase (latent heat energy storage).

To this end, research on passive heat storage systems has generated many studies lastly, namely on latent heat energy storage like Phase Change Material (PCM). PCMs are used to store heat during the melting of the material and release later the stored energy during the solidification process. At the present time, the latent heat storage technologies are proven as an effective solution to decrease the use of fossil fuel and in the same time to increase the efficiency of energy usage.

Aside from energy storage technologies, PCMs are also widely used in building applications, to decrease temperature fluctuations. The latest announcement of the French ministry of ecological transition, detailing the repartition of the energy consumption in different domains, indicates that more than 35% of the total energy is consumed by residential and commercial buildings. Details about energy consumptions in 2017, reported by the French ministry of ecological transition are shown in Tab. 1.1.

Agriculture	Buildings	Industry	Transportation	Other
4.5	41.8	26	43.8	4.5

Table 1.1: Energy consumed by different domains in France in 2017, in million tonnes of oil equivalent. French ministry of ecological transition (Ministère de la transition écologique et solidaire, 2018).

More than 60% of the total energy consumption in the residential sector is used to space heating (see Fig. 1.1b). Research towards an energy-efficient building to reduce heating and cooling demands is of principal interest nowadays. Taking advantage of the high value of the latent heat of solid-liquid transformations, PCMs are extensively encountered in building's thermal regulation to reduce overheating. In summer, PCMs are used to absorb the excessive solar radiation heat and maintain a bracing indoor ambience. PCM with a temperature of fusion close to the ambient temperature is generally used to ensure melting during the daytime and solidification during the night-time. During winter however, PCMs can be used to store heat generated by electrical heating system during the night and then release it in the daytime.

PCMs are also encountered in other applications ranging from metal casting and passive temperature control devices for modern portable electronics, to food freezing and cryosurgery. In many of these applications, the choice of an appropriate material for a specific end depends of many criteria, such as the operating temperature range, the thermal conductivity, the cost, etc. They are generally classified into three classes: organic, inorganic and eutectic. A target application area for some PCMs is drawn in Tab. 1.2. The main operating temperature range can be assorted in three groups of melting temperature range. First, 0 to 65^oC for thermal storage used in domestic heating/cooling or for thermal storage of solar energy. Paraffins and water are used for such applications. Second, 80 to 120^oC for the cooling of systems with temperature of fusion less than 120^oC. Finally, temperatures greater than 150^oC for the heat storage in solar power plants based on parabolic trough collectors and direct steam generation. For more details about these applications, see the review by Agyenim et al. (2010).

Melting and solidification are also fundamental processes in geophysical problem such as Earth's mantle formations, lava lakes (Davaille and Jaupart, 1993), thermal convection in magma chambers (Brandeis and Marsh, 1989) or ice-melt lakes (Polashenski et al., 2012). Ice-melt ponds that form during the summer season in the Arctic are known for example to display natural convection coupled

Temperature range	PCM	Target application area
0 - 65 ^oC	Paraffins (-3 to 64 ^oC), water / ice (0 ^oC), stearic acide (41 - 43 ^oC), n-octadecane (27.7 ^oC)	Storage for domestic heating/-cooling. Passive storage in bio-climatic building/architecture. Thermal storage of solar energy. Application in off-peak electricity for cooling and heating. Protection of electrical devices.
80 - 120 ^oC	Erythritol (117.7 ^oC), RT100 (99 ^oC), $MgCl_2\,6H_2O$ (116.7 ^oC)	Storage for the hot-side of $LiBr/H_2O$ absorption cooling system with generator temperature requirements of less than 120 ^{o}C
$>$ 150 ^oC	$NaNO_3$ (310 ^oC), KNO_3 (330 ^oC), $NaOH$ (318 ^oC), KOH (380 ^oC), $ZnCl_2$ (280 ^oC)	Storage for solar power plants based on parabolic trough collectors and direct steam generation.

Table 1.2: Target application area for some PCMs studied in the literature (Agyenim et al., 2010).

to a phase-change process on the bottom side (Polashenski et al., 2012; Esfahani et al., 2018). In this case, Rayleigh-Bénard like convection cells are observed in the liquid phase.

The solid-liquid phase-change phenomenon is known to involve complex processes. It couples the natural convection in the liquid phase induced by the buoyancy force to the non-linear evolution of the phase-change interface and the heat transfer process, which could be different from one configuration to another. The coupling of all these physical phenomena induces a strong non-linear process in the solid-liquid problems, difficult to analyse, excepting for simple and ideal test cases. As an example, Fig. 1.2 shows the experimental investigation of the melting of n-octadecane inside a transparent brick, used as a smart material to control the indoor environment of a building (Gong et al., 2015). The investigated material is heated from the right and melts consequently from the right to the left. Figs. 1.2a and 1.2b display the evolution of the liquid fraction and the vector field in the fluid obtained by particle image velocimetry (PIV) method. Capturing accurately the non-linear evolution of the solid-liquid interface and the strong convection in the melting PCM is clearly a challenging numerical task. Furthermore, the existence of boundary layers near the walls and the interface suggests that the mesh resolution should adapt to capture these structures.

1.2 Theoretical and experimental studies of phase-change systems

Solid-liquid phase-change problems have attracted attention since the study of crust formation of earth by Lamé and Clapeyron (1831) or the ice formation problem by Stefan (1889). From a mathematical point of view, the phase transition is referred to a moving boundary problem. The Stefan problem considers a linear evolution of the interface by assuming only conductive heat transfer. Under this as-

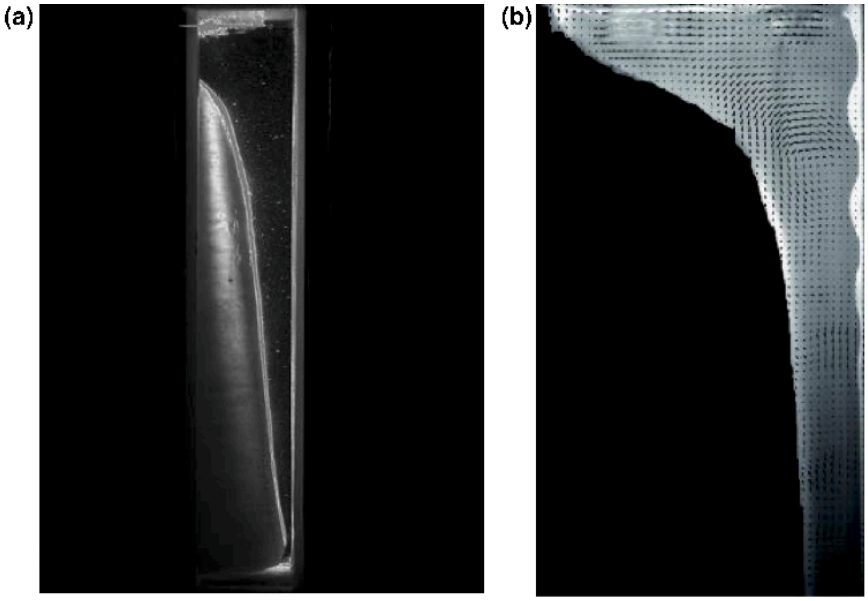

Figure 1.2: Experimental observation of the melting of n-octadecane within a transparent brick of plexiglas heated vertically from the right: (a) melted fraction (b) velocity field in the liquid region obtained by particle image velocimetry (PIV) method (Gong et al., 2015).

sumption, the existence and the uniqueness of the solution for the one-dimensional problem was proven by Rubinstein (1947) using constant properties. For a historical review detailing the evolution of the Stefan problem and the progressive consideration of convection in the liquid, one can refer to Yao and Prusa (1989). Over the past 30 years, solid-liquid phase-change involving natural convection has been widely studied. Rectangular and cylindrical geometries were the most investigated configurations. Okada (1984); Gau et al. (1983); Gong et al. (2015) have investigated experimentally the melting of n-octadecane and gallium PCMs inside rectangular containers. Ho and Viskanta (1984); Liu and Groulx (2014); Omojaro and Breitkopf (2017) have studied experimentally the melting of different paraffins, within cylindrical enclosures. These experimental investigations have been extensively used for numerical validations (see Bertrand et al. (1999); Gobin and Le Quéré (2000); Wang et al. (2010b); Danaila et al. (2014); Rakotondrandisa et al. (2019)) and have permitted a better comprehension of the physical phenomena that occur during melting and solidification, mainly the heat transfer process. The experimental work of Okada (1984) has permitted for example to formulate correlations for the variation of dimensionless thermal energy stored as latent heat. Later, Ho and Viskanta (1984) have analyzed the solid-liquid interface position for different configurations and Jany and Bejan (1988) have suggested Nu-$\mathcal{R}a$ correlations through a scaling analysis. Bejan (1989) gathered the previous observations and described analytically the solid-liquid melting process in the case of a vertical heating. Le Quéré and Gobin (1999) have performed instability analysis during the melting of low and large Prandtl numbers. Gallium and n-octadecane were the most investigated materials. Besides, their physical properties are equal in both liquid and solid phases (differences less than 3%). Gallium and n-octadecane melt near the room temperature, making them the preferred materials for experimentally investigating melting and solidification of low or high Prandtl-number PCMs.

The previously mentioned works were mostly focused on studying separately melting or solidification and only recently alternate melting and solidification cycles were addressed (Wang et al., 2010b; Rakotondrandisa et al., 2019). Prior to these studies on complete cycles, periodic melting and solidi-

fication problems were the most studied in the literature. Ho and Chu (1993) and Voller et al. (1996) studied numerically periodic melting in square enclosures. Recently, Hosseini et al. (2014) studied melting and solidification of a cylindrical PCM during charging and discharging processes and Chabot and Gosselin (2017) studied analytically the effect of an alternate heating and cooling in a cylindrical PCM, with periodical boundary conditions. We have also contributed recently to the understanding of the governing mechanism during the melting and the solidification process in the paper Rakotondrandisa et al. (2019). We analysed in detail the difference between solidification occuring after a partial melting or a complete melting by providing temporal evolutions of solid-liquid interface, liquid fraction, Nusselt number and accumulated heat input.

While the literature about melting and solidification of PCM heated from the side is very abundant, research on melting of PCM heated from below is quite rare. Diaz and Viskanta (1984); Hale and Viskanta (1980) have studied experimentally the solid-liquid interface morphology of the PCM during basal heating. Gong and Mujumdar (1998) studied numerically the flow and heat transfer during the melting of pure n-octadecane in a rectangular cavity heated from below. Recent numerical simulations have investigated different boundary conditions, such as periodic configurations along the horizontal axis (Esfahani et al., 2018; Madruga and Curbelo, 2018; Favier et al., 2019) or wavy surface in a rectangular cavity heated from below (Kousksou et al., 2014). Concerning theoretical works, Vasil and Proctor (2011); Favier et al. (2019) have studied the hydrodynamic instabilities at the onset of convection and compared their observations with the classical Rayleigh-Bénard instability mechanism (Chandrasekhar, 2013). Favier et al. (2019) have focused on the effect of the non-planar topography of the interface on the convection flow. On the other hand, Gong and Mujumdar (1998); Esfahani et al. (2018); Madruga and Curbelo (2018) mostly focused on global quantities, such as the heat flux and statistical properties of the interface.

1.3 Physical models for phase-change materials

Temperature gradients induce buoyancy forces in the liquid (melted) phase and generate a significant convective flow. The appropriate mathematical description of the liquid phase is thus the usual model for the natural convection flow: the incompressible Navier-Stokes system of equations with Boussinesq approximation for thermal (buoyancy) effects (*e. g.* Viskanta (1985)). In this model, the energy conservation equation is written as a convection-diffusion equation for the temperature. In the solid phase, conduction is the main phenomenon and the appropriate model is the classical heat equation. The main modelling difficulty is to link these two models by taking into account the separation of the two phases by a sharp interface, across which thermodynamic properties are discontinuous.

We offer in this section a description of the two main approaches suggested in the literature to deal with solid-liquid phase change problem. For a comprehensive review of models for phase-change problems with convection, see Kowalewski and Gobin (2004). Note that a different category of models was recently suggested in the literature, based on the Lattice Boltzmann Method (Luo et al., 2015; Gong et al., 2015) or meshless methods Atluri and Shen (2002). Such methods based on non-deterministic models are not discussed in this introduction.

A first modelling approach, usually referred to as the multi-domain (or deforming-grid) method, is based on the classical Stefan two-phase model. Solid and liquid domains are separated and the corresponding conservation equations are solved in each domain. Boundary conditions at the interface between domains are obtained by imposing the Stefan condition (balance of heat fluxes at the interface). The position of the solid-liquid interface is tracked and moved explicitly using either *front tracking* or *front fixing* methods. The former method uses deforming grids to reconstruct the interface, while

the latter is based on a time-depending coordinate transform, mapping the physical domain into a fixed computational domain. For a detailed description of these methods, see *e. g.* Sparrow et al. (1977); Unverdi and Tryggvason (1992); Gupta (2000); Tenchev et al. (2005). The main drawback of deforming-grid methods is their algorithmic complexity, which makes difficult to accurately capture solid-liquid interfaces of complicated shape or structure (*e. g.* with mushy regions between solid and liquid phases). Configurations with multiple interacting interfaces are also difficult to simulate with these methods (see also Stella and Giangi (2004)).

The second modelling approach avoids to impose explicitly the Stefan condition at the solid-liquid interface and therefore uses a single-domain (or fixed-grid) model. The same system of equations is solved in both liquid and solid phases. The energy balance at the interface is implicitly taken into account by the model. Consequently, the position of the interface is obtained a posteriori by post-processing the computed temperature field. Phase-field methods (Fabbri and Voller, 1997) and enthalpy methods (Voller and Prakash, 1987; Cao et al., 1989) are the most commonly used single-domain models. In phase-field methods, a supplementary partial differential equation for the evolution of the order parameter (a continuous variable taking the value 0 in the solid and 1 in the liquid) has to be solved, coupled with the conservation laws (Shyy et al., 1996). This new equation is model dependent and its numerical solution could lead to diffuse solid-liquid interfaces. For recent contributions in this area, see Boettinger et al. (2002); Singer-Loginova and Singer (2008); Favier et al. (2019). We focus below on enthalpy methods, which are the most widely used single-domain models due to their algorithmic simplicity.

The main idea behind enthalpy models is to formulate the energy conservation law in terms of enthalpy and temperature, and include latent heat effects in the definition of the enthalpy. The obtained equation applies to both liquid and solid phases and implicitly takes into account the separation of the phases. Another advantage of enthalpy methods, when compared to previously described models, is to remove the limitation of the phase-change occurring at a fixed temperature. The presence of mushy regions can be easily modelled with these methods. Two types of formulations of enthalpy methods exist in the literature, depending on the main variable used to solve the energy equation: enthalpy or temperature-based methods.

In enthalpy-based formulations the main variable is the enthalpy (Eyres et al., 1946; Rose, 1960; Bhattacharya et al., 2014). Temperature is computed from the temperature-enthalpy coupling model. An iterative loop is necessary to solve the energy equation, formulated with both enthalpy and temperature variables. For a review of different iterative techniques to solve the energy equation, see Voller (1996). A second variety of enthalpy-based formulations consists in rewriting the energy equation with enthalpy terms only (Rady and Mohanty, 1996; Hannoun et al., 2003).

In temperature-based formulations, the energy equation is formulated in terms of temperature only. The latent heat is treated either by deriving an apparent heat capacity coefficient to define the total enthalpy (Morgan et al., 1978; Chiesa and Guthrie, 1974; Gau and Viskanta, 1984) or by introducing a source term in the energy equation (Voller, 1996; Swaminathan and Voller, 1997). Advantages and drawbacks of each approach are discussed in detail in König-Haagen et al. (2017).

1.4 Numerical approaches

Single-domain methods are very appealing for numerical implementations. The same system of equations is solved in the entire computational domain, making possible algorithmic or computer-architecture optimisations. If enthalpy models offer an elegant solution to deal with the same energy conservation

equation in both phases, a last modelling problem has to be solved. It concerns the extension of the Navier-Stokes-Boussinesq equations from the liquid to the solid phase. Different techniques to bring the velocity to zero in the solid region were suggested.

The most straightforward is the switch-off technique, which decouples solid and liquid computational points and overwrites the value of the velocity by setting it to zero in the solid region. Different implementations of this technique with finite-volume methods are presented in Ma and Zhang (2006); Wang et al. (2010a).

In variable viscosity techniques (Gartling, 1980; Voller et al., 1987; Cao and Faghri, 1990), the fluid viscosity depends on the temperature and is artificially increased to huge values in the solid regions through a regularisation or mushy zone. To avoid blow-up or numerical inconsistencies, the large gradients of viscosity must be correctly resolved in the mushy region. This is naturally achieved in finite-element methods with dynamical mesh adaptivity (Danaila et al., 2014), while in finite-volume methods with fixed grids, the time step has to be adapted to the space resolution (Ma and Zhang, 2006). Versions of the variable viscosity approach suggested in Danaila et al. (2014) were further studied by Aldbaissy et al. (2018); Woodfield et al. (2019) and implemented in a different finite-element framework (FEniCS) by Zimmerman and Kowalski (2018).

A third technique used to ensure a zero velocity field in the solid phase is the so-called enthalpy-porosity model (Brent et al., 1988). A penalisation source term is introduced in the momentum equation to allow the switch from the full Navier-Stokes equations in the liquid phase to a Darcy equation for porous media. The mushy region is thus regarded as a very dense porous medium that sharply brings the velocity to zero in the solid region. The expression of the penalisation source term generally follows the Carman-Kozeny model for the permeability of a porous medium (Hannoun et al., 2003, 2005; Belhamadia et al., 2012), but other mathematically equivalent expressions were suggested (Angot et al., 1999; Favier et al., 2019). Different formulations and implementations of the enthalpy-porosity model are presented in Kowalewski and Rebow (1999); Giangi et al. (2000); Stella and Giangi (2004).

Concerning the space discretization of these models, finite difference (FD) or finite volume (FV) methods are generally used in the literature. When single-mesh models are used, the general strategy to capture the solid-liquid interface is to dramatically increase the mesh resolution in the whole domain. This results in a considerable increase of the computational time, even for two dimensional cases. Hannoun et al. (2003) have reported that the simulation of the melting of tin with a 200×200 fixed grid required $2,400$ CPU hours, 111 runs (restarts), and 3 months of calculation. Dynamical mesh adaptivity becomes in this context a valuable tool to concentrate the grid refinement effort only in regions displaying high gradients of the computed variables (melting-solidification fronts, thermal or viscous boundary layers, recirculation zones).

Finite element (FE) methods offer the possibility to dynamically refine the mesh only in specific regions of the domain. Different FE approaches were suggested, from enthalpy-type methods (*e. g.* Elliott (1987)) to front-tracking methods (*e. g.* Li (1983)). Recently, adaptive FE methods were proposed for classical two-phase Stefan problem (Belhamadia et al., 2004a) using an anisotropic mesh adaptation algorithm based on solution-dependent metrics. The authors extended their algorithm for the three-dimensional simulation of the same problem (Belhamadia et al., 2004b) and showed that the use of locally adapted meshes with strong anisotropy proved to be very effective in reducing the number of computational nodes for such phase-change systems without convection.

To simulate melting or solidification problems with convection, Danaila et al. (2014) recently suggested a dynamical mesh adaptation algorithm based on metrics control and implemented with the FreeFem++ software (Hecht et al., 2007; Hecht, 2012). The advantage of this adaptive finite-element method, which will be also used in the present study, is to make possible, with reasonable computational cost,

the re-meshing of the computational domain at each time step. A very refined discretization of the regularization zone between solid and liquid phases is thus obtained, while regions with low gradients are coarsened in order to balance the overall computational effort.

1.5 Present numerical approach

The present study is based on a single-domain enthalpy-porosity model for solid-liquid phase change problems with convection. For the energy conservation equation, a temperature-based formulation takes into account the latent heat by introducing a discontinuous source term. For the mass and momentum conservation equations, we solve in the entire domain the incompressible Navier-Stokes equations with Boussinesq approximation for buoyancy effects. To bring the velocity to zero in the solid phase, we introduce in the momentum equation a penalty term following the Carman-Kozeny model. The coupled system of momentum and energy equations is integrated in time using a second-order Gear scheme. All the terms are treated implicitly and the resulting discretized equations are solved using a Newton method (Danaila et al., 2014).

The advantage of this formulation is to permit a straightforward implementation of different types of non-linearities. For the space discretization we use Taylor-Hood triangular finite elements, *i. e.* $\mathbb{P}_2$ for the velocity and $\mathbb{P}_1$ for the pressure. Temperature is discretized using $\mathbb{P}_2$ or $\mathbb{P}_1$ finite elements. Discontinuous variables (latent heat, thermal diffusivity, etc) at the solid-liquid interface are regularized through an intermediate artificial mushy region.

Single domain methods require a refined mesh near the interface, where large enthalpy gradients have to be correctly resolved. An optimized dynamical mesh adaptivity algorithm allows us to adapt the mesh every time step and thus accurately capture the evolution of the interface. Mesh adaptivity, a feature of the current method, offers the possibility to deal with complicated phase-change cases, involving multiple solid-liquid interfaces.

There are three main novelties in the present numerical approach, when compared to Danaila et al. (2014):

(i) we use the Carman-Kozeny model to bring the velocity to zero inside the solid phase, instead of a viscosity penalty method (imposing a large value of the viscosity in the solid),

(ii) we increase the time accuracy of the algorithm by replacing the first-order Euler scheme with the second-order Gear (BDF2) scheme (see also Belhamadia et al. (2012)),

(iii) we improve the metric calculation procedure for the mesh adaptivity.

The programs were built and organized as a toolbox for FreeFem++ (Hecht, 2012; Hecht et al., 2007), which is a free software (under LGPL license). FreeFem++ [1] offers a large variety of triangular finite elements (linear and quadratic Lagrangian elements, discontinuous $\mathbb{P}_1$, Raviart-Thomas elements, etc.) to solve partial differential equations. It is an integrated product with its own high level programming language and a syntax close to mathematical formulations, making the implementation of numerical algorithms very easy. Among the features making FreeFem++ an easy-to-use and highly adaptive software we recall the advanced automatic mesh generator, mesh adaptation, problem description by its variational formulation, automatic interpolation of data, colour display on line, postscript printouts, etc. The FreeFem++ programming framework offers the advantage to hide all technical issues related to the implementation of the finite element method. It becomes then easy to use the present toolbox to

[1] FreeFem++ for different OS can be downloaded from `http://www3.freefem.org/`.

code new numerical algorithms for similar problems with phase-change.

1.6 Purpose of the thesis

The purpose of the present work was to investigate numerically solid-liquid phase-change systems. The investigation tool used in this thesis is the open-source software FreeFem++ (Hecht et al., 2007; Hecht, 2012). A high accuracy numerical model using a Newton method with adaptive finite elements is used to simulate phase-change problems with natural convection.

A first numerical investigation of convective phase-change problems using an adaptive finite element method has been carried out by Danaila et al. (2014). Their method solved the Navier-Stokes-Boussinesq equations by the mean of a single domain approach using first order scheme in time. The technique of variable viscosity approach was applied to bring to zero the velocity in the solid phase. The study was focused on two-dimensional square cavity configurations.

A first objective of this thesis was to improve the existing code, developed by the Numerical methods and applications group of the LMRS Laboratory [2], and to organize the program as a toolbox for the software FreeFem++. To this end, the following objectives were addressed:

(i) increase the accuracy by using a second order scheme for the time discretization and $\mathbb{P}_2$ finite elements for the temperature,

(ii) implement a Carman-Kozeny model, in addition to the viscosity-based approach, to bring to zero the velocity in the solid region,

(iii) investigate challenging cases by simulating complex geometries (highly distorted meshes, cylindrical PCM with inner heated tubes) and computationally demanding cases (high Rayleigh numbers),

(iv) simulate a complete melting-solidification cycle of a PCM.

A second objective was to extend the program to three-dimensional configurations. The two dimensional assumption is indeed not valid for high Rayleigh problems, especially for basal melting cases. Moreover, three dimensional adaptive finite element methods for convective melting problems are less present in the literature.

A third objective was to provide a thorough analysis of both melting and solidification processes and compare with numerical results.

1.7 Thesis plan

Chapter 2 sets the mathematical and physical basis of the numerical system used to simulate phase-change problems involving natural convection. We present in detail the incompressible Navier-Stokes-Boussinesq equation and the single-domain approach to solve the same system of equations in the whole domain. The enthalpy method, modeling the phase-change phenomenon, is presented first. The Navier-Stokes equation with Boussinesq approximation to simulate the natural convection in the liquid flow is then recalled. Finally, the non-dimensional system of equations is described in detail, with a discussion on the Carman-Kozeny penalty term in the momentum equation.

[2] http://lmrs-num.math.cnrs.fr

Chapter 3 is devoted to the numerical algorithm for solving the numerical system presented previously. The finite element algorithm that we have developed in this work is first presented: the time integration scheme, the finite element discretization and the Newton method. Then, we describe the mesh adaptivity by metric control, which is a standard function offered by FreeFem++. Some theoretical tests to assess for the accuracy of our numerical method are also presented. The space and time convergence orders are demonstrated using the Burggraf flow and a manufactured solution designed for the incompressible Navier-Stokes equation. The structure of the new finite-element toolbox for the simulation of PCMs is also described. The program architecture and the parameter details are presented. Finally, the domain decomposition method used for large simulations is described.

A first validation of our numerical method is presented in Chapter 4. The capability of the code to deal with linear and non-linear forms of the buoyancy force in the Boussinesq approximation is first tested. Test cases are presented by increasing progressively the difficulty. We simulate first the natural convection of air in square enclosures, differentially heated from the vertical walls. Then, a heated obstacle is added in the center of the domain. Finally, we add the non-linearity in the Boussinesq force to simulate the natural convection of water.

Once the capability of our algorithm to deal with natural convection problems was demonstrated, much more attentions to phase-change problems is paid in Chapter 5. Numerical simulations of melting and solidification of PCM are presented. The melting processes for octadecane and Gallium inside rectangular enclosures are investigated first since they were extensively used for numerical method validations. Their physical properties are approximately equal in both solid and liquid phases. Finally, several PCM container geometries are simulated to prove the robustness of our numerical method. In particular, cylindrical and irregular domains are computed.

A scale correlation analysis is presented in Chapter 6. We compare the behavior of the PCM for lateral and basal heating. The melting of n-octadecane heated from the side is carried out first. Then, numerical results for the melting from below are presented. For both cases, we provide a comprehensive description of the melting process through a scale analysis for a better understanding of the heat transfer mechanism. The time evolution of some physical parameters, such as the Nusselt number, the liquid fraction, the accumulated heat input and the time evolution of the melting are discussed and analysed.

Chapter 7 presents the numerical simulation of a full melting/solidification cycle of a PCM. Two solidification fronts have to be tracked, which makes the case very challenging. A differentially heated cavity case and a circular PCM with inner cooled tube are studied. The influence of the Rayleigh number during the melting and the solidification processes is emphasized, since both cycles are not driven by the same mechanism.

Chapter 8 is devoted to three-dimensional configurations simulated using parallel algorithms. 3D simulations of PCMs are indeed less investigated in the literature.

Finally, Chapter 9 draws the conclusion of this study and some ideas for future developments.

2 Navier-Stokes-Boussinesq and enthalpy-porosity models

We consider a solid-liquid system placed in a 2D or 3D domain Ω of characteristic length L_{ref}. In the following, subscripts s and l will refer to the solid and liquid phases, respectively.

The single domain approach, using the same system of equations in both phases, is described first in detail. The model is based on the Navier-Stokes equations with Boussinesq approximation, which is the natural description of the fluid flow with natural convection. A penalty term is added to the momentum equations to bring the velocity to zero inside the solid region. For the energy conservation equation, an enthalpy-porosity method is used to model the phase change process.

2.1 Enthalpy-porosity model

The phase change process is modeled using an enthalpy method with temperature-based formulation (Voller et al., 1987; Cao et al., 1989; Cao and Faghri, 1990). We start from the classical energy equation:

$$\frac{\partial(\rho h)}{\partial t_\varphi} + \nabla \cdot (\rho h \boldsymbol{U}) - \nabla \cdot (k \nabla T) = 0, \tag{2.1}$$

where t_φ is the physical time, h the enthalpy, ρ the density, $\boldsymbol{U}$ the velocity vector, T the temperature and k the thermal conductivity. The total enthalpy h is transformed as the sum of the sensible heat and the latent heat:

$$h = h_{sen} + h_{lat} = c(T + s(T)), \tag{2.2}$$

with c the local specific heat. The function s is introduced to model the jump of the enthalpy during the solid-liquid transition. For pure materials, s is theoretically a Heaviside step function depending on the temperature: it takes the zero value in the solid region and a large value in the liquid, equal to h_{sl}/c_l, with h_{sl} the latent heat of fusion.

If the phase-change is assumed to occur within a mushy zone defined by a small temperature interval $T \in [T_f - T_\varepsilon, T_f + T_\varepsilon]$ around the temperature of fusion T_f, a model for $s(T)$ is necessary. Linear (Voller et al., 1987; Wang et al., 2010a) or more smooth functions (Danaila et al., 2014) can be used to regularize $s(T)$ and thus model the jump of material properties from solid to liquid. In the current work we use a regularization of all step-functions (latent heat source, specific heat, thermal diffusivity or conductivity) by a continuous and differentiable hyperbolic-tangent function suggested by Danaila et al. (2014).

We assume moreover that the undercooling phenomenon is negligible during the solidification stage (see also Wang et al. (2010b); Kowalewski and Gobin (2004)). The solid-liquid interface is identified by the isoline $T = T_f$, while the Gibbs-Thomson effect due to the surface energy of the solid-liquid interface is assumed to be negligible.

Equation (2.1) can be further simplified by considering the following assumptions:

(i) The density difference between solid and liquid phases is negligible, *i. e.* $\rho_l = \rho_s = \rho$ is constant. We note however that this is not strictly true for all substances, but it serves here as a convenient simplification.

(ii) The regularization zone is narrow and the velocity inside this zone is negligible.

Consequently, the final form of the energy equation is obtained by combining Eqs. (2.2) and (2.1) and neglecting the convection term $\nabla \cdot (cs\boldsymbol{U})$[1]:

$$\frac{\partial (cT)}{\partial t_\varphi} + \nabla \cdot (cT\boldsymbol{U}) - \nabla \cdot \left(\frac{k}{\rho}\nabla T\right) + \frac{\partial (cs)}{\partial t_\varphi} = 0. \tag{2.3}$$

2.2 Navier-Stokes equations with Boussinesq approximation

The natural convection in the liquid part of the system is modeled using the incompressible Navier-Stokes equations, with Boussinesq approximation for buoyancy effects. To make this model valid for both liquid and solid phases, the momentum equation is modified as following:

$$\frac{\partial \boldsymbol{U}}{\partial t_\varphi} + (\boldsymbol{U} \cdot \nabla)\boldsymbol{U} + \frac{1}{\rho}\nabla P - \frac{\mu_l}{\rho}\nabla^2 \boldsymbol{U} + \rho g \boldsymbol{e}_y = A(T)\boldsymbol{U}, \tag{2.4}$$

where P denotes the pressure, μ_l the dynamic viscosity of the liquid (assumed to be constant), and g the gravitational acceleration.

The penalty term $A(T)\boldsymbol{U}$ is artificially introduced in Eq. (2.4) to extend this equation in the solid phase, where the velocity, pressure, viscosity and Boussinesq force are meaningless. Consequently, $A(T)$ is modelled to vanish in the liquid, where the Navier-Stokes-Boussinesq momentum equation is recovered. A large value of $A(T)$ is imposed in the solid, reducing the momentum Eq. (2.4) to $A(T)\boldsymbol{U} = 0$, equivalent to $\boldsymbol{U} = 0$. The exact expression for A will be given in the next section.

The density is assumed to be constant everywhere except for the body force term $\rho g \boldsymbol{e}_y$ in Eq. (2.4). Under the assumption of a small variations of density and temperature, the Boussinesq approximation allows to linearize the density as follows:

$$\rho = \rho_{ref}(1 - \beta(T - T_{ref})), \tag{2.5}$$

with $\beta = -(1/\rho_{ref})(\partial\rho/\partial T)_{\rho_{ref}}$ the thermal expansion coefficient and (ρ_{ref}, T_{ref}) a reference state. It is worth noting that this approximation is valid for $\beta(T - T_{ref})$ considerably smaller than the unity. Therefore, the momentum Eq. (2.4) can be written as

$$\frac{\partial \boldsymbol{U}}{\partial t_\varphi} + (\boldsymbol{U} \cdot \nabla)\boldsymbol{U} + \nabla p - \nu_l \nabla^2 \boldsymbol{U} - f_B(T)\boldsymbol{e}_y = A(T)\boldsymbol{U}, \tag{2.6}$$

where $\nu_l = \mu_l/\rho$ is the kinematic viscosity, $p = (P + \rho_{ref} g y)/\rho_{ref}$ includes the hydrostatic pressure $\rho_{ref} g y$ and $f_B(T) = g\beta(T - T_{ref})$ denotes the buoyancy force.

[1] In the liquid phase, $\nabla \cdot (cs\boldsymbol{U}) = h_{sl}\nabla \cdot \boldsymbol{U} = 0$; in the solid phase, $s = 0$; in the regularization (mushy) region, it is assumed that $\boldsymbol{U} = 0$.

Finally, the conservation of mass in the liquid phase is expressed by the continuity equation in the frame of incompressible fluids:

$$\nabla \cdot \boldsymbol{U} = 0. \tag{2.7}$$

The final system of equations for the single-domain approach is thus:

$$\begin{aligned}
\nabla \cdot \boldsymbol{U} &= 0, && (2.8)\\
\frac{\partial \boldsymbol{U}}{\partial t_\varphi} + (\boldsymbol{U} \cdot \nabla)\boldsymbol{U} + \nabla p - \nu_l \nabla^2 \boldsymbol{U} - f_B(T)\boldsymbol{e}_y - A(T)\boldsymbol{U} &= 0, && (2.9)\\
\frac{\partial (cT)}{\partial t_\varphi} + \nabla \cdot (cT\boldsymbol{U}) - \nabla \cdot \left(\frac{k}{\rho}\nabla T\right) + \frac{\partial (cs)}{\partial t_\varphi} &= 0. && (2.10)
\end{aligned}$$

2.3 Dimensionless system of equations for the single-domain approach

It is convenient to numerically solve a dimensionless form of the previous equations. After choosing a reference length L_{ref} (usually the height of the cavity when a rectangular domain is considered) and a reference state (ρ, V_{ref}, T_{ref}), we can define the following scaling for the space, velocity, temperature and time variables:

$$\boldsymbol{x} = \frac{\boldsymbol{X}}{L_{ref}}\,,\ \boldsymbol{u} = \frac{\boldsymbol{U}}{V_{ref}}\,,\ \theta = \frac{T - T_{ref}}{\delta T}\,,\ t = \frac{V_{ref}}{L_{ref}}\,t_\varphi. \tag{2.11}$$

T_{ref} is the reference temperature and in most cases $T_{ref} = T_f$ (the temperature of fusion), unless otherwise specified. Consequently, the non-dimensional temperature of fusion is set to $\theta_f = 0$. The temperature difference δT, defines a temperature scale, that will be set differently for melting and solidification cases. δT is considered as the representative temperature scale for the natural convection onset in the liquid region. For the classical natural convection problem without phase-change, δT is generally defined as $\delta T = T_h - T_c$ since the flow in the fluid is driven by the temperature difference between the "hot" and the "cold" temperature. However, for the melting PCM, the convection is driven by the temperature difference $\delta T = T_h - T_f$, with T_f the temperature of fusion. As far as the solidification process is concerned, a distinct discussion will be provided in Chapter 7.

The dimensionless system of equations to be solved in both liquid and solid regions can be finally written as:

$$\begin{aligned}
\nabla \cdot \boldsymbol{u} &= 0, && (2.12)\\
\frac{\partial \boldsymbol{u}}{\partial t} + (\boldsymbol{u} \cdot \nabla)\boldsymbol{u} + \nabla p - \frac{1}{\mathcal{R}e}\nabla^2 \boldsymbol{u} - f_B(\theta)\,\boldsymbol{e}_y - A(\theta)\boldsymbol{u} &= 0, && (2.13)\\
\frac{\partial (C\theta)}{\partial t} + \nabla \cdot (C\theta\boldsymbol{u}) - \nabla \cdot \left(\frac{K}{\mathcal{R}e\mathcal{P}r}\nabla\theta\right) + \frac{\partial (CS)}{\partial t} &= 0. && (2.14)
\end{aligned}$$

f_B is the linearised Boussinesq buoyancy force, Re is the Reynolds number relating the inertia forces to the viscous forces, and $\mathcal{P}r$ the Prandtl number expressing the ratio of the molecular momentum and thermal diffusivities:

$$f_B(\theta) = \frac{\mathcal{R}a}{\mathcal{P}r\mathcal{R}e^2}\theta, \quad \mathcal{R}e = \frac{\rho V_{ref} L_{ref}}{\mu_l} = \frac{V_{ref} L_{ref}}{\nu_l}, \quad \mathcal{P}r = \frac{\nu_l}{\alpha_l}, \tag{2.15}$$

with $\alpha = k/(\rho c)$ the thermal diffusivity. In the expression of f_B, the Rayleigh number of the flow, which indicates the relative importance of the buoyancy term with respect to viscous effects, is defined as

$$\mathcal{R}a = \frac{g\beta L_{ref}^3 \delta T}{\nu_l \alpha_l}. \tag{2.16}$$

If previous non-dimensional numbers are pertinent only in the liquid phase, the non-dimensional conductivity and specific heat are defined in both phases

$$K(\theta) = \frac{k}{k_l} = \begin{cases} 1, & \theta \geq \theta_f, \\ k_s/k_l, & \theta < \theta_f. \end{cases}, \; C(\theta) = \frac{c}{c_l} = \begin{cases} 1, & \theta \geq \theta_f, \\ c_s/c_l, & \theta < \theta_f. \end{cases} \tag{2.17}$$

The non-dimensional function $S = s/s_l$ in the energy Eq. (2.14) takes a similar non-dimensional form:

$$S(\theta) = \frac{s}{s_l} = \begin{cases} \dfrac{h_{sl}/c_l}{\delta T} = \dfrac{1}{Ste}, & \theta \geq \theta_f, \\ 0, & \theta < \theta_f, \end{cases} \tag{2.18}$$

with Ste the Stefan number.

Discontinuous step-functions defined in Eqs. (2.17) and (2.18) are replaced by continuous and differentiable hyperbolic-tangent functions, generically defined for all θ by the formula (Danaila et al., 2014)

$$F(\theta; a_r, \theta_r, R_r) = f_l + \frac{f_s - f_l}{2}\left\{1 + \tanh\left(a_r\left(\frac{\theta_r - \theta}{R_r}\right)\right)\right\}, \tag{2.19}$$

where f_l, f_s are the imposed values in the liquid and solid phases, a_r a smoothing parameter, θ_r the central value (around which we regularize), and R_r the smoothing radius. For example, we use for the non-dimensional source term in Eq. (2.14) the following regularisation over the artificial mushy region $\theta \in [-\varepsilon, \varepsilon]$:

$$S(\theta) = \frac{1}{\mathcal{S}te} - \frac{1}{2\,\mathcal{S}te}\left\{1 + \tanh\left(\frac{\theta_s - \theta}{R_s}\right)\right\}, \tag{2.20}$$

with $\theta_s = \theta_f = 0$ and $R_s = \varepsilon$ for the melting case.

Finally, the penalty term in the momentum Eq. (2.13) is derived from the Darcy's law, by modeling the fluid flow within the mushy region as a flow through a porous medium. In fact, the Darcy's law states that the velocity of flow in porous medium is proportional to the pressure gradient:

$$\boldsymbol{u} = -\frac{\zeta^*}{\mu}\boldsymbol{\nabla} p. \tag{2.21}$$

where ζ^* is the permeability, which is a function of the porosity. As the porosity decreases, the permeability (and the velocity) also decreases, down to the limiting value of zero when the mushy zone becomes completely solid. This behavior can be accounted in a numerical model by adding a source term $A\boldsymbol{u}$ in the momentum equation. The well-known equation derived from the Darcy law is the Carman-Kozeny model:

$$\nabla p = -\frac{C_{\text{CK}}(1-\lambda)^2}{\lambda^3}\boldsymbol{u}. \tag{2.22}$$

Consequently, A takes the form (Belhamadia et al., 2012; Kheirabadi and Groulx, 2015)

$$A(\theta) = -\frac{C_{\text{CK}}(1 - L_f(\theta))^2}{L_f(\theta)^3 + b}, \tag{2.23}$$

where $L_f(\theta)$ is the local liquid fraction, which is 1 in the fluid region and 0 in the solid. L_f is regularized inside the artificial mushy-region using a hyperbolic-tangent similar to Eq. (2.20). The Carman-Kozeny constant C_{CK} is set to a large value (as discussed below) and the constant $b = 10^{-6}$ is introduced to avoid divisions by zero.

2.4 Boundary layer approximation and scale analysis

Regardless to the practical use of PCM (energy storage, building insulation, or for other purposes), one would necessarily assess the heat transfer during the phase-change process. It was extensively proven that the convective heat transfer plays a significant role during the melting stage. Therefore, before solving numerically Eqs. (2.12) - (2.14), we first rely on a scale analysis to predict theoretically the fluid flow and heat transfer patterns that can develop in the fluid part. The idea behind the scaling analysis is to identify the proper scales of the phenomenon, in order to understand the evolution of the heat transfer and the melting rate. We consider only the liquid phase without phase-change, inside a two-dimensional enclosure of height H filled with Newtonian fluid, differentially heated from the vertical walls and insulated at the horizontal walls. A homogeneous Dirichlet boundary condition is prescribed for the velocity. One may refer to the book by Bejan (2013) for a more detailed presentation.

Since no external force is applied to our system, the fluid flow is mainly driven by natural convection, induced by the temperature difference from the vertical walls. The heat transfer through the fluid layer immediately adjacent to the wall is assumed to be driven by pure conduction. We therefore define the average Nusselt number to quantify the heat transfer rate at the hot wall (placed at $x = 0$):

$$\mathcal{N}u = -\int_0^1 \left.\frac{\partial\theta}{\partial x}\right|_{x=0} dy. \tag{2.24}$$

When a steady state could be reached, the fluid near each sidewall is characterized by two boundary layers: a thermal boundary layer of thickness δ_θ and a viscous boundary layer of thickness δ_ν. The boundary layer approximation assumes that the flow and the energy transfer are restricted predominantly to the boundary layer region. The main consequences of the boundary layer approximation are that:

(i) the normal part of the momentum has a negligible importance,

(ii) the downstream diffusion terms in the momentum and energy equations are neglected in comparison with the normal diffusion terms,

(iii) the pressure distribution is purely hydrostatic,

(iv) the thermal and the viscous boundary layer thickness are related by following expression: $\delta_\nu/\delta_\theta = o\left(\mathcal{P}r^{1/2}\right)$.

The scaling laws suggested by Bejan (2013) are presented in Fig. 2.1, and rely on boundary layer approximation:

$$\delta_T \sim \begin{cases} H\mathcal{R}a^{-1/4} & \text{if } \mathcal{P}r \gg 1, \\ H\mathcal{P}r^{-1/4}\mathcal{R}a^{-1/4} & \text{if } \mathcal{P}r \ll 1. \end{cases} \tag{2.25}$$

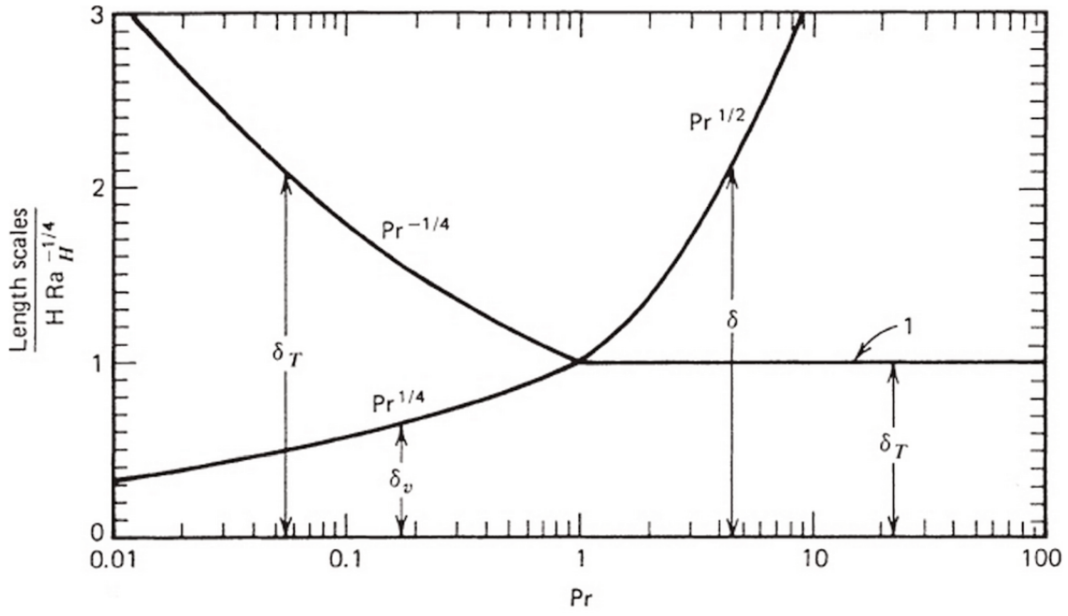

Figure 2.1: Thermal and viscous boundary layer thickness functions of the Prandtl number (Bejan, 2013).

Since the Nusselt number (2.24) scales as H/δ_θ, Bejan (2013) suggested the following $\mathcal{N}u - \mathcal{R}a$ correlations:

$$\mathcal{N}u \sim \begin{cases} \mathcal{R}a^{1/4} & \text{if } \mathcal{P}r \gg 1, \\ \mathcal{P}r^{1/4}\mathcal{R}a^{1/4} & \text{if } \mathcal{P}r \ll 1. \end{cases} \tag{2.26}$$

The correlation (2.25) is useful to estimate the scale of the boundary layer for the mesh adaptivity, since the minimum edge length should allow to capture the smaller length scale in the flow. For low-Prandtl fluids, the viscous boundary layer is thinner than the thermal boundary layer, and conversely, the thermal boundary layer is thinner for high-Prandtl fluids.

3 A finite element method for the Navier-Stokes-Boussinesq equations using a Newton algorithm

This chapter sets the numerical algorithm for solving the system of equations described previously in Chapter 2 for both two and three-dimensional configurations. The finite element method and the Newton algorithm are presented first in detail. Then, the domain decomposition method for the three-dimensional configuration is discussed.

3.1 Motivation for the choice of the numerical method

In many in-house or commercial codes used to simulate phase-change problems (ANSYS CFX, Fluent, etc.), finite difference (FD) or finite volume (FV) methods are used most of the time with a fixed-mesh approach. Accurate simulations are therefore carried out by refining considerably the mesh resolution in the whole domain, and thus increasing dramatically the computational time. In the example of Voller et al. (1996) who used insufficient grid resolution to compute the melting of Gallium, Wang et al. (2010b) had to consider thinner meshes, resulting in a strong increase, of a factor of three, of the total mesh nodes to capture correctly the boundary layer structure.

Our choice for the finite element (FE) method is motivated by its capability to adapt dynamically the mesh and to deal with several geometrical domains. The adaptive capabilities of the FE discretization to use finer meshes where sharp phenomena take place (solid-liquid interfaces, boundary layers, recirculation zones) and coarser meshes elsewhere (in the solid, in the bulk of the fluid region where the gradient are lower than in the boundary layer region) is helpful to reduce the degrees of freedom involved in the numerical resolution and thus reduce the computational time. We use a finite-element method that was implemented using the open-source software FreeFem++ (Hecht et al., 2007; Hecht, 2012).

In this study, the use of mesh adaptivity proved mandatory to obtain accurate results within reasonable computational time. The numerical code was optimized to afford the mesh refinement every time step: the mesh density was increased around the phase change interfaces, offering an optimal resolution of the large gradients of all regularized functions (S, K, L_f), while the mesh was de-refined (larger triangles) in the solid part, where a coarser mesh could be used. A simulation using a globally refined mesh would require a prohibitive computational time for an equivalent accuracy of the melting front resolution. Similar algorithms based on FreeFem++ were successfully used for solving different systems of equations with locally sharp variation of the solution, such as Gross-Pitaevskii equation (Danaila and Hecht, 2010; Vergez et al., 2016) or Laplace equations with nonlinear source terms (Zhang and Danaila, 2013).

The space discretization is based on Taylor-Hood finite elements, approximating the velocity with $\mathbb{P}_2$ Lagrange finite elements (piecewise quadratic), and the the pressure with the $\mathbb{P}_1$ finite elements (piecewise linear). The temperature and the enthalpy are discretized using $\mathbb{P}_2$ finite elements. This discretization is second order accurate in space. We also use a second order accurate discretization in time. A fully implicit backward second order scheme (BDF2 or GEAR) is employed in the present study. The time derivative of a variable ϕ is approximated by:

$$\frac{d\phi}{dt} \simeq \frac{3\phi^{n+1} - 4\phi^{n} + \phi^{n-1}}{2\delta t}, \tag{3.1}$$

computing the solution ϕ^{n+1} at time $t_{n+1} = (n+1)\delta t$ by using two previous states (ϕ^n, ϕ^{n-1}). We use this scheme to advance in time both velocity ($\phi = \boldsymbol{u}$) and temperature fields ($\phi = \theta$). The other terms in Eqs. (2.12) - (2.14) are treated implicitly (*i. e.* taken at time t_{n+1}). The resulting non-linear equations are solved using a Newton algorithm.

Some authors used a Richardson extrapolation (Belhamadia et al., 2012; Wang et al., 2010b) in the momentum equation by extrapolating U from previous time steps. We have tested this approach, but the results exhibited less accurate solutions and the computations requested small δt. In addition, a projection algorithm with an explicit discretization of the Navier-Stokes-Boussinesq equations was also investigated, using the Adams-Bashforth and Crank-Nicolson second order schemes. The main drawback is the very small δt ($\sim 10^{-6}$) needed to ensure convergence at each time steps. A last alternative we tested for the treatment of non-linear terms in the momentum equation is the characteristics Galerkin method (Pironneau et al., 1992), but this method is not convenient for high $\mathcal{R}a$ simulations and requires very small time steps.

Finally, a supplementary difficulty comes from the one-domain method which needs techniques to bring the velocity to zero in the solid region. The switch-off technique, the variable viscosity approach and the Carman-Kozeny penalty term are the most used in the literature. We note that the physical meaning of the variable viscosity formulation and the Carman-Kozeny penalty term is fundamentally different. The Carman-Kozeny approach considers the mushy zone as a porous media, *i. e.* the solid is stationary and the liquid flows through the porous structure, while the variable viscosity formulation treats the mushy zone as a mixture of solid crystals and liquid, permitting thus a movement of both the solid and the liquid. The viscosity-based method was investigated by Danaila et al. (2014) and the Carman-Kozeny penalty method is investigated in the present work. We note however that techniques in FV methods based on the modification of the numerical algorithm to switch-off the velocity in the solid by a relaxation scheme also exist.

3.2 Finite element algorithm

To solve the system of Eqs. (2.12) - (2.14) we use a finite-element method. Finite-element methods for solving Navier-Stokes type systems of equations are generally based on a separate discretization of the temporal derivative (using finite difference, splitting or characteristics methods) and the generalization of the Stokes problem for the resulting system (Temam, 1983; Girault and Raviart, 1986; Quarteroni and Valli, 1994). We use the second-order implicit finite-difference discretization (3.1) of the temporal derivative and obtain the time semi-discretization of the single-domain model (2.12) - (2.14):

$$\nabla \cdot \boldsymbol{u}^{n+1} + \gamma p^{n+1} = 0, \tag{3.2}$$

$$\frac{3}{2}\frac{\boldsymbol{u}^{n+1}}{\delta t} + (\boldsymbol{u}^{n+1}\cdot\nabla)\boldsymbol{u}^{n+1} + \nabla p^{n+1} - \frac{1}{\mathcal{R}e}\nabla^2\boldsymbol{u}^{n+1} - A(\theta^{n+1})\boldsymbol{u}^{n+1} - f_B(\theta^{n+1})\,\boldsymbol{e}_y = 2\frac{\boldsymbol{u}^n}{\delta t} - \frac{\boldsymbol{u}^{n-1}}{2\delta t}, \tag{3.3}$$

$$\frac{3}{2}\frac{\theta^{n+1}+S(\theta^{n+1})}{\delta t} + \nabla\cdot\left(\boldsymbol{u}^{n+1}\theta^{n+1}\right) - \nabla\cdot\left(\frac{K}{\mathcal{R}e\mathcal{P}r}\nabla\theta^{n+1}\right) = 2\frac{\theta^n+S(\theta^n)}{\delta t} - \frac{\theta^{n-1}+S(\theta^{n-1})}{2\delta t}. \tag{3.4}$$

The penalty parameter γ is introduced to fill the diagonal of the pressure term at the algebraic level, when a Dirichlet boundary condition is applied for the velocity. The average value of the pressure field and the divergence-free velocity field, computed for different values of the penalty parameter γ, for the case of the natural convection of air, are given in Tab. 3.1.

γ	0.1	10^{-3}	10^{-7}	10^{-10}
$\int_\Omega \boldsymbol{\nabla}\cdot\boldsymbol{u}$	$1.27\cdot10^{-17}$	$6.70\cdot10^{-18}$	$5.61\cdot10^{-18}$	$3.54\cdot10^{-18}$
$\int_\Omega p$	$1.15\cdot10^{-16}$	$5.40\cdot10^{-14}$	$4.61\cdot10^{-10}$	$4.37\cdot10^{-7}$

Table 3.1: Average values of the pressure field and of the divergence of the velocity field, computed for different values of the penalty parameter γ.

One can observe a decreasing values of $\int_\Omega \boldsymbol{\nabla}\cdot\boldsymbol{u}$ for very low values of γ. However, larger values of $\int_\Omega p$ are observed for decreasing values of the penalty parameter. To ensure a good approximation of the pressure field with zero average, a value of $\gamma = 10^{-7}$ is set for all simulations. This system of non-linear equations is solved at time $t_{n+1} = (n+1)\delta t$, using two previous states at t_n and t_{n-1}.

The space discretization of variables over the domain Ω uses a finite-element method based on a weak formulation of the system of Eqs. (3.2) - (3.4). We consider homogeneous Dirichlet boundary conditions for the velocity, *i. e.* $\boldsymbol{u} = 0$ on $\partial\Omega$, and set the classical Hilbert spaces for the velocity and pressure:

$$\boldsymbol{V} = V\times V,\ V = H_0^1(\Omega), \quad Q = \left\{ q\in L^2(\Omega) \,\middle|\, \int_\Omega q = 0 \right\}. \tag{3.5}$$

Following the generalization of the Stokes problem (Temam, 1983; Girault and Raviart, 1986; Quarteroni and Valli, 1994), the variational formulation of the system of Eqs. (3.2) - (3.4) can be written as: find $(\boldsymbol{u}^{n+1}, p^{n+1}, \theta^{n+1}) \in \boldsymbol{V}\times Q\times V$, such that

$$b\left(\boldsymbol{u}^{n+1}, q\right) - \gamma(p^{n+1}, q) = 0, \quad \forall\, q\in Q \tag{3.6}$$

$$\frac{3}{2\delta t}\left(\boldsymbol{u}^{n+1},\boldsymbol{v}\right) + c\left(\boldsymbol{u}^{n+1};\boldsymbol{u}^{n+1},\boldsymbol{v}\right) + \frac{1}{Re}a\left(\boldsymbol{u}^{n+1},\boldsymbol{v}\right) - (A(\theta^{n+1})\,\boldsymbol{u}^{n+1},\boldsymbol{v}) + b\left(\boldsymbol{v},p^{n+1}\right) - \left(f_B(\theta^{n+1})\,\boldsymbol{e}_y,\boldsymbol{v}\right) = \frac{2}{\delta t}\left(\boldsymbol{u}^n,\boldsymbol{v}\right) - \frac{1}{2\delta t}\left(\boldsymbol{u}^{n-1},\boldsymbol{v}\right), \quad \forall\,\boldsymbol{v}\in\boldsymbol{V} \tag{3.7}$$

$$\frac{3}{2\delta t}\left(\theta^{n+1}+S(\theta^{n+1}),\phi\right) + \left(\boldsymbol{u}^{n+1}\cdot\nabla\theta^{n+1},\phi\right) + \left(\frac{K(\theta^{n+1})}{RePr}\nabla\theta^{n+1},\nabla\phi\right) = \frac{2}{\delta t}\left(\theta^n+S(\theta^n),\phi\right) - \frac{1}{2\delta t}\left(\theta^{n-1}+S(\theta^{n-1}),\phi\right), \quad \forall\,\phi\in V, \tag{3.8}$$

where $(u, v) = \int_\Omega u \cdot v$ denotes the scalar product in $L^2(\Omega)$ or $\left(L^2(\Omega)\right)^2$; the bilinear forms a, b and trilinear form c are defined as (Girault and Raviart, 1986; Quarteroni and Valli, 1994):

$$
\begin{aligned}
a : \boldsymbol{V} \times \boldsymbol{V} \to \mathbb{R}, \qquad & a(\boldsymbol{u}, \boldsymbol{v}) = \int_\Omega \boldsymbol{\nabla}^t \boldsymbol{u} : \boldsymbol{\nabla} \boldsymbol{v} = \sum_{i,j=1}^{2} \int_\Omega \partial_j u_j \cdot \partial_j v_i, \\
b : \boldsymbol{V} \times Q \to \mathbb{R}, \qquad & b(\boldsymbol{u}, q) = -\int_\Omega \nabla \cdot \boldsymbol{u}\, q = -\sum_{i=1}^{2} \int_\Omega \partial_i u_i \cdot q, \\
c : \boldsymbol{V} \times \boldsymbol{V} \times \boldsymbol{V} \to \mathbb{R}, \qquad & c(\boldsymbol{w}; \boldsymbol{z}, \boldsymbol{v}) = \int_\Omega \left[(\boldsymbol{w} \cdot \nabla)\, \boldsymbol{z}\right] \cdot \boldsymbol{v} = \sum_{i,j=1}^{2} \int_\Omega w_j (\partial_j z_i) v_i.
\end{aligned}
$$

The system of non-linear Eqs. (3.6) - (3.8), regarded as a general equation $\mathcal{F}(w) = 0$, with $w = (\boldsymbol{u}^{n+1}, p^{n+1}, \theta^{n+1})$, is solved using a Newton method. To advance the solution from time t_n to t_{n+1}, we start from an initial guess $w_0 = (\boldsymbol{u}^n, p^n, \theta^n)$ (which is the solution at t_n), and construct the Newton sequence $w_k = (u_k, p_k, \theta_k)$ by solving for each inner iteration k:

$$
D_w \mathcal{F}(w_k) w_{k+1} = D_w \mathcal{F}(w_k) w_k - \mathcal{F}(w_k). \tag{3.9}
$$

$D_w \mathcal{F}$ is the linear operator representing the differential of $\mathcal{F}$. Equation (3.9) can be rewritten as follows:

$$
\begin{aligned}
b\left(\boldsymbol{u}_{k+1}, q\right) - \gamma(p_{k+1}, q) &= 0, && (3.10) \\
\frac{3}{2\delta t}\left(\boldsymbol{u}_{k+1}, \boldsymbol{v}\right) + c\left(\boldsymbol{u}_{k+1}; \boldsymbol{u}_k, \boldsymbol{v}\right) &+ c\left(\boldsymbol{u}_k; \boldsymbol{u}_{k+1}, \boldsymbol{v}\right) && (3.11) \\
+\frac{1}{\mathcal{R}e} a\left(\boldsymbol{u}_{k+1}, \boldsymbol{v}\right) - \left(\frac{dA}{d\theta}(\theta_k)\, \theta_{k+1}\, \boldsymbol{u}_k, \boldsymbol{v}\right) &- \left(A(\theta_k)\, \boldsymbol{u}_{k+1}, \boldsymbol{v}\right) + b\left(\boldsymbol{v}, p_{k+1}\right) & \\
-\left(\frac{df_B}{d\theta}(\theta_k)\, \theta_{k+1}\, \boldsymbol{e}_y, \boldsymbol{v}\right) &= \frac{1}{\delta t}\left(2\boldsymbol{u}^n - \frac{1}{2}\boldsymbol{u}^{n-1}, \boldsymbol{v}\right) & \\
+c\left(\boldsymbol{u}_k; \boldsymbol{u}_k, \boldsymbol{v}\right) - \left(\frac{dA}{d\theta}(\theta_k)\, \theta_k\, \boldsymbol{u}_k, \boldsymbol{v}\right) &- \left(\left(\frac{df_B}{d\theta}(\theta_k)\, \theta_k - f_B(\theta_k)\right) \boldsymbol{e}_y, \boldsymbol{v}\right), & \\
\frac{3}{2\delta t}\left(\theta_{k+1} + \frac{dS}{d\theta}(\theta_k)\, \theta_{k+1}, \phi\right) + \left(\boldsymbol{u}_k \cdot \nabla \theta_{k+1}, \phi\right) &+ \left(\boldsymbol{u}_{k+1} \cdot \nabla \theta_k, \phi\right) && (3.12) \\
+\left(\frac{K(\theta_k)}{\mathcal{R}e\mathcal{P}r} \nabla \theta_{k+1}, \nabla \phi\right) + \left(\frac{dK}{d\theta}(\theta_k) \frac{\theta_{k+1}}{RePr} \nabla \theta_k, \nabla \phi\right) &= \frac{2}{\delta t}\left(\theta^n + S(\theta^n), \phi\right) + \left(\boldsymbol{u}_k \cdot \nabla \theta_k, \phi\right) & \\
+\frac{3}{2\delta t}\left(\frac{dS}{d\theta}(\theta_k)\, \theta_k - S(\theta_k),\, \phi\right) - \frac{1}{2\delta t}\left(\theta^{n-1} + S(\theta^{n-1}),\, \phi\right) &+ \left(\frac{dK}{d\theta}(\theta_k) \frac{\theta_k}{RePr} \nabla \theta_k, \nabla \phi\right). &
\end{aligned}
$$

Note that the last term of Eq. (3.11) cancels in the case of a linear Boussinesq force f_B (see Eq. (2.15)); this is not the case when non-linear variations of the density of the liquid are considered (convection or solidification of water). Note also that the previous system of Eqs. (3.10) - (3.12) depends only on $\boldsymbol{u}^n$, $\boldsymbol{u}^{n-1}$, θ^n and θ^{n-1} and is independent of p^n, the pressure being in this approach a Lagrange multiplier for the divergence free constraint. We underline the fact that the Newton loop (following k) has to be

iterated until convergence for each time step δt following the algorithm

$$
\begin{array}{l}
\text{Navier-Stokes time loop following } n \\
\text{set } w_0 = (\boldsymbol{u}^n, p^n, \theta^n) \\
\quad \text{Newton iterations following } k \\
\quad\quad \text{solve Eqs. (3.10) - (3.12) to get } \boldsymbol{w}_{k+1} \\
\quad \text{stop when } \|\boldsymbol{w}_{k+1} - \boldsymbol{w}_k\| < \xi_N \\
\text{actualize } (\boldsymbol{u}^{n+1}, p^{n+1}, \theta^{n+1}) = w_{k+1}.
\end{array}
\tag{3.13}
$$

In some cases, it is more relevant to solve directly the steady equation corresponding to Eqs. (3.6) - (3.8) (*i. e.* without the temporal derivatives), when a steady state could be achieved. It is, for example, the case for the natural convection of air or water in differentially heated configurations and low $\mathcal{R}a$ numbers. In the stationary case, the weak formulation of the problem becomes:

$$
\begin{aligned}
b\left(\boldsymbol{u}^{n+1}, q\right) - \gamma(p^{n+1}, q) &= 0, && (3.14)\\
\left(\boldsymbol{u}^{n+1}, \boldsymbol{v}\right) + c\left(\boldsymbol{u}^{n+1}; \boldsymbol{u}^{n+1}, \boldsymbol{v}\right) + a\left(\boldsymbol{u}^{n+1}, \boldsymbol{v}\right) & && (3.15)\\
-(A(\theta^{n+1})\,\boldsymbol{u}^{n+1}, \boldsymbol{v}) + b\left(\boldsymbol{v}, p^{n+1}\right) - \underline{\alpha\left(f_B(\theta^{n+1})\,\boldsymbol{e}_y, \boldsymbol{v}\right)} &= 0, && \\
\left(\boldsymbol{u}^{n+1} \cdot \nabla\theta^{n+1}, \phi\right) + \left(\frac{K}{\mathcal{R}e\mathcal{P}r}\nabla\theta^{n+1}, \nabla\phi\right) &= 0. && (3.16)
\end{aligned}
$$

The parameter α is introduced in front of the buoyancy force term f_B as a continuation parameter of the value of the $\mathcal{R}a$ number. The idea is to solve successively steady problems by increasing α from 0 to 1. At each stage, the previously computed solution is used as initial condition. These steps could be assimilated to a smooth increase of the $\mathcal{R}a$ number:

$$
\begin{array}{l}
\text{Loops for } m = 1 : \mathcal{N} \text{ steps} \\
\text{set } w_0 = (\boldsymbol{u}^n, p^n, \theta^n) \\
\quad \text{Newton iterations following } k \\
\quad\quad \text{solve (3.14) - (3.16) with } \alpha = \left(\frac{m}{\mathcal{N}}\right)^4 \\
\quad \text{stop when } \|\boldsymbol{w}_{k+1} - \boldsymbol{w}_k\| < \xi_N \\
\text{actualize } (\boldsymbol{u}^{n+1}, p^{n+1}, \theta^{n+1}) = w_{k+1},
\end{array}
\tag{3.17}
$$

with $\mathcal{N}$ the number of steps of the continuation algorithm.

This approach allows to compute the steady natural convection of air in 6 iterations for $\mathcal{R}a = 10^6$ instead of 150 iterations when the unsteady system of equations is solved until a steady state is reached.

3.3 Mesh adaptivity

We use the standard mesh adaptivity function (`adaptmesh`) offered by FreeFem++ (Hecht, 2012). The key idea implemented in this function (see also Borouchaki et al. (1996); Castro-Diaz et al. (2000); Hecht and Mohammadi (1997); George and Borouchaki (1998); Frey and George (1999); Mohammadi and Pironneau (2000)) is to modify the scalar product used in the automatic mesh generator to evaluate distance and volume. Equilateral elements are thus constructed, accordingly to the new metric. The

scalar product is based on the evaluation of the Hessian $\mathcal{H}$ of the variables of the problem. For example, for a $\mathbb{P}_1$ discretization of a variable χ, the interpolation error is bounded by:

$$\mathcal{E} = |\chi - \Pi_h \chi|_0 \leq c \sup_{T \in \mathcal{T}_h} \sup_{x,y,z \in T} |\mathcal{H}(x)|(y-z, y-z), \tag{3.18}$$

where $\Pi_h \chi$ is the $\mathbb{P}_1$ interpolate of χ, $|\mathcal{H}(x)|$ is the Hessian of χ at point x after being made positive definite. Using the Delaunay algorithm (*e. g.* George and Borouchaki (1998)) to generate a triangular mesh with edges close to the unit length in the metric $\mathcal{M} = \frac{|\mathcal{H}|}{(c\mathcal{E})}$ will result in a equally distributed interpolation error $\mathcal{E}$ over the edges a_i of the mesh. More precisely, we get

$$\frac{1}{c\mathcal{E}} a_i^T \mathcal{M} a_i \leq 1. \tag{3.19}$$

The previous approach could be generalized for a vector variable $\chi = [\chi_1, \chi_2]$. After computing the metrics $\mathcal{M}_1$ and $\mathcal{M}_2$ for each variable, we define a metric intersection $\mathcal{M} = \mathcal{M}_1 \cap \mathcal{M}_2$, such that the unit ball of $\mathcal{M}$ is included in the intersection of the two unit balls of metrics $\mathcal{M}_2$ and $\mathcal{M}_1$. For details, see the procedure defined in Frey and George (1999).

The `adaptmesh` function offers the possibility to take into account several metrics computed from different variables monitoring the evolution of the phase-change systems. For natural convection systems, the mesh will be adapted using the values of the two velocity components and the temperature. For phase-change systems, to accurately track the solid-liquid interface we add the variation of the enthalpy source term in the adaptivity criterion. For water systems (convection or freezing), we also add an extra function tracking the anomalous change of density around 4^oC. To reduce the impact of the interpolation on the global accuracy for time-depending problems, we consider, for each variable used for adaptivity, the metrics computed at actual (t_{n+1}) and previous (t_n) time instants (see also Belhamadia et al. (2004a)). The anisotropy of the mesh is a parameter of the algorithm and it was set to values close to 1. This is an inevitable limitation since we also impose the minimum edge-length of triangles to avoid too large meshes. The capabilities of the mesh adaptivity algorithm are illustrated in Chapter 5.

3.4 A finite-element toolbox for the simulation of phase-change systems with natural convection

The methods described previously were implemented in a 2D toolbox based on FreeFem++ . The syntax to implement the Newton algorithm is very close to the mathematical formulation given above. After defining a vectorial finite-element space `fespace Wh(Th,[P2,P2,P1,P1]);`, associated to the mesh `Th`, we define the velocity, pressure and temperature variables in a compact manner by `Wh [u1,u2,p,T];`. Corresponding test functions are defined similarly. It is then very easy to define a `problem` formulation in FreeFem++ and include all the terms of the algorithm (3.10) - (3.12). This makes the reading of the programs very intuitive by comparing each term to its mathematical expression. New terms could be added to the variational formulation expressed in the `problem` structure, without affecting other parts of the program. Consequently, the implementation of new models or numerical methods for this problem is greatly facilitated by this modular structure of programs.

In this section we first describe the architecture of the programs and the organisation of files. Then we focus on the list of input parameters and the structure of output files.

3.4.1 Program architecture

Figure 3.1 gives a schematic overview of the content of the toolbox. All files are provided in a directory called `PCM-Toolbox`. Many detailed comments are included in the programs, with direct link to the mathematical expressions used in this chapter. The FreeFem++ syntax was intentionally kept at a low level of technicality and supplemented with detailed comments when specific more technical syntax was used.

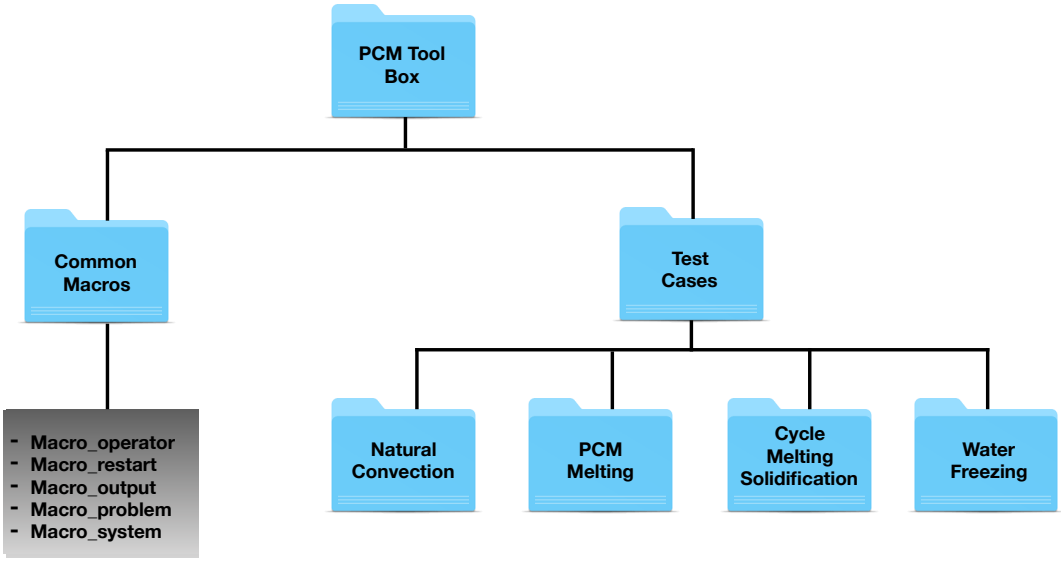

Figure 3.1: Folder tree structure of the FreeFem++ toolbox to solve phase change problems. Test cases and common macros are separated into two folders.

This directory is organized as follows:

1. The directory `Common-Macros` contains five files:
   - *Macro_operator.idp* includes macros and functions defining mathematical operators,
   - *Macro_problem.idp*: macros defining the variational formulation of the problem,
   - *Macro_restart.idp*: macros used to start a new simulation from a saved field,
   - *Macro_output.idp*: macros used to save the solution with different formats,
   - *Macro_system.idp*: macros identifying the OS and defining specific OS-commands.

2. The directory `Test-Cases` contains four subdirectories, each of them defining one of the following applications:
   - natural convection of air or water in a differentially heated square cavity,
   - melting of a PCM stored in containers of different shapes,
   - melting followed by solidification of a rectangular PCM,
   - freezing of pure water in a square cavity.

   Each subdirectory contains three files: *NEWTON_$case.edp* is the main FreeFem++ script file, $param\_phys.inc$ defines the physical parameters and $param\_num.inc$ the numerical parameters. For example, to run the natural convection case of air in a square cavity, one can use the following command in a terminal window:

```
FreeFem++ NEWTON_stat_natconv.edp
```

The folder structure of each test case is illustrated in Fig. 3.2. The obtained solutions are saved in the folder `OUTPUT/Data`. Depending on the output format selected by the user, data files are generated in specific folders for being visualized with: Tecplot, Paraview, Gnuplot or Medit. We also provide in the folder `Figures` ready-made layouts for these visualisation softwares. The user can thus obtain the figures from the current work using newly generated data. More details about the output structure are given below.

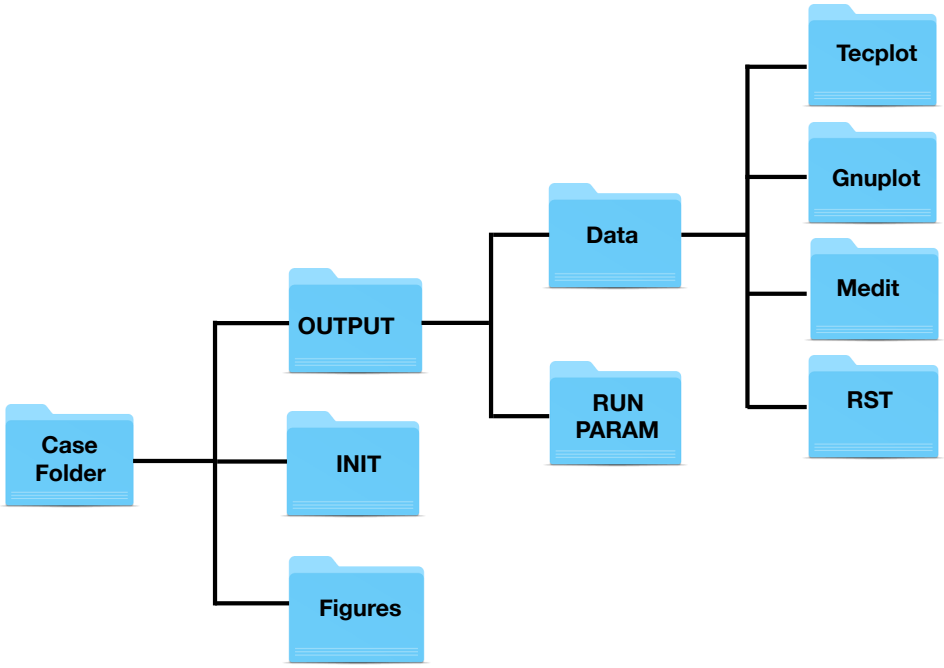

Figure 3.2: Structure of each Test-case folder.

3.4.2 Input parameters

Physical parameters and parameters related to the run are separated into two files.
(1) The file *param_phys.inc* contains the physical descriptions of the problem:

- **typeT**: is the finite-element type for the temperature, with possible values `P2` or `P1`,
- **Torder**: is the accuracy order of the time integration scheme, with possible values 1 (Euler scheme) or 2 (Gear scheme),
- **scalAdim**: defines the characteristic scales of the problem, see Eq. (2.11). Possible values 1, 2 or 3 correspond to the following choice of the characteristic scales (Danaila et al., 2014):

$$(1) \quad : \quad V_{ref}^{(1)} = \frac{\nu_l}{H} \Longrightarrow t_{ref}^{(1)} = \frac{H^2}{\nu_l} \Longrightarrow \mathcal{R}e = 1, \tag{3.20}$$

$$(2) \quad : \quad V_{ref}^{(2)} = \frac{\alpha}{H} \Longrightarrow t_{ref}^{(2)} = t_{ref}^{(1)} \mathcal{P}r \Longrightarrow \mathcal{R}e = 1/\mathcal{P}r, \tag{3.21}$$

$$(3) \quad : \quad V_{ref}^{(3)} = \frac{\nu_l}{H}\sqrt{\frac{\mathcal{R}a}{\mathcal{P}r}} \Longrightarrow t_{ref}^{(3)} = t_{ref}^{(1)}\sqrt{\frac{\mathcal{P}r}{\mathcal{R}a}} \Longrightarrow \mathcal{R}e = \sqrt{\frac{\mathcal{R}a}{\mathcal{P}r}}, \tag{3.22}$$

- **$\mathbf{x}_l$, $\mathbf{x}_r$, $\mathbf{y}_l$, $\mathbf{y}_r$**: are the values defining the dimensions of the cavity $[x_l, x_r] \times [y_l, y_r]$,
- **Pr, Ra, Ste**: are the Prandtl, Rayleigh and Stefan numbers, see Eq. (2.16) and (2.15),
- **$\mathbf{T}_{hot}$, $\mathbf{T}_{cold}$**: are dimensionless temperatures according to Eq. (2.11),
- **$\mathbf{bcu}_1$, $\mathbf{bcu}_2$, bcT**: are macros defining the velocity ($\boldsymbol{u}$) and the temperature (T) boundary conditions.
- **epsi**: is the half width ε of the mushy region. Default value = 0.01,
- **dt**: is the dimensionless time step,
- **$\mathbf{t}_{max}$**: is the dimensionless final time,
- **Parameters for regularization functions**:
  The parameters of the hyperbolic-tangent function in Eq. (2.19), used to regularize discontinuous functions are set by default as follows:

	f_s	f_l	a_s	θ_s	R_s	C_{CK}	b
*E*nthalpy	0	1/Ste	1	0.01	0.01	-	-
*C*arman - Kozeny	0	1	1	0.01	0.01	10^6	10^{-7}
*C*onductivity (water)	1	2.26/0.578	1	θ_f	0.015	-	-

- **rho(T) and Drho(T)**: (water cases only) define the density and its derivative as functions of the temperature, following the model (Gebhart and Mollendorf, 1977):

$$\rho(T) = \rho_m(1 - \omega|T - T_m|^q),$$

ρ_m [kg/m^3]	ω [^{o}C^{-q}]	q	T_m [^{o}C]
999.972	$9.2793 \cdot 10^{-6}$	1.894816	4.0293

- **$\mathbf{f}_B$(T), $\mathbf{df}_B$(T)**: define the buoyancy force and its derivative.

(2) The file *param_num.inc* contains the parameters controlling the run.
Restart parameters:

- **Nsave**: the solution is saved every $Nsave$ time steps in the `Data` folder (see Fig. 3.2). The temperature and the velocity fields are saved in `Tecplot` and `Medit` folders, while the liquid fraction, the Nusselt number, and the accumulated heat input are saved in the `Gnuplot` folder.
- **Nrestart**: restart files (mesh and solution) are saved every $Nrestart$ time steps. Solutions at current and previous iterations, the CPU time, the accumulated heat input Q_0, and the time step dt are saved in the folder `RST`.
- **Ncondt**: allows the user to stop the run and save the solution properly.
  The file `OUTPUT/zz.condt` is read every $Ncondt$ time steps: if the user replaces the value "0" in this file by "1" the run is stopped. This is a simple solution for a clean stop of the job by the user. Default value = 20.
- **Nremesh**: the mesh is adapted every $Nremesh$ iterations. If this parameter is set to "1" the mesh is adapted every time step.

- **IFrestart**: is a boolean controlling the set up of the initial field.
  $IFrestart = 0$, the initial condition is built in the code for each test case. For the PCM melting cases, the PCM is initially motionless at isothermal temperature. To set-up a smooth initial field, a few time steps (with very small δt) are computed by increasing progressively the boundary temperature at the hot wall and the Rayleigh number (by continuation). Outputs are saved in `OUTPUT/Data-RST-0`.
  $IFrestart > 0$, (positive integer values) the solution field previously computed at iteration $IFrestart$ is loaded from the folder `OUTPUT/Data-RST-filenameRST/RST`,
  with `filenameRST` a variable selecting the restart folder.
  $IFrestart < 0$, (negative integer values), the same principle for loading a solution is used, but from the folder `INIT` (see Fig. 3.2). The solution fields stored in this folder could come from different previous calculations (*e. g.* a steady state solution or, for the water, the natural convection field before freezing).

Newton parameters:

- **epsconv**: is the value of the stopping criterion for steady cases,
- **gamma**: is the penalty parameter in Eq. (3.2). Default value = 10^{-7},
- **tolNewton**: is the Newton tolerance ξ_N (see Eq. (3.13)). Default value = 10^{-6},
- **newtonMax**: limits the maximum number of iterations in the Newton algorithm (3.13). Default value = 50,

Mesh parameters:

- **nbseg**: is the number of segments for the discretisation along the x and y directions,
- **errh**: is the interpolation error level. Default value = 0.02,
- **hmin, hmax**: are the minimum and maximum edge size, respectively,
- **adaptratio**: is the ratio for a prescribed smoothing of the metric. For a value less than 1.1 no smoothing is done. Default value = 1.5,
- **nbvx**: is the maximum number of vertices allowed in the mesh generator. Default value = 50000.

Output parameters:

- **dircase**: is the name of the output folder,
- **fcase**: is the prefix-name for ouput files.
- **Tecplot, Medit, Gnu**: correspond to the name of the visualisation software to be used; the format of the outputs written in `OUTPUT/Data` (see Fig. 3.2) is accordingly set. The files from the Tecplot folder can be easily read also with Paraview.

3.4.3 Outputs

When a computation starts, the `OUTPUT` directory is created (see Fig. 3.2). It contains two folders storing the output data and the echo of the run parameters. The folder `Data` contains four subdirectories with different output format files of the computed solution. File names are created using the prefix defined by the parameter **fcase**, the current iteration and the current dimensionless time t. Solution

files can be visualized using either Tecplot or any other CFD Visualization tools (Paraview, Visit, etc.). Moreover, *.gmsh* (mesh) and *.rst* (fields) files are generated in the folder `RST` to enable restarts of the computation. Note that the folder `FFglut` contains FreeFem++ scripts that re-read and visualize the RST-files to facilitate the selection of a restart field. An *.echo* file with a summary of the main parameters, informations on the run and the names of the output files is saved in the folder `RUNPARAM`. This directory additionally contains a copy of the *.inc* parameter files, allowing an easy identification of each case and preparing an eventual rerun of the same case.

3.5 Numerical tests of the accuracy of the numerical method

We start by presenting tests of the accuracy of our numerical method. We used the technique of manufactured solutions (*e. g.* Roache (1998)) which has the advantage of providing an exact solution to a modified problem, related to the initial one. The general idea is to modify the original system of equations by introducing an extra source term, such that the new system admits an exact solution given by a convenient analytic expression. Even though in most cases exact solutions constructed in this way are not physically realistic, this approach allows one to rigorously verify computations.
We tested the space and time accuracy using manufactured solutions for the system of Eqs. (2.12) - (2.14) for a stationary case (Burggraf flow) and a time-dependent one (Nourgaliev et al., 2016). For both cases, we computed the global error ε for different norms in space:

$$\varepsilon = \|\Phi_e - \phi_h\|, \tag{3.23}$$

with Φ_e the exact solution and ϕ_h the numerical solution. Computations were performed for the convection of air ($C = K = 1$, $A(\theta) = S(\theta) = 0$), with a Rayleigh number $\mathcal{R}a = 10^4$ and a Prandtl number $\mathcal{P}r = 0.71$.

3.5.1 Space accuracy: Burggraf stationary flow with thermal effects

The Burggraf manufactured solution is a time-independent recirculating flow inside a square cavity $[0,1] \times [0,1]$. It is similar to the well-known entrained cavity flow, with the difference that the velocity singularity at the top corners of the cavity is avoided. We added to the classical Burggraf flow (Shih et al., 1989; Laizet and Lamballais, 2009) a manufactured solution for the temperature, with constant temperature imposed at the top and the bottom walls. Vertical walls are assumed to be adiabatic. The exact solution of the new flow with thermal effects is

$$\begin{aligned}
u_1(x,y) &= \sigma g'(x)h'(y), \\
u_2(x,y) &= -\sigma g''(x)h(y), \\
p(x,y) &= \frac{\sigma}{\mathcal{R}e}\left(h^{(3)}(y)g(x) + g''(x)h'(y)\right) + \frac{\sigma^2}{2}g'(x)^2\left(h(y)h''(y) - h'(y)^2\right), \\
T(x,y) &= T_c + (T_h - T_c)y + a(x)b(y),
\end{aligned} \tag{3.24}$$

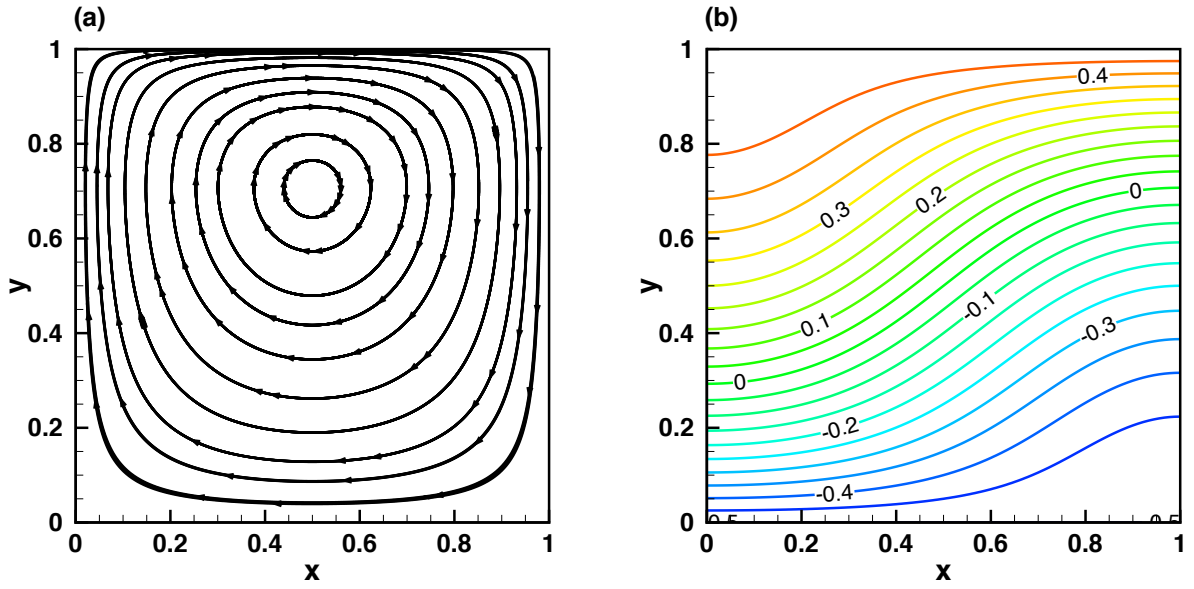

Figure 3.3: Burggraf stationary flow with thermal effects used to test the space accuracy of the numerical scheme. Streamlines (a) and temperature contours (b) of the flow field.

with $\sigma > 0$ a scaling parameter and functions

$$\begin{aligned} g(x) &= \frac{x^5}{5} - \frac{x^4}{2} + \frac{x^3}{3}, \\ h(y) &= y^4 - y^2, \\ a(x) &= \cos(\pi x), \\ b(y) &= y(1-y). \end{aligned} \tag{3.25}$$

Note that the velocity at the top border of the cavity is

$$u_1(0,1) = 2\sigma(x^4 - 2x^3 + x^2), \quad u_2(x,1) = 0, \tag{3.26}$$

which ensures the continuity of the velocity at corners ($\boldsymbol{u}(0,1) = \boldsymbol{u}(1,1) = 0$), since no-slip walls are imposed for the other borders: $\boldsymbol{u}(x,0) = \boldsymbol{u}(0,y) = \boldsymbol{u}(1,y) = 0$.

The forcing terms that have to be added to the momentum and energy (temperature) equation are derived by injecting the exact solution (3.24) into the system of Eqs. (2.12) - (2.14):

$$\begin{aligned} f_{u_1} &= 0, \\ f_{u_2} &= \sigma^2 h(y)h'(y)\left(g''(x)^2 - g'(x)g^{(3)}(x)\right) \\ &+ \frac{\sigma}{\mathcal{R}e}\left(g^{(4)}(x)h(y) + 2g''(x)h''(y) + g(x)h^{(4)}(y)\right) \\ &+ \frac{\sigma^2}{2}g'(x)^2\left(h(y)h^{(3)}(y) - h'(y)h''(y)\right) - \frac{\mathcal{R}a}{\mathcal{P}r\mathcal{R}e^2}T(x,y), \\ f_T &= u_1(x,y)a'(x)b(y) + u_2(x,y)\left(T_h - T_c + a(x)b'(y)\right) \\ &- \frac{K}{\mathcal{R}e\mathcal{P}r}\left(a''(x)b(y) + a(x)b''(y)\right). \end{aligned} \tag{3.27}$$

We used the Taylor-Hood finite element ($\mathbb{P}_2$ for the velocity and $\mathbb{P}_1$ for the pressure) and tested $\mathbb{P}_1$ or $\mathbb{P}_2$ finite elements for the temperature. Figures 3.3a and 3.3b illustrate the streamlines and the temperature field, respectively.

Figure 3.4 plots the discretization error ε as a function of the grid size $h = \delta x = \delta y$ for the temperature and the velocity. Both L^2 and L^∞ norms are displayed. The expected second order accuracy in L^2-norm is obtained with $\mathbb{P}_1$ finite elements (Figs. 3.4a and 3.4b), while an order exceeding three is observed when $\mathbb{P}_2$ finite elements are used (Fig. 3.4c and 3.4d).

The optimal convergence for the velocity, the pressure and the temperature is shown in Fig. 3.5, for their natural norms: H^1 norms for the velocity and the temperature, and L^2 norm for the pressure. A seconder order convergence is observed for the velocity and the pressure, whatever $\mathbb{P}_1$ or $\mathbb{P}_2$ finite elements are considered for the temperature (Figs. 3.5a - 3.5c), consistent with the Taylor-Hood finite elements employed. Moreover, as expected, a first order accuracy is obtained for the temperature using $\mathbb{P}_1$ finite elements (Fig. 3.5b) and a second order using $\mathbb{P}_2$ finite elements (Fig. 3.5d).

3.5.2 Time accuracy: manufactured unsteady solution

To test the time accuracy of the Gear (BDF2) scheme, we used the manufactured time-dependent solution suggested in Nourgaliev et al. (2016):

$$
\begin{aligned}
u_1(x,y,t) &= (\delta U_0 + \alpha_u \sin(t)) \cos(x+\gamma_1 t) \sin(y+\gamma_2 t), \\
u_2(x,y,t) &= -(\delta U_0 + \alpha_u \sin(t)) \sin(x+\gamma_1 t) \cos(y+\gamma_2 t), \\
T(x,y,t) &= \bar{T} + (\delta T_0 + \alpha_t \sin(t)) \cos(x+\gamma_1 t) \sin(y+\gamma_2 t), \\
p(x,y,t) &= \bar{P} + (\delta P_0 + \alpha_p \sin(t)) \sin(x+\gamma_1 t) \cos(y+\gamma_2 t),
\end{aligned}
\tag{3.28}
$$

The values of the constants are reported in Table 3.2.

γ_1	γ_2	$\bar{P}$	$\bar{T}$	δP_0	δT_0	δU_0	α_p	α_u	α_t
0.1	0.1	0	1.0	0.1	1.0	1.0	0.05	0.4	0.1

Table 3.2: Parameter for the time-dependent manufactured solution (3.28).

The corresponding forcing source terms are

$$
\begin{aligned}
f_{u_1} &= \alpha_u \cos(t) \cos(a)\sin(b) - U_c\,\gamma_1 \sin(a)\sin(b) + U_c\,\gamma_2 \cos(a)\cos(b) \\
&\quad -U_c\,u_1(x,y,t) \sin(a)\sin(b) + U_c\,u_2(x,y,t) \cos(a)\cos(b) + P_c \cos(a)\cos(b) \\
&\quad + \frac{2}{\mathcal{R}e}\, u_1(x,y,t), \\
f_{u_2} &= -\alpha_u \cos(t) \sin(a)\cos(b) - U_c\,\gamma_1 \cos(a)\cos(b) + U_c\,\gamma_2 \sin(a)\sin(b) \\
&\quad -U_c\,u_1(x,y,t) \cos(a)\cos(b) + U_c\,u_2(x,y,t) \sin(a)\sin(b) - P_c \sin(a) \sin(b) \\
&\quad + \frac{2}{\mathcal{R}e}\, u_2(x,y,t) - \frac{\mathcal{R}a}{\mathcal{P}r\mathcal{R}e^2}\, T(x,y,t), \\
f_T &= \alpha_t \cos(t) \cos(a)\sin(b) - T_c\,\gamma_1 \sin(a)\sin(b) + T_c\,\gamma_2 \cos(a)\cos(b) \\
&\quad -T_c\,u_1(x,y,t) \sin(a)\sin(b) + T_c\,u_2(x,y,t) \cos(a)\cos(b) + \frac{2K}{\mathcal{R}e\mathcal{P}r}\, T_c \cos(a)\sin(b),
\end{aligned}
\tag{3.29}
$$

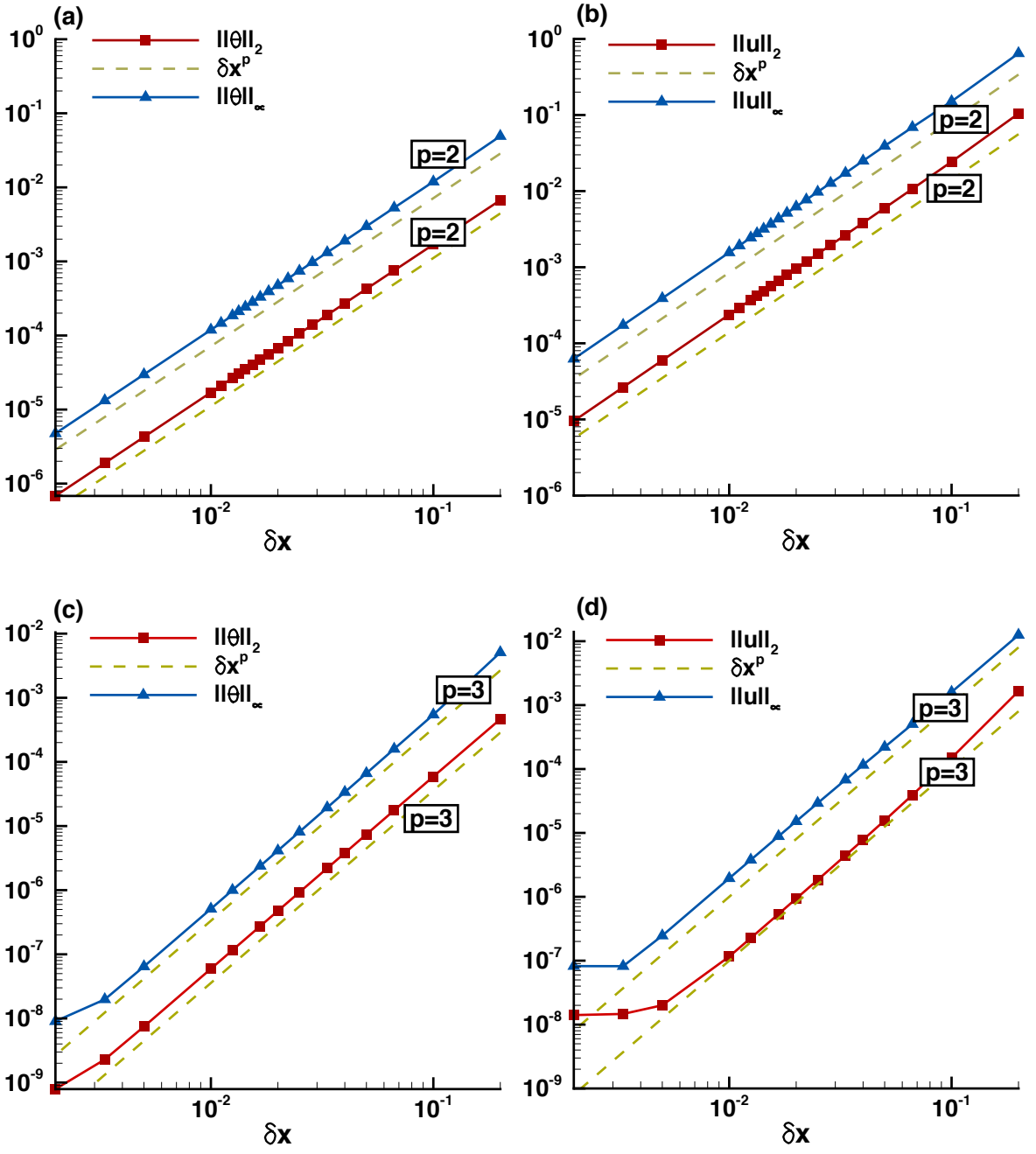

Figure 3.4: Burggraf stationary flow with thermal effects used to test the space accuracy of the numerical scheme. Global error ε (3.23) for the temperature θ and velocity $\boldsymbol{u}$. Numerical scheme using $\mathbb{P}_1$ finite elements for the temperature (panels a and b) or $\mathbb{P}_2$ for the temperature (panels c and d).

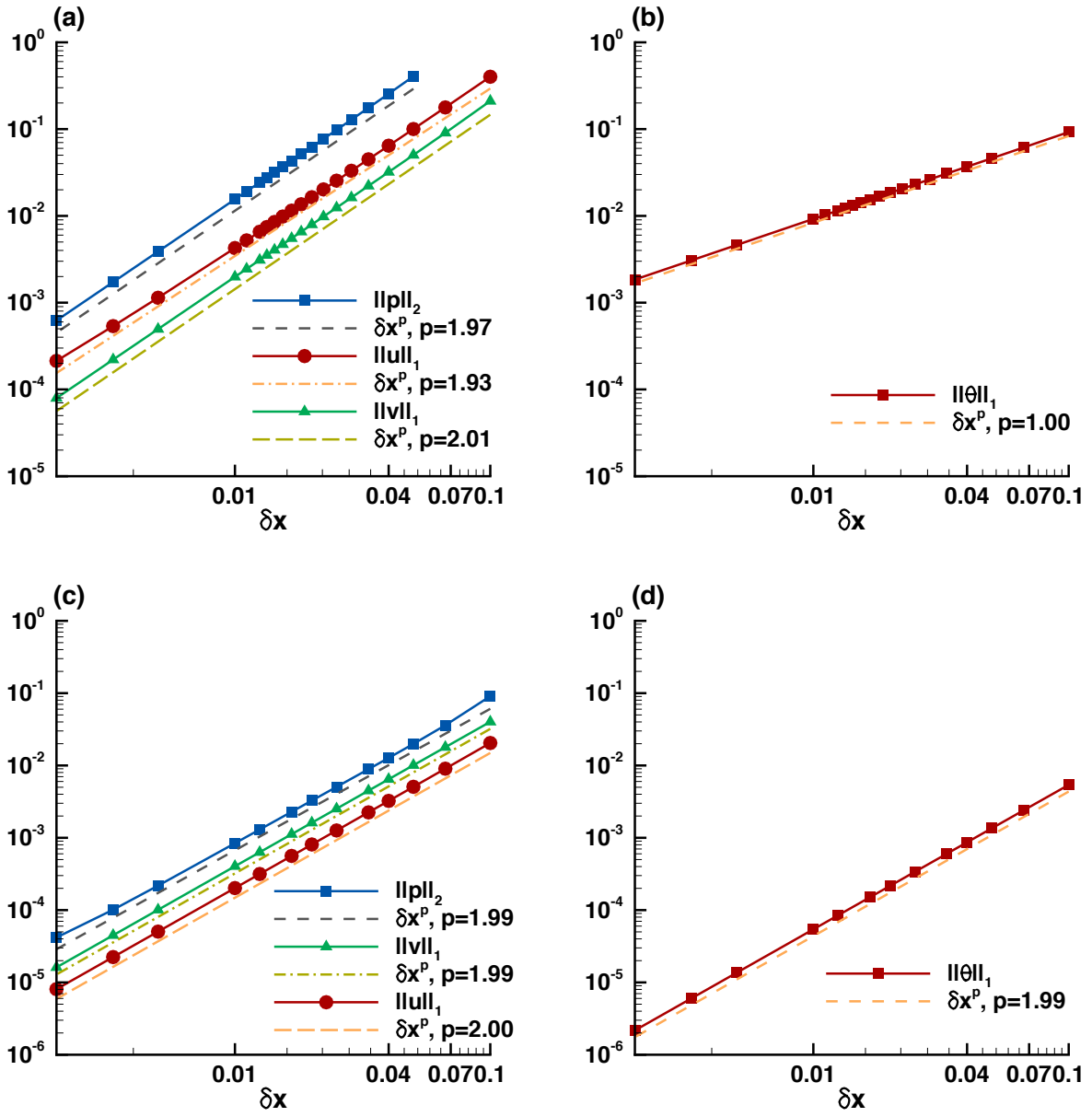

Figure 3.5: Burggraf stationary flow with thermal effects used to test the space accuracy of the numerical scheme. Global errors ε (3.23) for the pressure p, the velocity $\boldsymbol{u}$, and the temperature θ. Numerical scheme using $\mathbb{P}_1$ finite elements for the temperature (panels a and b) or $\mathbb{P}_2$ finite elements (panels c and d).

where $a = (x + \gamma_1 t)$, $b = (y + \gamma_2 t)$ and $U_c = (\delta U_0 + \alpha_u \sin(t))$, $T_c = (\delta T_0 + \alpha_u \sin(t))$, $P_c = (\delta P_0 + \alpha_u \sin(t))$.

Guided by the results obtained in Sec. 3.5.1 for the space accuracy, we fixed the grid size to $h = dx = 0.01$ and we applied $\mathbb{P}_2$ discretization for the temperature, to ensure small spatial discretization errors. For diminishing values of the time step δt, the solution was evolved in time up to the time instant $t_{max} = \pi$ at which the error (3.23) was computed. The time convergence is displayed in Fig. 3.6 for the temperature (panel a) and the velocity (panel b) variables, for which the expected second order convergence in time is obtained.

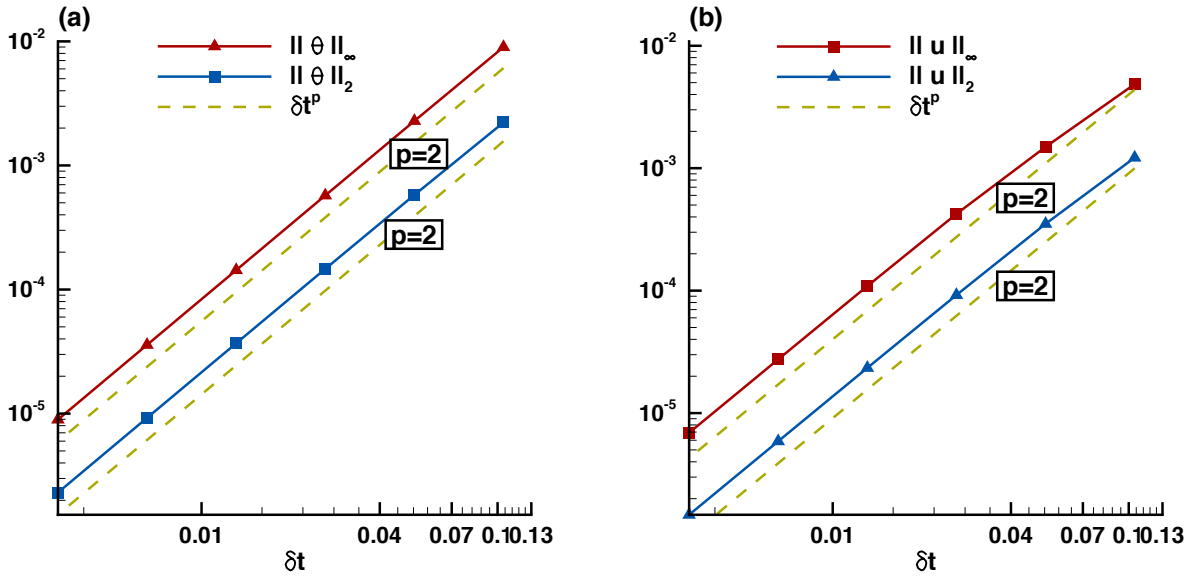

Figure 3.6: Time accuracy of the numerical scheme tested using the time-dependent manufactured solution of Nourgaliev et al. (2016). Discretization using $\mathbb{P}_2$ finite elements for the temperature. Evolution of the global error ε (3.23) for the temperature (a) and the velocity (b) measured at $t_{max} = \pi$.

3.6 Domain decomposition method with FreeFem++: FFDDM

Solving the Navier-Stokes-Boussinesq systems of Eqs. (3.6) - (3.8) in three-dimensional configurations could generate large-size problems. The natural convection of air in a cube of dimensions $[0, 1]^3$ with $40 \times 40 \times 40$ uniform grid involves 3 millions of unknowns (d.o.f.) in the linear system, when a $\mathbb{P}_1$ finite element is considered for the temperature. For such a large-size problem, memory limitation can rapidly arise with sequential algorithms. It is thus essential to distribute data among several processors.

A natural approach is the domain decomposition method (DDM). DDM aims at dividing the computational domain in many subdomains on which we solve local problems with adequate interface conditions. Two families of DDM exists: non-overlapping methods and overlapping methods such as the Schwarz method.

We use in this work a domain decomposition Schwarz method, enhanced by coarse space corrections

through the FreeFem++ library `ffddm`. This enrichment with a coarse space is mandatory in the present study to avoid the lack of robustness related to the one-level method. The main drawback of one-level methods is their convergence rate that depends on the number of subdomains, resulting in a poor scaling for large problems. This is mostly due to a lack of global communication between subdomains that exchange informations with their direct neighbors only. The additional coarse space has consequently the task to spread the information to all subdomains at each iteration.

The data distribution among processors is done via an overlapping domain decomposition and involves a related linear algebra. To enable parallel computing, the mesh is first split into subdomains using `Scotch` or `Metis` libraries. Figure 3.7 illustrates the domain decomposition of a cube of dimension $[0,1]^3$ into 8 subdomains with `Metis` graph partitioner. Mesh adaptivity using metrics control makes possible the optimisation of the distribution of mesh elements.

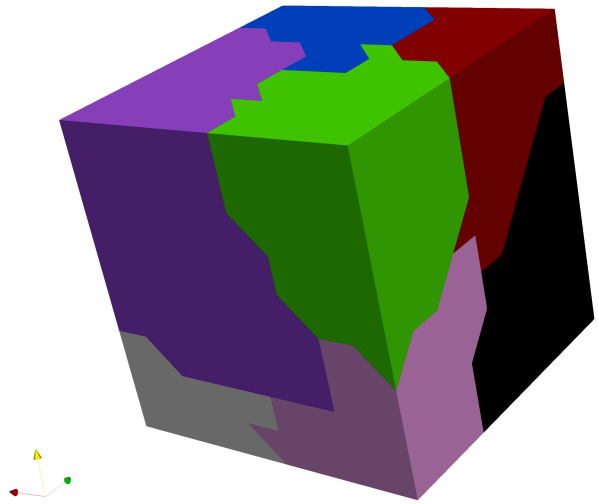

Figure 3.7: Partition of $\Omega = [0,1]^3$ into 8 subdomains with `Metis` partitioner.

The final linear system of Eqs. (3.10) - (3.12) is solved in parallel using a GMRES Krylov method, with an Optimized Restricted Additive Schwarz (ORAS) preconditioner. To solve the linear equation $Ax = b$, the ORAS preconditionner reads

$$M_{RAS}^{-1} = \sum_{j=1}^{\mathcal{N}} R_j^T D_j (R_j A R_j^T)^{-1} R_j, \tag{3.30}$$

R_j denote the restriction operators and D_j are square diagonal matrices. Local matrices are defined as:

$$A_j = R_j A R_j^T. \tag{3.31}$$

The duplicated unknowns due to the overlap between subdomains are coupled via a partition of unity

$$I = \sum_{i=1}^{\mathcal{N}} R_i^T D_i R_i. \tag{3.32}$$

Thus, the global solution U is defined as:

$$U = \sum_{i=1}^{\mathcal{N}} R_i^T D_i R_i U = \sum_{i=1}^{\mathcal{N}} R_i^T D_i U_i. \tag{3.33}$$

We assess on the strong scalability of the ORAS preconditioner in the 3D differentially heated cubic cavity. We vary the number of subdomains while the global system size is fixed. With a $\mathbb{P}_2$ finite element for the temperature, we solve 7.2 million of unknowns (d.o.f). The domain is decomposed into subdomains with `Metis`, ranging from 48 to 400 subdomains.

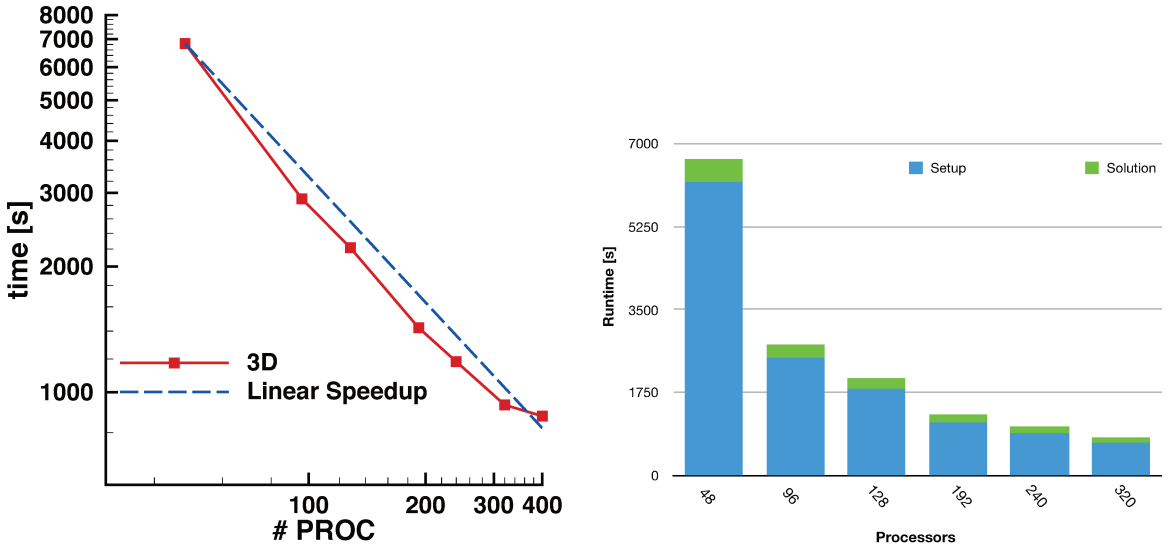

Figure 3.8: Strong scalability of the ORAS preconditioner: 7.2 millions of d.o.f and subdomains ranging from 48 to 400.

Figure 3.8 illustrates the evolution of the total wall clock time for calculations with a different number of subdomains. A good speed-up is observed. From 48 to 320 processors we observe a linear speed-up. The total runtime passes from 2 hours for 48 subdomains to 15 minutes for 320 subdomains. The linear speed-up is then slightly lost for 400 subdomains but remains reasonable. In Tab. 3.3 we detail the different runtimes relative to this test. The column "Factorization" denotes the time spent in the factorization of the local submatrices and "GMRES" gives the time taken by GMRES to solve the global linear system by the domain decomposition algorithm.

$\mathcal{N}$	Factorization (s)	GMRES (s)	Total Step (s)
48	6186.33	473.66	6659.99
96	2468.68	283.099	2751.779
128	1814.26	237.853	2052.113
192	1111.5	169.174	1280.674
240	889.422	146.539	1035.961
320	674.204	114.346	788.55
400	614.418	107.422	721.84

Table 3.3: Strong scaling experiment in a 3D differentially heated cavity. 7.2 millions of d.o.f and subdomains ranging from 48 to 400.

4 Numerical simulation of natural convection flow in a 2D square cavity

We first focus on the capability of our code to deal with natural convection flows in square enclosures. The convection flow is a relevant case to validate rigorously the Navier-Stokes-Boussinesq solver. A large number of benchmarks on natural convection problems induced by temperature difference could be found in the literature, with connection to engineering (air circulation in buildings, double-wall insulations, solar collectors, etc.) and geophysical systems.

In this chapter, we are interested on the natural convection of fluids in a square cavity differentially heated from the vertical walls. The fluid temperature rises and its density decreases along the heated wall, convecting the fluid up to the point where it reaches the cold wall, along which the reverse process occurs. These two simultaneous opposed effects create a recirculation cell within a stationary zone in the center.

We solve the system of Eqs. (2.12) - (2.14), with $A(\theta) = 0$ in the momentum equation and $S(\theta) = 0$ in the energy equation. Linear and non-linear expressions of the buoyancy force $f_B(T)$ are investigated, by simulating the natural convection of air and water, respectively. Natural convection of water exhibits a non-linear variation of the density with a maximum value around $T = 4^oC$. A linear variation with temperature is generally assumed for the natural convection of air in the Boussinesq approximation. We consider a square enclosure of height H. Physical properties of air and water used in our simulations are listed in Tab. 4.1. Isothermal boundary conditions are applied at the vertical

	ρ kg/m^3	μ kg/(m s)	c_p J/(kg K)	k W/(m K)	α m^2/s	β 1/K
Air	1.177	$1.85 \cdot 10^{-5}$	1006	0.0262	$2.22 \cdot 10^{-5}$	$3.4 \cdot 10^{-3}$
Water	999.84	$1.003 \cdot 10^{-3}$	4182	0.578	$1.33 \cdot 10^{-7}$	$6.91 \cdot 10^{-5}$

Table 4.1: Physical parameters of air and water at $T = 300K$ used in our simulations. $\mathcal{P}r = 0.71$ (for air) and $\mathcal{P}r = 6.99$ (for water).

walls and adiabatic boundary conditions to the upper and lower walls. Quantitative and qualitative validations are carried out as following. **(i)** The velocity profile along symmetry lines, the maximum value of $\boldsymbol{u}$ at mid-domain ($x = 0.5$ and $y = 0.5$), locations x_{max} and y_{max} of this maximum and the Nusselt number are compared with the spectral-accurate simulations by Le Queré (1991) and de Vahl Davis (1983) in Sec. 4.1.1 for natural convection of air within a square cavity. **(ii)** A heated obstacle is included in the center of the domain and the transversal velocity profile along the horizontal symmetry lines is compared with numerical results of Moglan (2013) in Sec. 4.1.2. **(iii)** The temperature profile along the horizontal symmetry line is compared with numerical results of Michalek and Kowalewski (2003) in Sec. 4.2 for the natural convection of water.

4.1 Natural convection of air

We start by testing the Newton algorithm (3.10) with linear expression of $f_B(\theta)$ (see Eq. (2.15)). The classical problem of the thermally driven square cavity with adiabatic top and bottom walls is simulated. We consider a cavity of height $H = 0.1$ m, initially filled with motionless air and a linear distribution of the temperature. The dimensionless parameters describing the investigated configuration are based on the fluid properties presented in Tab. 4.1. $\mathcal{P}r = 0.71$ and Rayleigh number ranges from $\mathcal{R}a = 10^4$ to 10^8. The characteristic scales of the problem are:

$$L_{ref} = H, \quad T_{ref} = \frac{T_h + T_c}{2}, \tag{4.1}$$

and,

$$V_{ref} = \frac{\nu_l}{H}\sqrt{\frac{\mathcal{R}a}{\mathcal{P}r}} \quad \Longrightarrow \quad t_{ref} = \frac{H^2}{\nu_l}\sqrt{\frac{\mathcal{P}r}{\mathcal{R}a}} \quad \Longrightarrow \quad \mathcal{R}e = \sqrt{\frac{\mathcal{R}a}{\mathcal{P}r}}. \tag{4.2}$$

The left wall is heated with dimensionless hot temperature $\theta_h = 0.5$ and the right wall is cooled with $\theta_c = -0.5$ (resulting from Eq. (4.1)). A homogenous Dirichlet boundary condition ($\boldsymbol{u} = 0$) is applied for the velocity. It has been shown by Le Quéré and Behnia (1998) that the solution of the 2-D Boussinesq equation in this configuration becomes unsteady at critical Rayleigh number $\mathcal{R}a = 1.82 \cdot 10^8$ due to the instability mode that breaks the usual central-symmetry of the solution. Therefore, a steady state can be achieved for the chosen Rayleigh numbers.

We solve the unsteady and steady Navier-Stokes-Boussinesq equations, related to algorithms (3.13) and (3.17), respectively. The unsteady case is computed until the steady state with a single convection cell is reached, with a numerical tolerance of 10^{-9}. In parallel, the steady case is performed using a Rayleigh number continuation: a smaller value of the Rayleigh number is set initially and increased smoothly until reaching the correct value. At each stage, the computation starts from the solution obtained from the previous Rayleigh number simulation.

Two cases are simulated: **i)** a differentially heated square cavity and **ii)** a differentially heated cavity with an inner heated obstacle. For each of them, the horizontal and the vertical velocity profiles $u(y)$ and $v(x)$ at mid-domain ($y = 0.5$ and $x = 0.5$, respectively) are plotted and compared with numerical results by Le Queré (1991) and Moglan (2013). Moreover, for **i)**, we compare with the benchmark solutions by de Vahl Davis (1983) and Le Queré (1991): the maximum value u_{max} and v_{max} with their location y_{max} and x_{max}, the Nusselt number at the heated (left) wall and at the mid-domain, and the maximum and the minimum value of the local Nusselt number at $x = 0$ with their y-locations.

4.1.1 Differentially heated square cavity

Figure 4.1 offers a comparison of the current simulation with the numerical results of Wakashima and Saitoh (2004), who used a fourth-order finite difference method for the spatial discretization and a third-order backward finite difference scheme for the time integration, for $\mathcal{R}a$ ranging from 10^4 to 10^6. The temperature distribution and the streamlines at the steady state display a good agreement with the benchmark solution. The higher the $\mathcal{R}a$ number, the stronger is the natural convection flow in the cavity. A single convection cell is observed in the center of the cavity for $\mathcal{R}a = 10^4$ (Fig. 4.1d) during which the heat transfer is merely bulk heat transfer. Figures 4.1e and 4.1f however exhibit stronger convection with more rolls, when the boundary layer heat transfer dominates.

A more accurate validation is performed with respect to the spectral-accurate results of Le Queré (1991). We plot in Fig. 4.2 the horizontal (panel a) and the vertical (panel b) profiles of the velocity

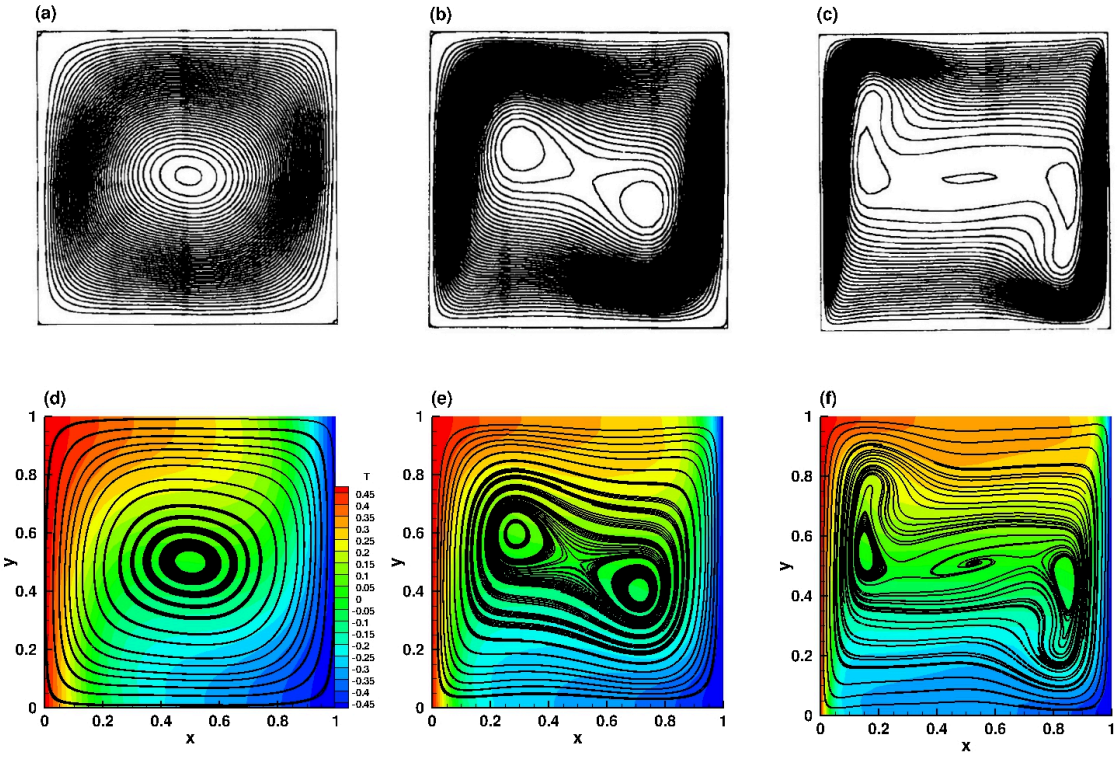

Figure 4.1: Natural convection of air for Ra ranging from 10^4 to 10^6 (from left to right) and $\mathcal{P}r = 0.71$. Temperature fields and streamlines at the steady state. Panels (a) to (c) correspond to the benchmark solution of Wakashima and Saitoh (2004). Panels (d) to (f) display our numerical results.

and compare the current simulation with data extracted from Le Queré (1991) for each of the three computed $\mathcal{R}a$ numbers. Results from Le Queré (1991) are represented by solid lines and the current simulation by symbols. A very good agreement can be noticed for each case. The thickness of the boundary layer is decreasing with increasing value of the temperature difference δT. Following the correlation of Bejan (2013), a viscous boundary layer with a dimensionless thickness of order of $\delta_\nu \sim 0.02$ should be present close to the vertical walls for $\mathcal{R}a = 10^6$. Accordingly, the mesh resolution should allow to capture these structures. We assess on the influence of the mesh resolution on the solution in Tab. 4.2. We report the L^2 and L^∞ norms of $\varepsilon_V = |V - V_{LQ}|$ (along $x-$direction) and

nbseg	$\|\|\varepsilon_U\|\|_2$	$\|\|\varepsilon_U\|\|_\infty$	$\|\|\varepsilon_V\|\|_2$	$\|\|\varepsilon_V\|\|_\infty$
40	$1.777477 \cdot 10^{-4}$	$5.617468 \cdot 10^{-4}$	$2.418556 \cdot 10^{-4}$	$7.203805 \cdot 10^{-4}$
80	$1.961756 \cdot 10^{-5}$	$5.463075 \cdot 10^{-5}$	$3.153492 \cdot 10^{-5}$	$9.160633 \cdot 10^{-5}$
120	$4.478622 \cdot 10^{-6}$	$1.518429 \cdot 10^{-5}$	$9.539112 \cdot 10^{-6}$	$2.891752 \cdot 10^{-5}$
160	$2.186721 \cdot 10^{-6}$	$6.181043 \cdot 10^{-6}$	$2.802694 \cdot 10^{-6}$	$9.789997 \cdot 10^{-6}$
200	$1.20101 \cdot 10^{-6}$	$3.666731 \cdot 10^{-6}$	$2.282512 \cdot 10^{-6}$	$5.690341 \cdot 10^{-6}$

Table 4.2: Error associated to the spatial discretization. Comparison with Le Queré (1991).

$\varepsilon_U = |U - U_{LQ}|$ (along $y-$direction) for different values of *nbseg*, from 40 to 200. The present

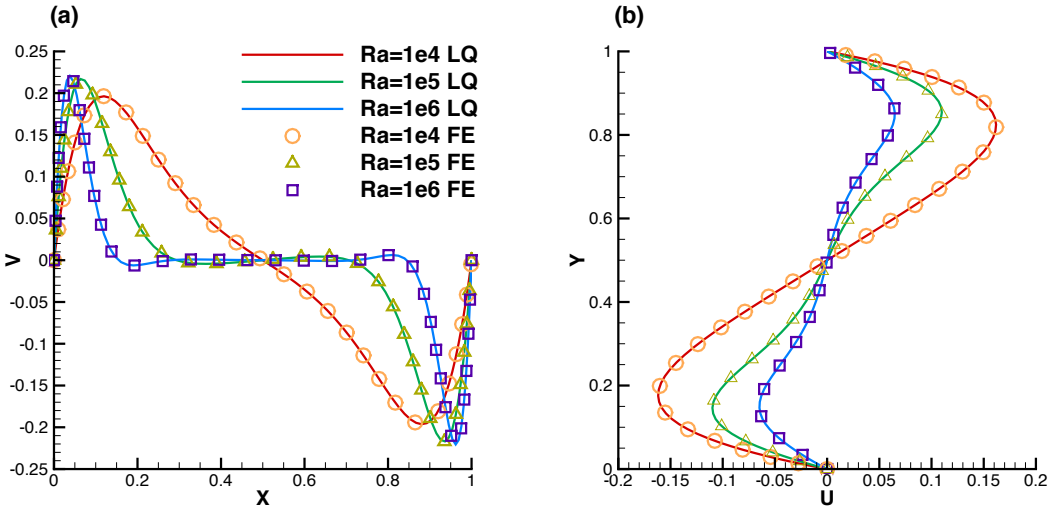

Figure 4.2: Natural convection of air in a differentially heated cavity for Ra ranging from 10^4 to 10^6 and $\mathcal{P}r = 0.71$. (a) Transversal velocity profile along the horizontal symmetry line. (b) Longitudinal velocity profile along the vertical symmetry line. Numerical results obtained using the present Newton method (symbols) with a mesh resolution of *nbseg* $= 80$; comparison with the spectral-accurate simulations by Le Queré (1991) (solid lines).

simulation is compared with the accurate solutions, V_{LQ} and U_{LQ}, of Le Queré (1991). Differences decrease when the mesh resolution is increased. We observe that errors of order of 10^{-5} are obtained for the 80×80 grid resolution, with a reasonable computational time of 14 seconds. All computations in this section are performed with a fixed triangular mesh, generated by the Delaunay algorithm starting with *nbseg = 80* points on each side of the square.

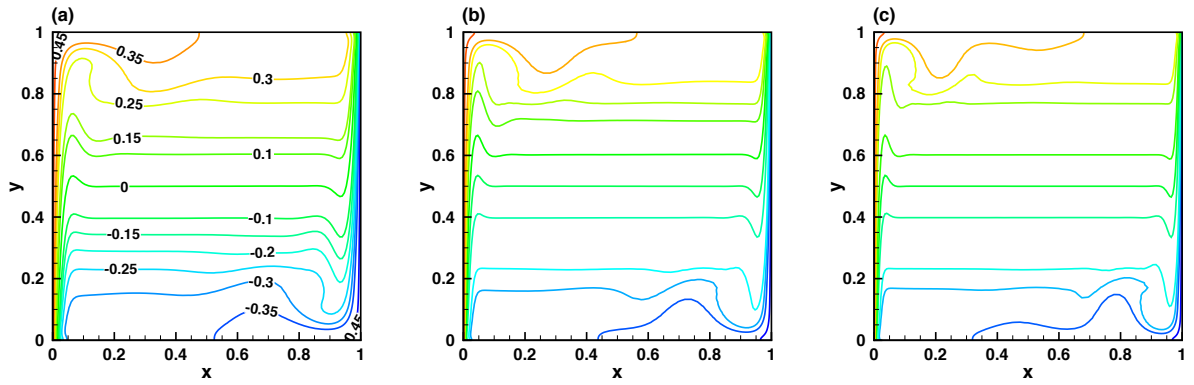

Figure 4.3: Natural convection of air. Temperature isolines at the steady state for (a) $Ra = 10^7$, (b) $Ra = 4 \cdot 10^7$, (c) and $Ra = 10^8$.

Higher $\mathcal{R}a$ number simulations were performed to test the robustness of our algorithm. We depict the temperature isolines at the steady state for $\mathcal{R}a = 10^7$, $4 \cdot 10^7$, and 10^8 in Fig. 4.3. One can observe the onset of detached regions along the upper and lower adiabatic walls for $\mathcal{R}a = 4 \cdot 10^7$, which is in agreement with observations of Le Quéré and De Roquefortt (1985). According to Le Quéré and

De Roquefortt (1985), this phenomenon is in part induced by the Neumann boundary conditions at the horizontal (top and bottom) walls. To assess for the steadiness of the solution, we plot in Fig. 4.4 the time evolution of the Nusselt number $\mathcal{N}u_0$ at the heated wall ($x = 0$) and $\mathcal{N}u_{1/2}$ at the mid-domain ($x = 0.5$). The Nusselt number in the center region of the cavity is defined as

$$\mathcal{N}u_{1/2} = \sqrt{\mathcal{P}r\mathcal{R}a} \int_0^1 \left(u\theta - \frac{\partial \theta}{\partial x} \right) \Big|_{x=0.5} dy. \tag{4.3}$$

The Nusselt at the hot wall becomes constant very soon when compared to $\mathcal{N}u_{1/2}$, which oscillates during a longer period and tends to the constant value of $\mathcal{N}u_0 = 16.5237$.

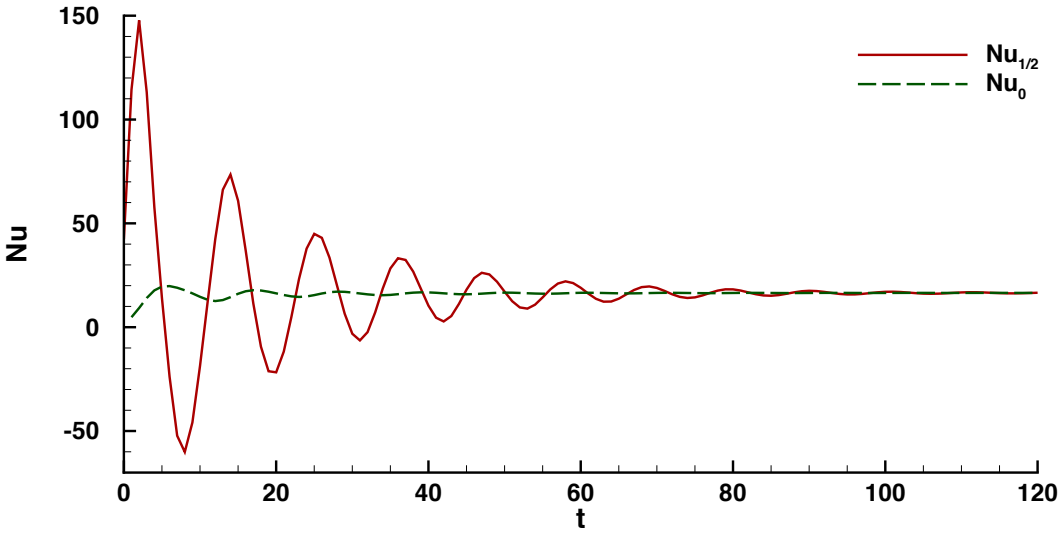

Figure 4.4: Natural convection of air. Time evolution of the Nusselt number at $x = 0$ and $x = 1/2$ for $\mathcal{R}a = 1 \cdot 10^7$.

Table 4.3 offers a more quantitative assessment of the accuracy of the present Newton method. The values of (u_{max}, y_{max}), (v_{max}, x_{max}) are compared to reference values from de Vahl Davis (1983) and Le Queré (1991) for $\mathcal{R}a$ ranging from 10^4 to 10^8. The Newton method gives results identical to reference values. Relative errors lower than 0.01% are obtained for $\mathcal{R}a = 10^5$ and 10^6. A relative difference of 0.43% is observed for $\mathcal{R}a = 10^6$ with respect to the reference solution of de Vahl Davis (1983), and a relative difference of 0.003% with the spectral accurate solution of Le Queré (1991). The highest discrepancy is noted for $\mathcal{R}a = 10^8$, but still offers reasonable agreement with benchmark values, within 0.52% error for u_{max} 5.57% for v_{max}. We compare moreover the average Nusselt number at the left vertical wall (the mean, the max, and the min) and at the mid-domain, since the Nusselt number will be largely used to compare the optimized configuration of a PCM, either for melting or solidification cycles in the next chapters. It is thus essential to ensure the accuracy of the computed value of this parameter. Excellent agreement with de Vahl Davis (1983) and Le Queré (1991) is obtained for all simulated $\mathcal{R}a$ numbers, with a relative error lower than 0.038%.

	u_{max} y	v_{max} x	$\mathcal{N}u_0$	$\mathcal{N}u_{1/2}$	$\mathcal{N}u_{max}$ y	$\mathcal{N}u_{min}$ y
$\mathcal{R}a = 10^4$	1.61782 0.826772	1.96272 0.11811	2.24487	2.24403	3.53218 0.141732	0.58497 1
de Vahl Davis (1983)	1.6178 0.823	1.9617 0.119	2.238	2.243	3.528 0.149	0.586 1
$\mathcal{R}a = 10^5$	3.47218 0.858268	6.85436 0.0629921	4.52172	4.52176	7.72 0.0787402	0.72797 1
de Vahl Davis (1983)	3.473 0.855	6.859 0.066	4.519	4.519	7.717 0.085	0.729 1
$\mathcal{R}a = 10^6$	6.48369 0.850394	22.0306 0.0393701	8.82521	8.82513	17.5344 0.0393701	0.979543 1
de Vahl Davis (1983)	6.463 0.850	21.936 0.0379	8.817	8.799	17.925 0.0378	0.989 1
Le Queré (1991)	6.48344 0.850	22.0559 0.038	8.8252	8.8252	17.5360 0.039	0.97946 1
$\mathcal{R}a = 10^7$	4.69349 0.88189	2.19517 0.023622	16.5237	16.5194	39.3455 0.015748	1.36675 1
Le Queré (1991)	4.69862 0.879	2.21118 0.021	16.523	16.523	39.3947 0.018	1.36635 1
$\mathcal{R}a = 10^8$	3.20182 0.929134	2.09841 0.015748	30.2353	30.1604	87.3469 0.00787402	1.92085 1
Le Queré (1991)	3.21875 0.928	2.22239 0.012	30.225	30.225	87.2355 0.008	1.91907 1

Table 4.3: Natural convection of air in a square cavity. Comparison with the results by de Vahl Davis (1983) and Le Queré (1991) for $\mathcal{R}a = 10^4$ to 10^8.

4.1.2 Differentially heated cavity with an inner heated square

Thermally driven cavity including a heated square obstacle is computed in this section. We consider the same configuration presented in Sec. 4.1.1 and a square domain with isothermal boundary conditions is added in the initial set-up. This kind of basic configuration could be representative of telecommunication outdoor cabinet applications, in which the use of passive cooling solutions have begun to be more and more investigated. Indeed, inside an outdoor cabinet, electronic equipments generate heat when active. The study of the flow structures within the enclosure with obstacles was studied experimentally and numerically by Moglan (2013). The simplified model of cavity with rectangular heated obstacles investigated by Moglan (2013) will be reproduced in this section to test the robustness of our numerical algorithm.

A linear distribution of the temperature is imposed initially in the motionless air inside the cavity. The obstacle is maintained at a dimensionless hot temperature $\theta_h = 0.8$, with a no-slip boundary condition for the velocity. The solutions for $\mathcal{R}a = 10^4$, 10^5, 10^6 and $\mathcal{P}r = 0.71$ are compared with the result obtained by Moglan (2013), who used an immersed boundary method with a FD code using high order schemes for time and spatial discretization.

The temperature distribution in the cavity when the steady-state is reached, for each of the three computed $\mathcal{R}a$ numbers, are reported in panels (a) to (c) of Fig. 4.5. The temperature gradient gives rise to a clockwise circulation and when $\mathcal{R}a$ is increased, vertical thermal boundary layers form distinctly along the differentially heated sidewalls and the obstacle. Consequently, higher is the Rayleigh number, the hot temperature in the center of the domain is more rapidly advected by the natural convection flow into the cold part of the cavity. It is worth noting that for $\mathcal{R}a = 10^6$ in panels (c) and (f), a stagnant fluid with a stratified temperature forms in a small portion of the fluid between the cold wall and the obstacle.

We present a more accurate validation in panels (d) to (f) of Fig. 4.5. The transversal velocity profiles along the $x-$axis are plotted and compared with the numerical data of Moglan (2013) for each cases. A good agreement can be observed, with a relatively small difference between the extremum of the velocity, while the shape of the velocity profile match well.

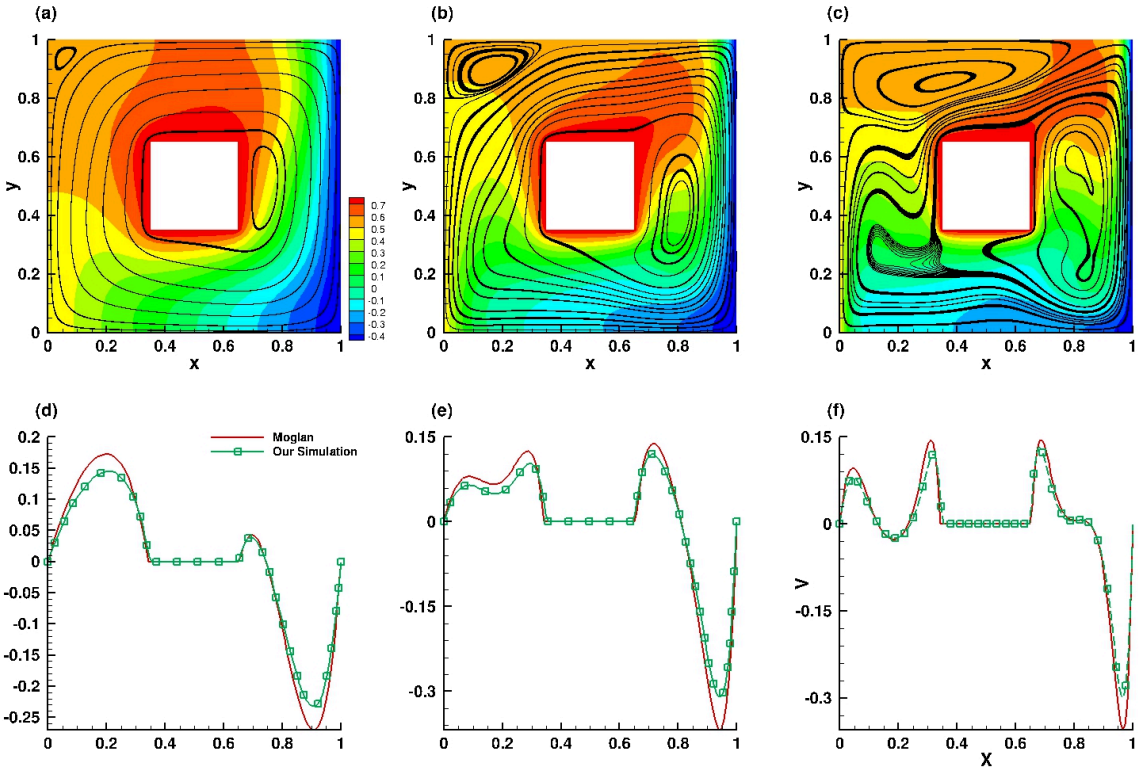

Figure 4.5: Natural convection of air in a differentially heated cavity with an inner heated square for $\mathcal{R}a$ ranging from 10^4 to 10^6. Temperature field and streamlines (top) and transversal velocity profile along the horizontal symmetry lines (bottom). Results obtained using the present Newton method (red solid line), with mesh resolution *nbseg* $= 80$; comparison with the finite difference code of Moglan (2013).

4.2 Natural convection of water inside a square cavity

We simulate in this section the natural convection of water in a differentially heated cavity. A further difficulty is introduced compared to the previous validations by taking into account the non-linear variation of the density in the buoyancy force. Pure water exhibits a non-linear density variation for $T < 10.2\,°\text{C}$ with a maximum at $T_m = 4.0293\,°\text{C}$. We use below the following density-temperature relationship suggested in Gebhart and Mollendorf (1977):

$$\rho(T) = \rho_m \left(1 - w\,|T - T_m|^q\right), \tag{4.4}$$

with $\rho_m = 999.972$ [kg/m^3], $w = 9.2793 \cdot 10^{-6}$ [$(°C)^{-q}$], and $q = 1.894816$. The bouyancy term $f_B = g(\rho_{ref} - \rho)/\rho_{ref}$ in Eq. (2.6) becomes after scaling:

$$f_B(\theta) = \frac{\mathcal{R}a}{\mathcal{P}r\,\mathcal{R}e^2}\frac{1}{\beta\delta T}\frac{\rho(\theta_f) - \rho(\theta)}{\rho(\theta_f)}, \tag{4.5}$$

where $\beta = (1/\rho_m)\,(d\rho/dT)$ is the thermal expansion coefficient with the value $\beta = 6.91 \cdot 10^{-5}$ [(K)$^{-1}$] (Scanlon and Stickland, 2004).

We consider a cavity of height $H = 0.38$ m filled with liquid pure distilled water. This problem was investigated experimentally and numerically by Giangi et al. (2000); Kowalewski and Rebow (1999); Michalek and Kowalewski (2003). The height H of the cavity is considered as a the length scale of the problem, $L_{ref} = H$. We choose $T_{ref} = T_h - T_c = 10K$ in order to compare our simulation with the numerical results of Michalek and Kowalewski (2003), and define the following scaling:

$$V_{ref} = \frac{\nu_l}{H} \quad \Longrightarrow \quad t_{ref} = \frac{H^2}{\nu_l} \quad \Longrightarrow \quad \mathcal{R}e = 1. \tag{4.6}$$

The non-dimensional parameters describing the problem result from the physical properties of water given in Tab. 4.1: $\mathcal{R}a = 2.518084 \cdot 10^6$ and $\mathcal{P}r = 6.99$.

The initial temperature is linearly distributed with a hot (non-dimensional) temperature $\theta_h = 1$ at the left wall and a cold temperature $\theta_c = 0$ at the right wall. The top and the bottom of the cavity are adiabatic and no-slip boundary condition $\boldsymbol{u} = 0$ is applied for the velocity.

The temperature field of the steady state is presented in Fig. 4.6a. Unlike the natural convection of air, in which two distinct boundary layers along the vertical walls and a stagnant and thermally stratified fluid in the core of the fluid flow were observed, an anomalous variation of the temperature is pointed out around the iso-line $\theta = \theta_m = 0.40293$ for the natural convection of water. This anomalous thermal variation of water density, is clearly discernible in the streamlines of the steady flow in Fig. 4.6b. Two recirculating zones are formed in the flow: a lower (abnormal) recirculation in the vicinity of the cold wall where $\theta < \theta_m$ and an upper (normal) one where the density decreases with temperature ($\theta > \theta_m$).

Following the above observations, a higher mesh resolution should be applied around θ_m. We thus define a $\mathbb{P}_1$ function $\Phi(\theta)$ by the following hyperbolic-tangent function similar to Eq. (2.20):

$$\Phi(\theta) = \frac{1}{2}\left\{1 + \tanh\left(\frac{\theta_m - \theta}{R_\Phi}\right)\right\}, \tag{4.7}$$

with $R_\Phi = 0.02$. The function $\Phi(\theta)$ and the two components of the velocity are used to compute the metric for the mesh adaptivity. $\Phi(\theta)$ is used to track θ_m. The velocity allows to refine the boundary

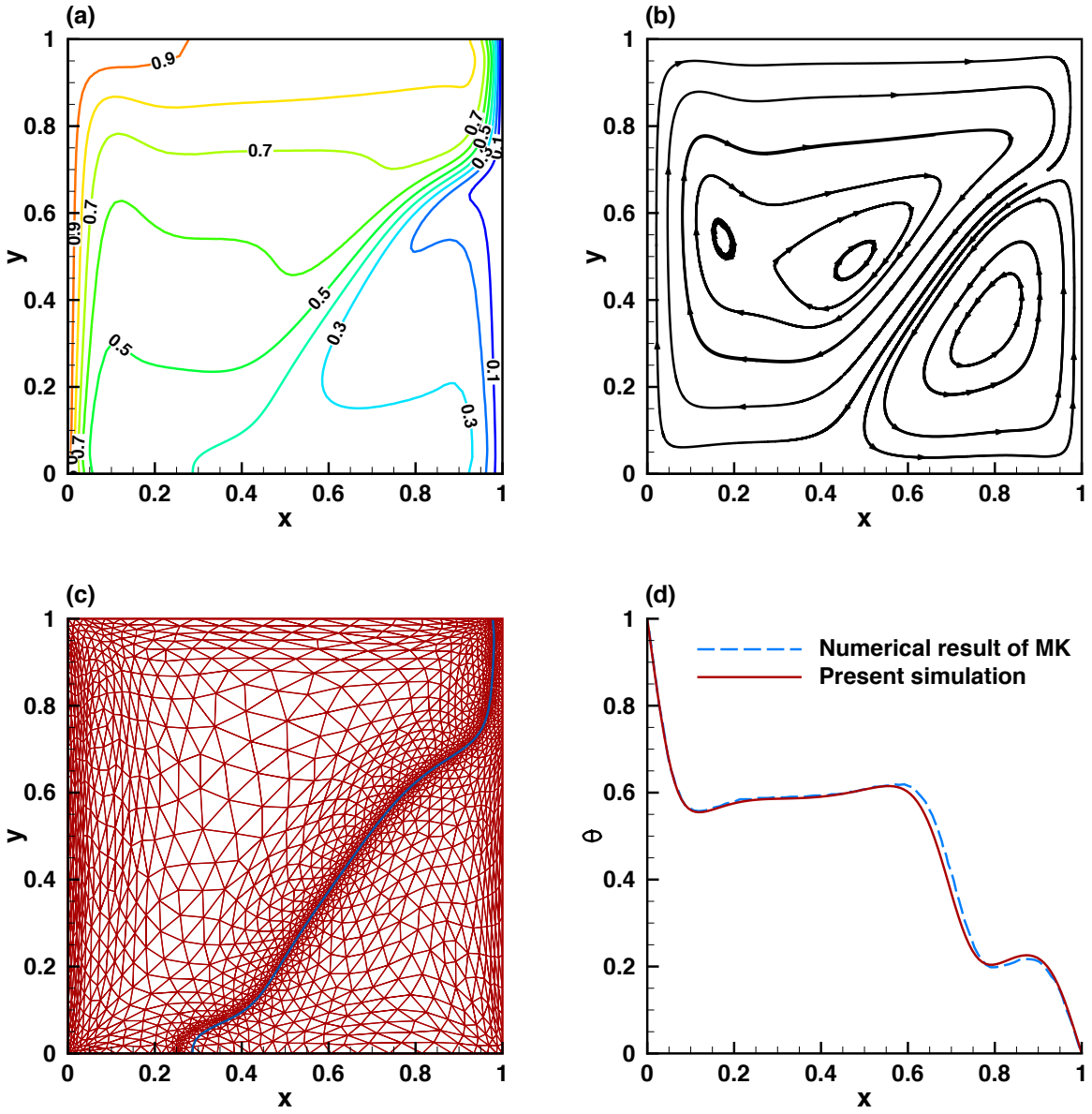

Figure 4.6: Natural convection of water in a differentially heated cavity with non-dimensional parameters: $\mathcal{R}a = 2.518084 \cdot 10^6$ and $\mathcal{P}r = 6.99$. (a) Iso-lines of the temperature at the steady state. (b) Streamline of the steady flow. (c) Illustration of the mesh adaptivity. The mesh is refined along the dimensionless temperature iso-line $\theta = \theta_m$, due to the density variation. (d) Temperature profile along the horizontal symmetry line. Comparison with the numerical results of Michalek and Kowalewski (2003).

layer regions. To reduce the impact of the interpolation on the global accuracy, since our algorithm is optimized to afford the mesh refinement every time step, we use both $\Phi(\theta^n)$ and $\Phi(\theta^{n+1})$ in the adaptivity procedure.

The final mesh is displayed in Fig. 4.6c. The mesh is clearly refined along the line $\theta = \theta_m$, where the structure and the extent of the two recirculating zones should be captured, and along the vertical walls

where the heat transfer is dominated by the boundary layer transfer. Furthermore, as expected in the relatively stagnant fluid region, a coarser mesh is applied.

A more accurate comparison is given in Fig. 4.6d. The temperature profile $\theta(x)$ along the horizontal symmetry line of the cavity is in good agreement with the numerical results of Michalek and Kowalewski (2003) obtained with FV and FD codes (FLUENT and FRECONV3V), commonly used in the heat transfer community. Differences are visible in the vicinity of the maximum density line, region where our mesh is well refined to capture the separation line between the two recirculation zones. It should be noted that the FLUENT simulations in Michalek and Kowalewski (2003) are performed with a fixed uniform grid with 380×380 nodes, while our adapted grid has only 3422 triangles.

4.3 Concluding remarks

We can conclude from sections. 4.1 and 4.2 that our Newton method is able to deal efficiently with the two-dimensional Navier-Stokes-Boussinesq problem, either with linear or non-linear buoyancy forces.

Our simulations of natural convection of air including or not obstacles are in good agreement with the numerical solutions of Le Queré (1991) and Moglan (2013). Excellent agreement with de Vahl Davis (1983) and Le Queré (1991) has also been observed for the value of the average Nusselt number at the heated wall.

The challenging case of the natural convection of water was used to demonstrate the robustness of the 2D code. Good agreement with the numerical simulations of Michalek and Kowalewski (2003) was noticed. The advantage of the mesh adaptivity was clearly shown by using a total number of grid points 40 times lower than in the simulation of Michalek and Kowalewski (2003). The refined mesh along the line θ_m have permitted to solve more accurately the structures and the extent of the two recirculating zones.

The properties of the run presented in this chapter are summarized in Tab. 4.4 for the highest value of the $\mathcal{R}a$ number, $\mathcal{R}a = 10^6$. The interest of solving the steady equation, when steady state could be reached, is clearly emphasised when regarding the number of iterations and the CPU time. $1,164$ iterations and 3162.86 CPU seconds are necessary to achieve the steady state with a tolerance of 10^{-6} for the natural convection of water by solving the unsteady equation, while only 20 iterations and 51.1662 CPU seconds are needed with the steady algorithm.

	Case	Nb of iterations	Nb of triangles	Nb of d.o.f.	CPU time (s)
Air	unsteady	164	$2,413$	$16,133$	338.527
	steady	6	$2,312$	$15,558$	14.0465
Air with obstacle	unsteady	157	$3,489$	$23,354$	436.405
	steady	6	$2,967$	$19,933$	15.9369
Water	unsteady	$1,164$	$3,422$	$22,639$	3162.86
	unsteady	20	$2,960$	$19,629$	51.1662

Table 4.4: Description of the runs for natural convection cases with $\mathcal{R}a = 10^6$.

We simulate in the next chapter the melting and the solidification of a PCM. Aside from the non-linear convection terms in the momentum and the energy Eqs. (2.12) - (2.14), a further difficulty will arise from the non-linearity introduced by the source term $\partial(CS)/\partial t$ in Eq. (2.14).

5 Numerical simulations of phase change materials in 2D configurations

The purpose of this chapter is to validate our numerical method by simulating convective phase-change problems. A discussion on numerical parameters is given first, followed by a sequence of validations computing different physical and geometrical configurations.

The Newton algorithm (3.10) is now solved throughout the whole domain containing liquid and solid phases. When compared to the previous validation, two new non-linearities are now added: the Carman-Kozeny penalty term in the momentum equation and the enthalpy source term in the energy equation. The Carman-Kozeny penalty term is used to ensure zero velocity in the solid region and the enthalpy non-linear source term is included to model the phase-change in the energy equation. Following the same idea as in the natural convection validation cases in Chapter 4, the non-linearity in the body force is gradually added. We consider first the linear form of $f_B(\theta)$ by investigating the melting of various PCMs within several shapes of the containers. Then, the challenging case of water freezing, characterized by a non-linear variation of the density (see Eq. (4.4) in Chapter 4), is simulated.

Details about the parameter settings are first given in Sec. 5.1: the characteristics of the mushy-zone, the mesh adaptivity and the initial condition are discussed in detail. Second, the melting of n-octadecane and Gallium are presented in Secs. 5.2 and 5.3. The physical properties of n-octadecane and Gallium used in our simulations are reported in Tab. 5.1.

	ρ kg/m^3	μ kg/(m s)	h_{SL} kJ/kg	c_p J/(kg K)	k W/(m K)	T_f K	β 1/K
Octadecane	774	$3.9 \cdot 10^{-3}$	244	2180	0.152	301	$8.5 \cdot 10^{-4}$
Gallium	6093	$1.81 \cdot 10^{-3}$	80.16	381.5	32	301	$1.2 \cdot 10^{-4}$

Table 5.1: Physical properties of n-octadecane and Gallium PCM.

Then, in Secs. 5.4 and 5.5 we demonstrate the capability of our code to deal with different shapes of the domain. The melting of a cylindrical PCM with inner heated tubes is presented in Sec. 5.4 and the solid crust formation in a highly distorted mesh is simulated in Sec. 5.5. Finally, the water freezing case is performed in Sec. 5.6. Besides the non-linear definition of the body force, the striking feature of the water freezing simulation is the tracking of several interfaces, namely the solidification front and the anomalous thermal variation of density. Our result is qualitatively compared with the experimental results of Kowalewski and Rebow (1999).

5.1 Parameter settings

We present in this section the setting of the main numerical parameters. The influence of the penalty term $A(\theta)$ in the momentum equation is discussed first, namely the value of the Carman-Kozeny constant C_{CK}. Second, details about the mesh adaptivity parameters are given. Finally, the initialization process is described.

5.1.1 The Carman-Kozeny model

When a single domain method is applied, the Carman-Kozeny penalty term is used to bring to zero the velocity in the solid region, through an intermediate mushy zone. In the mushy zone, at the leading term, the momentum Eq. (2.13) becomes

$$\frac{\partial \boldsymbol{u}}{\partial t} = A\boldsymbol{u}. \tag{5.1}$$

with solution

$$\boldsymbol{u} = \boldsymbol{u}_0 \exp(At). \tag{5.2}$$

Since $A < 0$, see Eq. (2.23), we infer that $\lim_{A\to\infty} \boldsymbol{u} = 0$. It is thus expected that, when C_{CK} is large enough, the value of the velocity in the solid region will tend to zero. The effect of this constant on the melting and the solidification processes has attracted some attention in the literature.

The influence of C_{CK} in the location of the solid-liquid front was investigated by Kheirabadi and Groulx (2015). They have concluded that high C_{CK} values induce a slower melting rates, and conversely small values result in unphysical predictions of the melting front evolution. They also noticed that C_{CK} and the melting temperature range $\Delta T_\varepsilon = T_{\varepsilon 2} - T_{\varepsilon 1}$ are dependent of one another: different values of ΔT_ε require different values of C_{CK} to obtain the same melting front location.

Mathura and Krishna (2017) studied the effect of the mushy zone constant and its influence on the melt fraction, vortex strength and the amount of heat storage. They have shown that increasing C_{CK} leads to a decrease of the convection strength and consequently to a decrease of the heat transfer rate. These studies show the necessity of choosing an appropriate value of this parameter. Because of the semi-solid state and porous nature of the mushy zone, the choice of the value of this constant is still an open problem.

To assess on the influence of the Carman-Kozeny constant, we simulate the melting of a n-octadecane PCM within a square enclosure with the following dimensionless parameters: $\mathcal{R}a = 3.27 \cdot 10^5$, $\mathcal{P}r = 56.2$ and $\mathcal{S}te = 0.045$. See Sec. 5.2 for a detailed description. Different values of C_{CK} are used ranging from 10^6 to 10^{20}. The local liquid fraction function $L_f(\theta)$ in Eq. (2.23), is regularized as:

$$L_f(\theta) = 1 - \frac{1}{2}\left\{1 + \tanh\left(\frac{\theta_f - \theta}{R_{ck}}\right)\right\}. \tag{5.3}$$

The value of θ_{ck} is set in order to have the sharp variation of the derivative of $\mathrm{d}L_f/\mathrm{d}\theta$ near the new phase appearing in the system, *i. e.* liquid for melting ($\theta_{ck} = \varepsilon$), and solid for freezing ($\theta_{ck} = \theta_f$) (see also Danaila et al. (2014)). This is to ensure that the velocity in the solid region is correctly set to $\boldsymbol{u} = 0$.

The computed velocity in the solid phase is reported in Tab. 5.2 for different values of C_{CK}, ranging from 10^6 to 10^{20}. Increasing the constant C_{CK} leads to lower values of the velocity in the solid, as it was expected. However, even though it is generally assumed that a large value for C_{CK} must be set, the exact value of this constant could influence the accuracy of the results.

C_{CK}	A_{max}	u_{solid}	v_{solid}
10^6	$1.62935 \cdot 10^{11}$	$-9.8058 \cdot 10^{-14}$	$-3.20216 \cdot 10^{-10}$
10^{10}	$1.62937 \cdot 10^{15}$	$1.09832 \cdot 10^{-17}$	$-3.23176 \cdot 10^{-14}$
10^{20}	$1.62935 \cdot 10^{25}$	$2.7011 \cdot 10^{-26}$	$-3.18493 \cdot 10^{-24}$

Table 5.2: The influence of the constant of Carman-Kozeny on the values of the velocity in the solid region.

We compare the location of the melting front with the experimental data of Okada (1984). Figure 5.1a displays the location of the phase-change interface for four values of C_{CK}: 10^6, 10^{10}, 10^{15}, and 10^{20}. Very good agreement with the experimental result of Okada (1984) is obtained for $C_{\text{CK}} = 10^6$. Increasing the constant C_{CK}, results in artificially slowing the propagation of the melting front. This behavior could be explained by the profile of the velocity $U = \sqrt{\Sigma_i u_i^2}$, plotted as a function of temperature θ following the line $y = 0.9$ (Fig. 5.1b). For a value of $C_{\text{CK}} = 10^6$, the velocity is zero in the expected temperature interval $[-0.01, 0.01]$, corresponding to the characteristic length of the regularization zone $R_{ck} = \varepsilon = 0.01$. However, imposing too large values of C_{CK}, induces a larger temperature interval in which the velocity is forced to be zero. For $C_{\text{CK}} = 10^{20}$, the velocity is canceled up to $\theta = 0.1$, *i. e.* an artificial mushy zone 10 times larger than the initial case $C_{\text{CK}} = 10^6$.

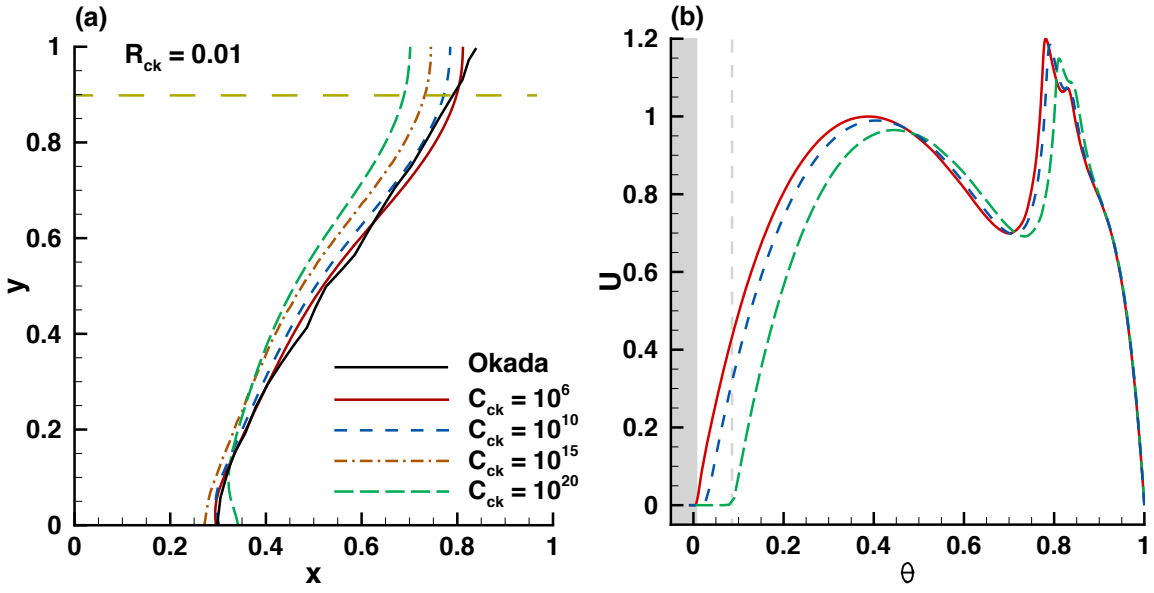

Figure 5.1: Location of the interface at $t = 78.7$ for the melting of the PCM. (a) Computations using different values of C_{CK} ranging from 10^6 to 10^{20} and comparison with experimental data of Okada (1984). (b) Velocity profile following the line $y = 0.9$ with respect to the temperature.

To obtain the same location of the melting front using different values of C_{CK}, one should thus decrease the smoothing radius parameter R_{ck}. Several values of R_{ck} ranging from ε to $\varepsilon/4$ were tested and the results are plotted in Fig. 5.2. Decreasing R_{ck} by a factor of 2 (Fig. 5.2 a) and 4 (Fig. 5.2 b), results in a merging of the location of the solid-liquid interface for different values of R_{ck}. It is however worth noting that decreasing the regularization interval R_{ck} implies a greater mesh resolution to solve accurately the strong gradient induced by discontinuities at the solid-liquid interface. We thus set for all subsequent simulations $C_{\text{CK}} = 10^6$ and $R_{ck} = \varepsilon$, which corresponds to the best fit with the experimental result of Okada (1984) and the less time-consuming configuration.

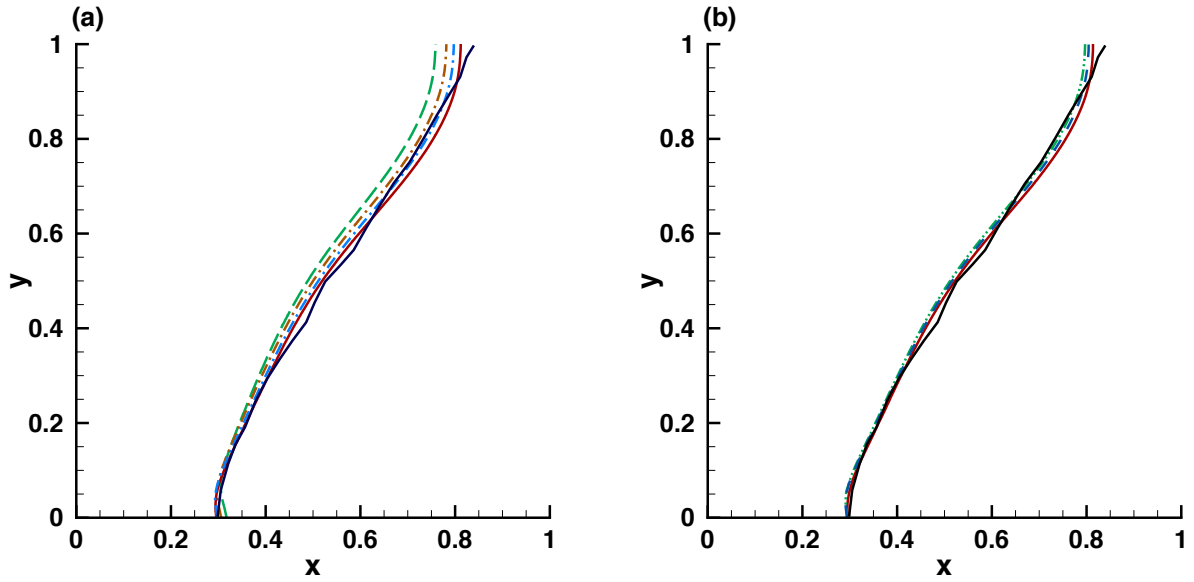

Figure 5.2: Location of the interface at $t = 78.7$ for the melting of the PCM. Computations using different values of C_{CK} ranging from 10^6 to 10^{20} and different values of the smoothing radius R_{ck}: (a) $R_{ck} = \varepsilon/2$, (b) $R_{ck} = \varepsilon/4$.

5.1.2 Mesh adaptativity

The use of mesh adaptation proved mandatory in the present simulation of PCM melting to obtain accurate results within reasonable computational time. For the melting case, we used five metrics intersection to adapt the mesh, based on $S^{n+1}, S^n, T^{n+1}, T^n$, and $\boldsymbol{u}^{n+1}$. To reduce the impact of the interpolation on the global accuracy for time-depending problems, we consider the metrics computed from actual (at t_{n+1}) and previous (at t_n) values, for the same variable used for adaptivity (see also Belhamadia et al. (2004a)).

The mesh adaptation strategy requires to set the interpolation error level *errh*, the minimum and the maximum edge sizes, *hmin* and *hmax*, and the *adaptratio* parameter, which defines the ratio for a prescribed smoothing of the metrics. The minimum size of triangles and the interpolation error level are set in order to capture the smaller length scale, mainly the boundary layer structure close to the wall, and to solve accurately the large gradient at the solid-liquid interfaces. The error level is adapted for each variable on which the metrics are computed. A default value *errh = 0.02* is defined for T and $\boldsymbol{u}$, and *errh = 0.2* for S. The scale for boundary layers in natural convection flow along a vertical wall is given by Eq. (2.25). For high-Prandtl simulations, the thermal boundary layer is thinner than

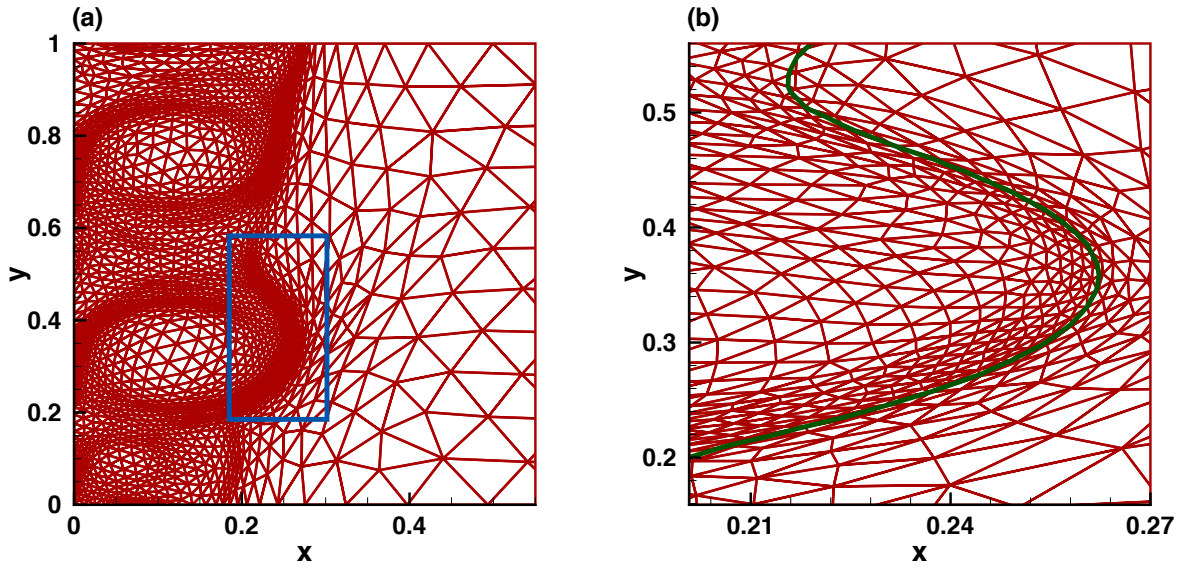

Figure 5.3: Adapted mesh during simulation of PCM melting. (a) $4,211$ triangles: the mesh is refined around the melting front $\theta = 0$ and in the fluid where velocity gradients exist. (b) zoom showing the variation of the mesh size around the temperature isoline $\theta = 0$.

the viscous boundary layer, and conversely for low-Prandtl fluids the viscous boundary layer is thinner than the thermal one. In our simulations, the values of the Rayleigh number, in the range 10^6 to 10^8, and the Prandtl number of order of 50, lead to a dimensionless thickness of the thermal boundary layer of order of $\delta_\theta \sim 10^{-3}$. For the same range of Rayleigh numbers and Prandtl number of order of 0.1, we obtain a dimensionless thickness of the viscous boundary layer of $\delta_\nu \sim 10^{-2}$. The minimum edge-length is therefore set to $hmin = 10^{-3}$. Moreover, we fix the maximum triangle size to avoid generating too large triangles. Mesh adaptivity is performed at each time step and offers a refined discretization of the regularization region where sharp gradients have to be accurately captured. Figure 5.3 shows the adapted mesh during the melting of Gallium PCM in a square cavity. The mesh is remarkably refined around the melting front (Fig 5.3b), localized by the temperature isoline $\theta = 0$. This is also the case in the fluid region around the convection cells, while a coarser mesh is applied in the solid. The typical number of triangles of the generated adaptive mesh is $4,000$. Non-adapted grids offering the same spatial resolution everywhere inside the computational domain would have resulted in $N_t = 9.94 \cdot 10^{10}$ triangles. Consequently, mesh adaptivity greatly helps in reducing the computational time. The mesh adaptivity capability to capture several interfaces is the striking feature of our method. Its capability to track efficiently two solidification fronts during PCM solidification or the density inversion interface during the water freezing will be discussed in Sec. 5.6.

5.1.3 Initialization

For the melting process, the PCM is initially solid and the temperature is set to a cold temperature θ_c, below the temperature of fusion θ_f. However, increasing abruptly the boundary temperature to a hot temperature θ_h, above the temperature of fusion, in order to initiate the melting process is numerically complicated because of the strong temperature gradient between the wall and the PCM. A first usual approach consists of setting a very thin fluid layer of thickness $\delta x \sim 0.01$ with isothermal temperature

in the vicinity of the hot wall (see Danaila et al. (2014); Belhamadia et al. (2004a)). A different approach, is applied in the current work. The temperature at the hot wall and the Rayleigh number are increased smoothly over a small time interval to reach the correct values of θ_h and $\mathcal{R}a$. This approach has a physical significance and is more robust when high Rayleigh number simulations are performed. Concerning the solidification stage, mainly the water freezing case, a 'hot' and a 'cold' restarts are used. The first approach consists of establishing a steady state regime by solving first the steady Eq. (3.14) and dropping then smoothly the temperature of the cold wall below the temperature of fusion. The second approach sets directly θ_c below the temperature of fusion and considers initial motionless fluid, thus inducing huge gradients near the wall, which requires very small triangles therein.

5.2 Melting of a n-octadecane PCM in a square cavity

We start the validation of our algorithm for phase-change systems by simulating the melting of n-octadecane PCM within a differentially heated square cavity. Three cases are investigated:
• *Benchmark* $\#1$: Experimental investigation by Okada (1984) of the melting of n-octadecane PCM.
• *Benchmark* $\#2$: Experimental and numerical investigations by Gong et al. (2015) of the melting of a PCM inside a transparent building brick.
• *Benchmark* $\#3$: Numerical comparison with various numerical methods, presented by Bertrand et al. (1999), for the melting of a PCM at high $\mathcal{R}a$.

The physical parameters used in our simulations are given in Tab. 5.3.

		$\mathcal{R}a$	$\mathcal{P}r$	$\mathcal{S}te$	δt	V_{ref}
n-octadecane	Bench $\#1$	$3.27 \cdot 10^5$	56.2	0.045	10^{-1}	$\frac{\nu_l}{H}$
	Bench $\#2$	$2.48 \cdot 10^8$	50	0.072	10^{-3}	
	Bench $\#3$	10^8	50	0.1	10^{-5}	
Gallium		$7 \cdot 10^5$	0.0216	0.046	10^{-3}	$\frac{\nu_l}{H}$

Table 5.3: Dimensionless parameters for the simulation of melting of a n-octadecane PCM.

The experimental investigation of Okada (1984) in *Benchmark* $\#1$ consists of a differentially heated square cavity of dimensions 1.5 cm $\times$ 1.5 cm. The left and the right walls are isothermal and the top and the bottom walls are adiabatic. No-slip boundary conditions are prescribed on the velocity over the whole $\partial\Omega$.

To ensure that we obtain a grid-converged solution, we first perform simulations with different mesh resolutions for *Benchmark* $\#1$ by keeping the minimum edge length constant and increasing *hmax* from 10^{-2} to 10^{-1}. A snapshot of the adapted mesh at $t = 78.7$ is reported in Fig. 5.4.

– *Mesh* $\#1$ (Panel a): $N_t = 48,247$ triangles and $314,203$ degree of freedom (d.o.f),
– *Mesh* $\#2$ (Panel b): $N_t = 21,093$ triangles and $143,202$ d.o.f,
– *Mesh* $\#3$ (Panel c): $N_t = 2,870$ triangles and $318,974$ d.o.f,
– *Mesh* $\#4$ (Panel d): $N_t = 820$ triangles and $5,544$ d.o.f.

For all considered meshes, one can observe the refined grid at the boundary layer region near the walls, due to the high velocity gradients, and along the interface $\theta = 0$. Coarser mesh is applied in the solid region. We note however that a ratio of 10 is set for *hmax* between *Mesh* $\#1$ and *Mesh* $\#4$,

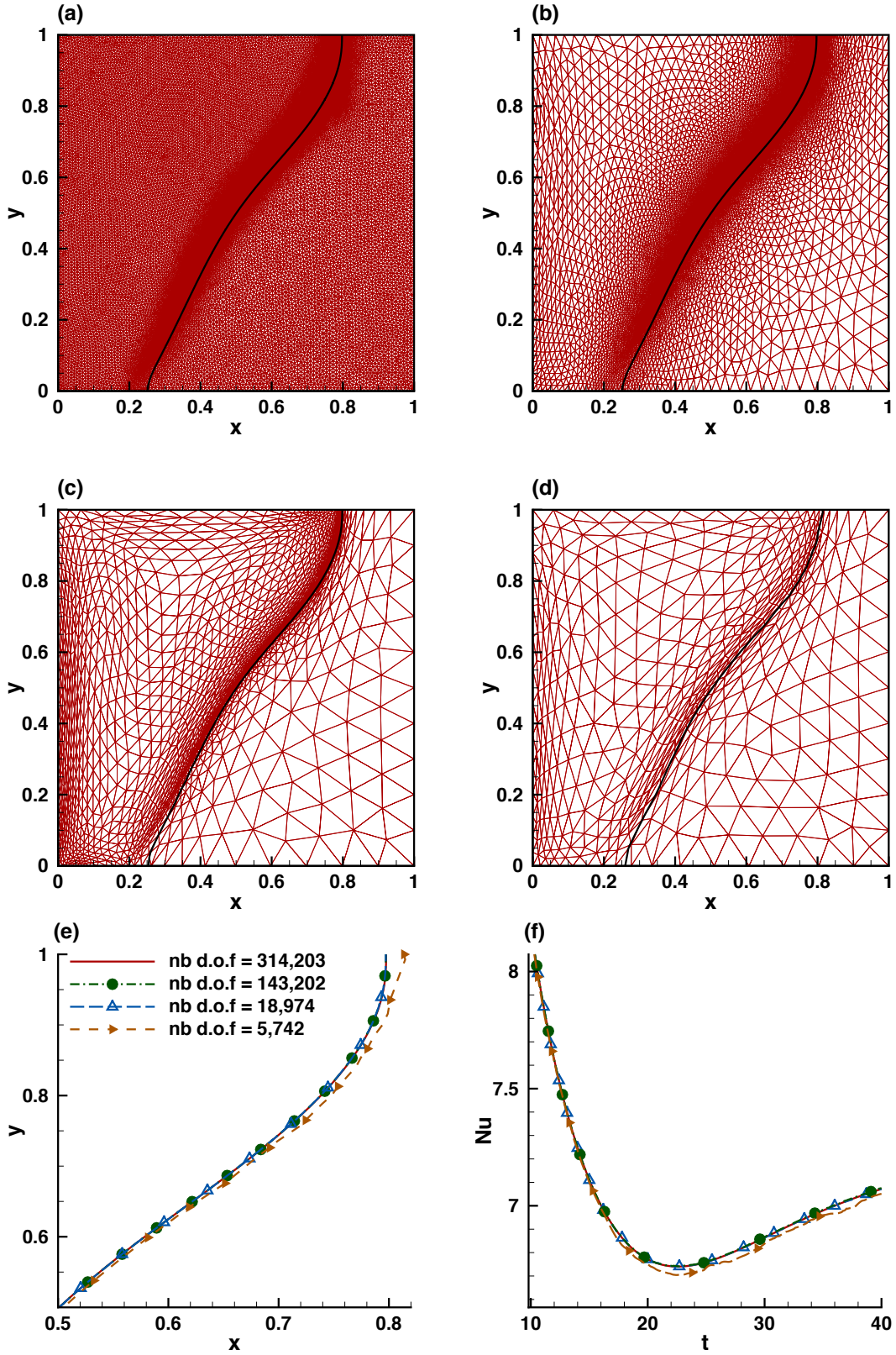

Figure 5.4: Benchmark #1. Influence of the mesh resolution on the numerical solution at dimensionless time $t = 78.7$. The mesh is refined around the melting front $\theta = 0$ and in the fluid where velocity gradients exist. Solid lines denote the solid-liquid interface. Number of triangles: (a) $48,247$, (b) $21,093$, (c) $2,870$, (d) 820. The location of the interface (e) and the time evolution of the Nusselt number (f) are compared.

resulting into a ratio of 50 for the number of d.o.f. using a $\mathbb{P}_2$ discretization for θ. Simulations are performed using $\delta t = 10^{-2}$ to ensure small time discretization errors. The location of the solid-liquid interface and the time evolution of the Nusselt number related to each of the four adapted meshes are compared in Figs. 5.4e and 5.4f. The maximum difference for the location of the melting front occurs at the top of the cavity since the highest velocity is reached in this region because of the clockwise recirculation of the flow. We also compare the position of the solid-liquid interface along x-direction at $y = 1$. The coarser grid (*Mesh* #4) exhibits the highest gap with respect to the most refined *Mesh* #1, with a relative error of 2.14% for the location of the melting front at the top of the cavity and by overestimating the heat transfer of an order of 3.83%. For *Mesh* #3, in which the mesh resolution is increased by a factor of 3 compared to the coarse mesh, differences of 0.042% and 0.039% are noticed for both $\mathcal{N}u$ and the interface position. Finally, for *Mesh* #2, variations lower than 0.01% are obtained. However, since a balance between the accuracy and the computational time is sought, the subsequent simulation are performed using the parameters of *Mesh* #3, summarized in Tab. 5.4. Solutions using *Mesh* #3 were performed with only 2876.39 CPU seconds, while 12 CPU hours were needed for *Mesh* #1.

hmin	hmax	adaptratio	errh	nbvx
10^{-3}	0.1	1.5	0.01	$50,000$

Table 5.4: Mesh adaptivity parameters used for *Mesh* #3.

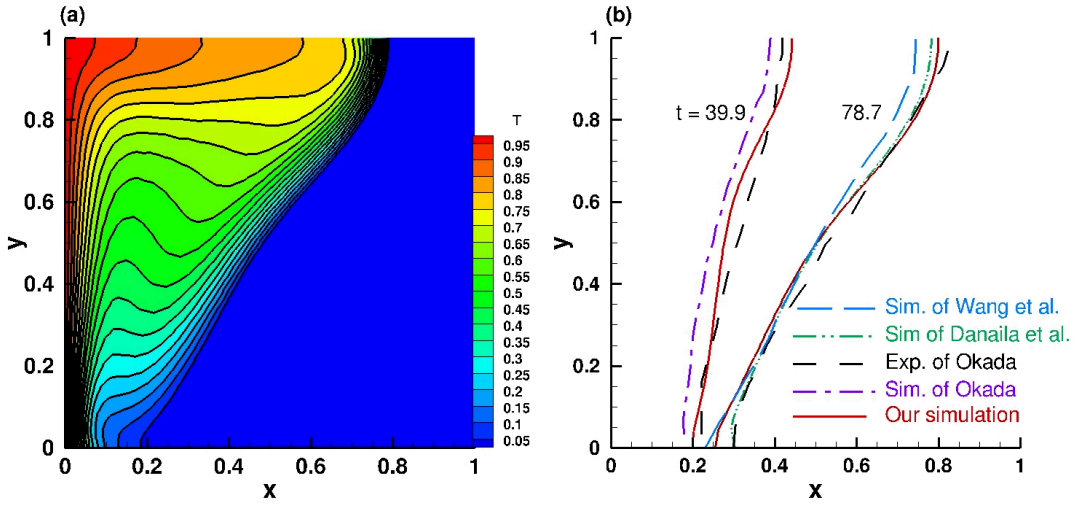

Figure 5.5: *Benchmark* #1. (a) Temperature isoline at $t = 78.8$. (b) Location of the interface. Comparison with experimental data of Okada (1984) and numerical solutions of Danaila et al. (2014) and Wang et al. (2010a) for two time instants ($t = 39.9$ and 78.8).

We present in Fig. 5.5 the computed solution for *Benchmark* #1 case using *Mesh* #3. Panel (a) displays the temperature distribution of the PCM at dimensionless time $t = 78.7$. The enclosure is heated from the left and the melting PCM expands from the left to the right (the blue color denotes the solid region). A non-planar shape of the phase-change interface could be observed due to effect of the natural convection in the liquid phase. Further comprehensive descriptions of the influence of the liquid flow on the interface will be discussed in Chapter 6. Panel (b) compares the location of the solid-liquid

interface with experimental investigation of Okada (1984). For two particular time instants, $t = 39.9$ and $t = 78.7$, we could compare our results to available experimental (Okada, 1984) and numerical (Okada, 1984; Wang et al., 2010a; Danaila et al., 2014) data. In the experimental set-up, the author reported that the top of the PCM was not perfectly insulated and consequently the growth of the upper part of melting front was delayed. The current work agrees well with the experimental results of Okada (1984) at the bottom part of the melting front. However, our results overestimate the location of the front in the top part of the cavity, which could be related to the experimental heat loss mentioned by the author. Moreover, our results are qualitatively in a better agreement with experimental data than previously published numerical results. This is a direct consequence of the precise tracking of the melting front achieved by the mesh adaptivity performed at each time step. Wang et al. (2010a) used a FV code with a fixed mesh of resolution $[60 \times 60]$, and Danaila et al. (2014) used a FE method with viscosity penalty.

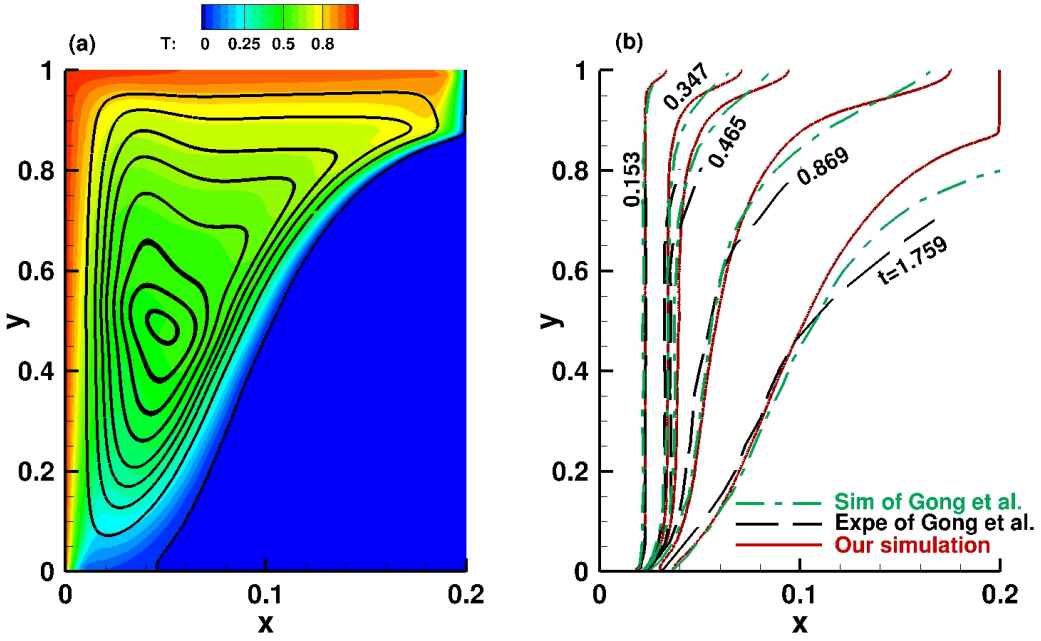

Figure 5.6: *Benchmark* #2. (a) Temperature distribution, streamlines, and solid-liquid interface at dimensionless time $t = 1.759$. (b) Comparison of the location of the solid-liquid interface, with both experimental and simulation results of Gong et al. (2015), for five time instants ($t = 0.153$, 0.347, 0.465, 0.869, and 1.759).

Numerical results for *Benchmark* #2 are depicted in Fig. 5.6. Gong et al. (2015) investigated the melting of octadecane PCM inside a transparent building brick of dimensions 15.2 cm $\times$ 3 cm. The numerical simulation is performed using $\delta t = 10^{-3}$ and a total runtime of $19,231$ CPU seconds using $4,198$ triangles. Figure 5.6a illustrates the temperature distribution in the melting PCM, the streamlines, and the phase-change interface obtained by the present finite element simulation. Panel (b) compares the location of the melting front for five particular time instants: $t = 0.153$, 0.347, 0.465, 0.869, and 1.759, with numerical and experimental data by Gong et al. (2015). Their numerical simulations were based on the thermal lattice Boltzmann method (TLBM), in which the natural convection was solved by LBM and the temperature equation was solved by a finite difference scheme using the enthalpy method. The difficulty here, compared to the first validation case, is the presence of a stronger

natural convection flow in the fluid due to the higher value of the Rayleigh number. We notice a very good agreement with both numerical and experimental data of Gong et al. (2015).

A last validation case for the n-octadecane PCM is also investigated to test the robustness of the method. Bertrand et al. (1999) compiled results provided by five different authors (Lacroix, Le Quéré, Gobin-Vieira, Delannoy and Binnet-Lacroix). Results provided by these authors will be hereafter referred to as (say) 'Lacroix, from Bertrand et al. (1999)'. They attempted a first comparison by taking several numerical methods to compute the basic configuration presented in this section. Two investigators among the five failed to predict the process and showed unrealistic behaviors (see Figs. 5.7 and 5.8): Lacroix and Delannoy seem to be insufficiently converged (Fig. 5.7), and Binet-Lacroix overestimates the average Nusselt number by more than 30% (Fig. 5.8). Hence, this collection of results allows us to compare our numerical method and check whether or not realistic results are obtained for complex physical configurations.

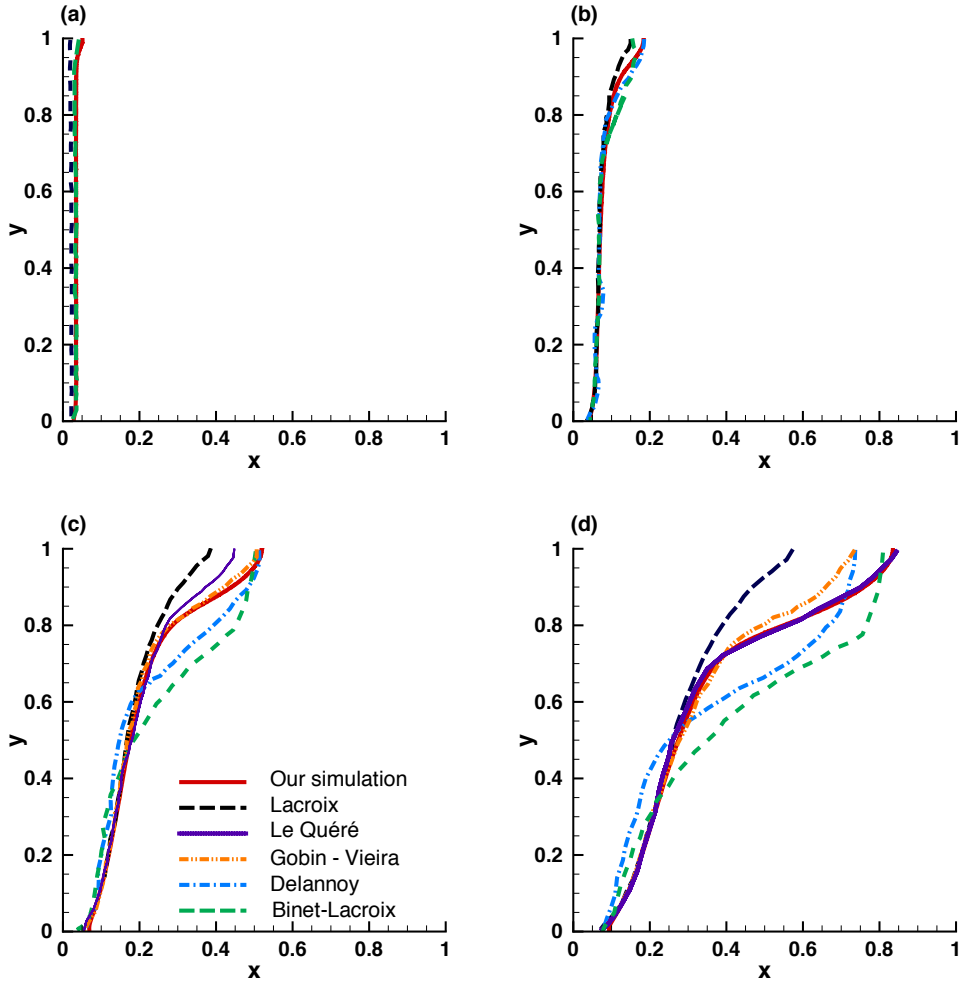

Figure 5.7: *Benchmark* #3. Location of the solid-liquid interface at dimensionless time (panels a to d) $t = 0.25$, $t = 1$, $t = 3$, and $t = 5$, compared with five simulations presented by Bertrand et al. (1999).

We inspect the melting front position (Fig. 5.7), the temporal evolution of the liquid fraction L_f and the Nusselt number $\mathcal{N}u$ at the left wall ($x = 0$) (Fig. 5.8), for each of the five results presented by Bertrand et al. (1999). For the liquid fraction, the initial solid state corresponds to $L_f = 0$, while

$L_f = 1$ indicates the complete melting of the PCM. The phase-change interface position for four time steps, $t = 0.25$, $t = 1$, $t = 3$ and $t = 5$ is represented in Fig. 5.7. Our results are for each case in fairly good agreement with those of Gobin and those of Le Quéré. Gobin used a front-tracking method using a coordinate transformation with a finite volume method with a 62×42 grid. Le Quéré solved a single domain model using a second order scheme with a finite volume method with a 192×192 grid (Gobin and Le Quéré (2000)). The time evolution of the liquid fraction and the Nusselt number are plotted in Fig. 5.8. A very good agreement is obtained with Gobin and Le Quéré. A relative difference, less than 2% is noticed for the Nusselt number, and a dispersion, smaller than 4%, for the melted fraction. The high value of the Rayleigh number, $\mathcal{R}a = 10^8$, results in a very demanding numerical test. The high velocity, inducing a very narrow thermal boundary layer can lead to unrealistic results and some numerical methods have failed. The interest of the mesh adaptation is clearly evidenced since a typical number of triangles of $N_t = 7,000$ was used during the simulation, which required $40,522$ CPU seconds.

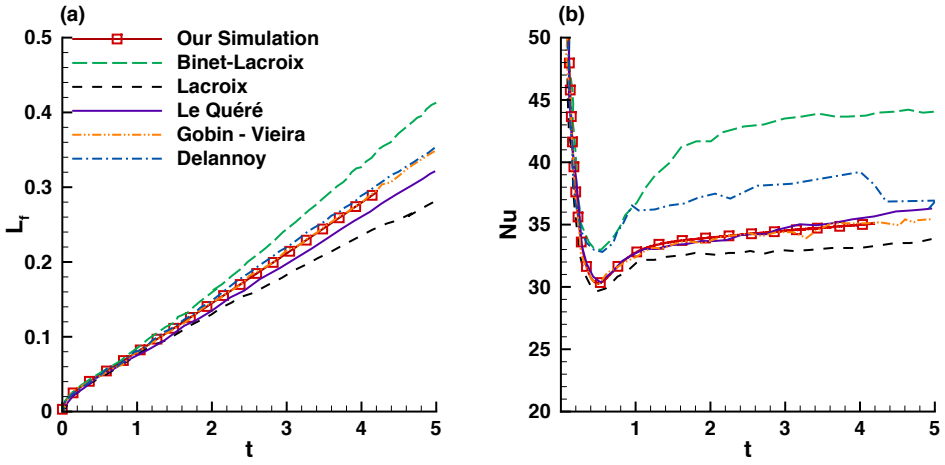

Figure 5.8: *Benchmark #3*: $\mathcal{R}a = 2 \cdot 10^8$, $\mathcal{P}r = 50$ and $\mathcal{S}te = 0.1$. Time evolution of the liquid fraction (a) and the Nusselt number (b). Comparison with five simulations presented by Bertrand et al. (1999).

5.3 Melting of Gallium in a rectangular cavity

The melting of tin or Gallium in a rectangular cavity, which corresponds to low-Prandtl fluids, was a controversial case since Dantzig (1989) raised the question whether the convection in the fluid is mono-cellular or multi-cellular. The experimental result exhibits indeed a mono-cellular structure, while many researchers claim this observation to be incorrect. Prior to Dantzig (1989) note, both experimental and numerical results supported a single cell solution in the fluid phase. Later, simulations provided solutions with multicellular flow. During the comparison exercise investigated by Bertrand et al. (1999), Le Quéré and Couturier-Sadat have predicted a different shape of the front corresponding to low-Prandtl simulation, induced by the multi-cellular structures of the flow in the melted PCM. Le Quéré and Gobin (1999) showed that the multi-cellular structures result from the hydrodynamic instabilities during the conduction regime before the onset of convection. Moreover, the numerical investigation of Hannoun et al. (2003), testing the influence of the mesh resolution and the numerical method's order, indicates clearly that mono-cellular observation is caused by a problem of convergence of the numerical solution. It can be due to the grid size or inconsistencies in the mathematical model.

Therefore, this test case simulating the melting of Gallium is a relevant exercice to test the consistency of our method. To capture the very small cell during the first step of the melting, Hannoun et al. (2003) used a $800 \times 1,120$ fixed grid in a rectangular domain of dimensions 6.35 cm $\times$ 8.89 cm. The authors have reported that the melting solution up to 32 s required about 980 CPU hours on a Compaq Alpha (667 MHz, ev67) processor. A maximum of $4,820$ triangles were necessary with our adaptive method, and only 4 CPU hours were spent to reproduce the numerical result of Hannoun et al. (2003) up to the final time 280s, on an Intel (2.8 GHz, Core i7) processor.

The time evolution of the flow is presented in Fig. 5.9. The enclosure is heated from the left (vertical) wall and the horizontal walls are adiabatic and no-slip. Dimensionless parameters of the run and properties of Gallium are given in Tabs. 5.1 and 5.3. Temperature field, streamlines and position of the melting front are displayed for several time instants: $t = 0.0015$, 0.006, 0.01, and 0.019. These values were chosen to visualize the merging of convection cells in the fluid flow and correspond to physical times $20s, 85s, 155s, 280s$ in Hannoun et al. (2003). The number of rolls was considered as a validation criterion by several authors (Hannoun et al., 2003; Cerimele et al., 2002; Giangi and Stella, 2000). Three cells are observed at $t = 0.006$ (Fig. 5.9). The number of cells decreases later through a process of roll merging, as it was also reported by Le Quéré and Gobin (1999) and Hannoun et al. (2003). Our numerical results are in good agreement with the observations of Hannoun et al. (2003), Cerimele et al. (2002) and Giangi and Stella (2000). The adapted mesh corresponding to $t = 0.019$ is illustrated in Fig. 5.9e. The mesh is well refined along the isoline $\theta = 0$ denoting the solid-liquid interface, and around the convective cells.

The time evolution of the Nusselt number at the heated vertical wall is plotted in Fig. 5.9f. One can note that the quasi-steady evolution of $\mathcal{N}u$, observed in Fig. 5.8 for high-Prandtl fluid simulations, is not recovered. This is in agreement with the stability analysis of Le Quéré and Gobin (1999), showing that the Nusselt number becomes unsteady starting from a critical time, for Rayleigh numbers greater than 10^5 and low-Prandtl numbers, while no instability could be found whatever the value of $\mathcal{R}a$ for high-$\mathcal{P}r$ cases. The first slight oscillation at the earlier time steps corresponds to the onset of the convective flow induced by the first instability of the conductive regime. It is followed by a nearly constant evolution of $\mathcal{N}u$ from $t = 0.01$ to $t = 0.02$ during the cell-merging process. High oscillations of the heat transfer are then observed, which is a feature of the onset of the second oscillatory instability. A zoom on the periodic evolution of the Nusselt number is displayed in Panel (f). Finally, the amount of heat transfer decreases starting with $t = 0.13$, when the front reaches the cold (right) vertical wall.

5.4 Melting of a cylindrical PCM with inner heated tubes

Cases presented in Secs. 5.3 and 5.2 considered phase change problems evolving in a simple geometry, a rectangular box. A more complex geometry, suggested by Luo et al. (2015), is simulated in this section. It consists of a cylindrical PCM of radius $R = 1$ with tube inclusions of different arrangements. The interest in studying this case is not solely the challenge of the complex configuration, but also the possibility to compare our results with those of Luo et al. (2015), obtained using a completely different model based on the Lattice Boltzmann Method. This configuration is also interesting from a practical point of view. Agyenim et al. (2010) pointed out that more than 70% of the PCM containers used for heat storage are using shell-tube systems.

We simulate three cases with one heated tube, four heated tubes, and nine heated tubes with the same total tube area. For the one heated tube case, the radius R_i of the inner tube is one-quarter of

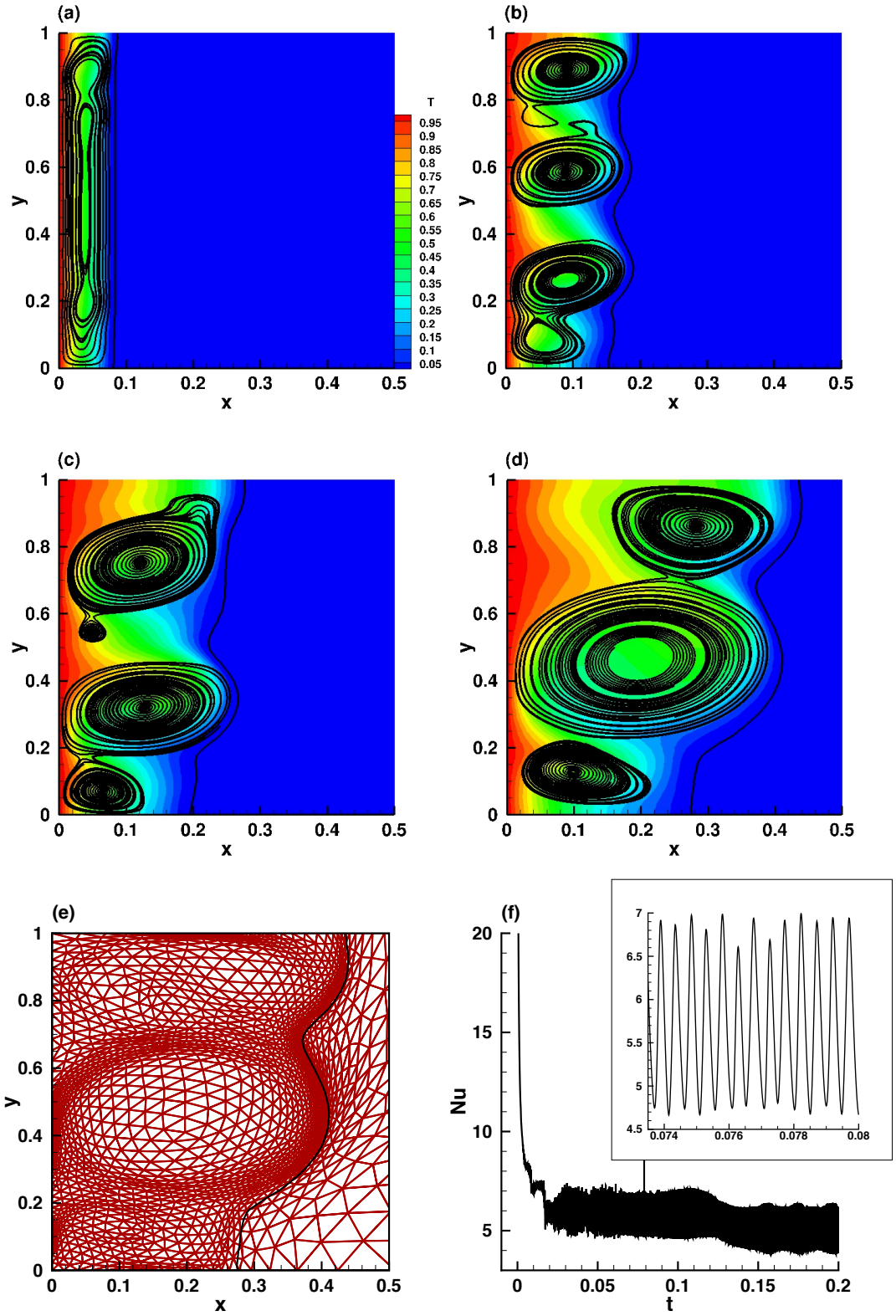

Figure 5.9: Melting of Gallium: temperature field, streamlines, and melting front for dimensionless time instants (panels a to d): $t = 0.0015$, 0.006, 0.01, and 0.019. Adapted mesh corresponding to $t = 0.019$ (e). Time evolution of the Nusselt number (f). For a better view of the convection cells, a ratio $2:1$ was used for the axes.

the outer radius ($R_i = R/4$), for four heated tubes $R_i = R/8$ and for nine heated tubes $R_i = R/12$. A Dirichlet boundary condition is applied to inner tubes $\theta = \theta_h$, and a Neumann boundary condition $\frac{\partial \theta}{\partial n} = 0$ is used at the outers. Homogenous Dirichlet boundary conditions ($\boldsymbol{u} = 0$) are prescribed on the velocity throughout all $\partial\Omega$. The physical parameters of the simulation are: $\mathcal{R}a = 5 \cdot 10^4$, $\mathcal{P}r = 0.2$ and $\mathcal{S}te = 0.02$. Only the half of the domain is simulated since the problem is axisymmetric for the investigated $\mathcal{R}a$ number. At $t = 0$, the PCM is completely solid with isothermal temperature θ_0 lower than the temperature of fusion. Immediately after the pipe placed on the center of the enclosure is heated, the melted layer expands in the radial direction. The mesh is refined initially around inner tubes, and is dynamically adapted at each time step around the melting front and the thermal boundary layer area.

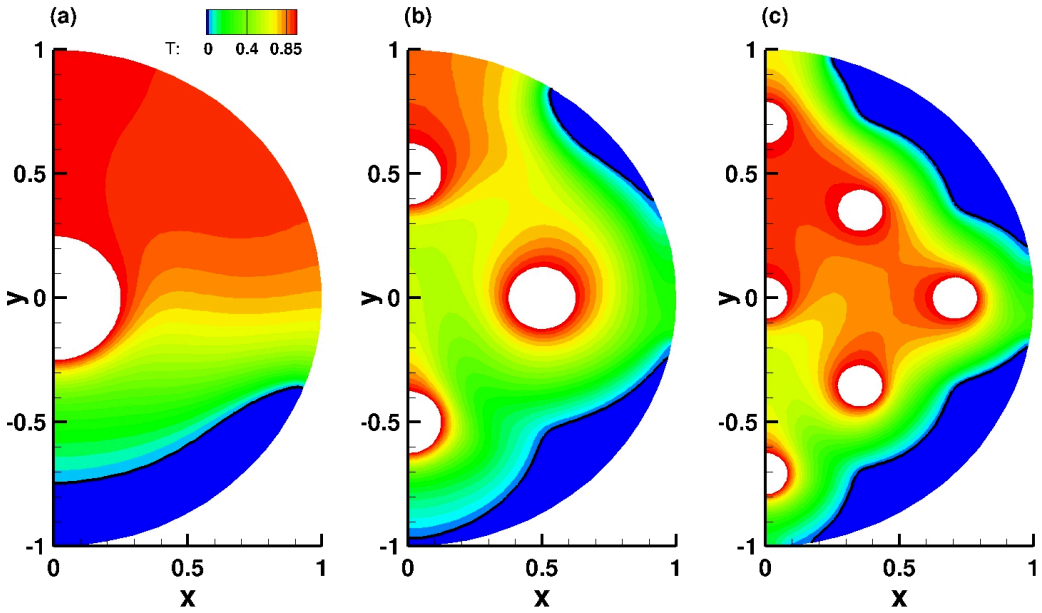

Figure 5.10: Temperature fields for the melting of a cylindrical PCM with inner heated tubes. Time instants corresponding to the same liquid fraction $L_f = 80\%$. Configurations with (a) one tube ($t = 2.5$), (b) four tubes ($t = 0.99$) and (c) nine tubes ($t = 0.4$). Melting fronts are represented with black lines (only half of the domain is simulated).

Figure 5.10 shows the temperature field and the position of the solid-liquid interface (black line) related to the three configurations for time instants corresponding to the same liquid fraction $L_f = 80\%$. The distribution of the inner tubes in the liquid phase influences directly the fluid motion and the shape of the melting front. The more the number of inner tubes, the stronger the natural convection is in the melted PCM. The shape of the solid-liquid interface displays complex patterns, depending on the space arrangement of the inner tubes. This is linked to the effect of the fluid motion in the presence of obstacles, as it was also noticed in Sec. 4.2. The mesh is adapted following the evolution of the melting interface, even after its separation in several distinct fronts touching the outer boundary (see Figs. 5.10b, c).

To estimate the efficiency of each configuration, we plot in Fig. 5.11 the time evolution of the liquid fraction L_f. By including more heated tubes, the heat transfer is enhanced, inducing a faster

melting time. The nine-tube configuration melts 5 times faster than the reference configuration with one tube. A reasonably close match with numerical results of Luo et al. (2015) is confirmed in Fig. 5.11a. We also assess on the effect of tubes arrangements for a fixed number of tubes. Three arrangements are simulated with 9 tubes and reported in Fig. 5.11b: central symmetry, inline, and staggered arrangements. The arrangement with central symmetry appears to provide a better heat transfer compared to the others. The inline and the staggered arrangements exhibit similar trends, with a slightly faster melting rate than the inline arrangement. The difference is explained by Luo et al. (2015) by the contribution of conductive heat transfer induced by the arrangements.

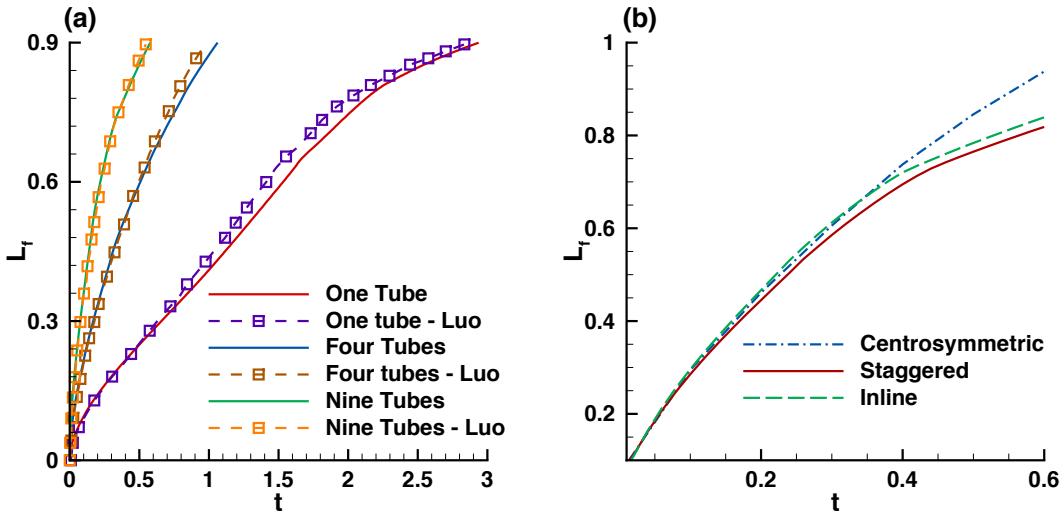

Figure 5.11: Time evolution of the liquid fraction for one, four, and nine heated tubes. (a) Comparison with numerical results of Luo et al. (2015) (b) comparison of different arrangements: central symmetry, inline, and staggered.

5.5 Solid crust formation in a highly distorted mesh

The solid crust formation inside a highly distorted domain, simulated by Nourgaliev et al. (2016) is considered in this section. Our emphasis here is on the ability of our method to tackle also solidification problems, especially in irregular domain (see Fig. 5.12).

The fluid is initially motionless with an initial dimensionless temperature $\theta_0 = 2$, above the temperature of fusion. The temperature of fusion is set to $\theta_f = 1.4$, according to Nourgaliev et al. (2016) parameters. It is worth noting that Nourgaliev et al. (2016) used $T_{ref} \neq T_f$ thus $\theta_f \neq 0$. The left side is set at cold temperature $\theta_c = 1.39$ in the initial stage while the right wall was kept constant at a hot temperature $\theta_h = 2$, so that a steady-state natural circulation should be established. The cold temperature at the left wall is then dropped smoothly to $\theta_c = 1$, below the temperature of fusion, starting the formation of a solid crust layer. The top and bottom walls are adiabatic.

The dimensionless parameters of the simulation are: $\mathcal{R}a = 1 \cdot 10^6$, $\mathcal{P}r = 0.1$ and $\mathcal{S}te = 4.854$. The scaling (4.2), which was also used by Nourgaliev et al. (2016), is used in the current simulation.

The temperature distribution, the streamlines, and the melting front position are reported in Fig. 5.12a and compared with the numerical results of Nourgaliev et al. (2016). These authors used a second-order discontinuous Galerkin finite element method and a viscosity-based technique to bring the velocity to zero in the solid region. We are qualitatively in good agreement with Nourgaliev et al. (2016). As expected, the high $\mathcal{R}a$ and $\mathcal{S}te$ dimensionless numbers, combined with the distorted domain, generate a complex vortical flow pattern in the melted PCM. Nourgaliev et al. (2016) presented a mesh convergence analysis and concluded that a 512×256 mesh resolution is needed to get a full resolution of the five vortical structures in Fig. 5.12b. Only $2,769$ triangles are used in the present simulation. This case illustrates again the capabilities of our mesh adaptivity algorithm.

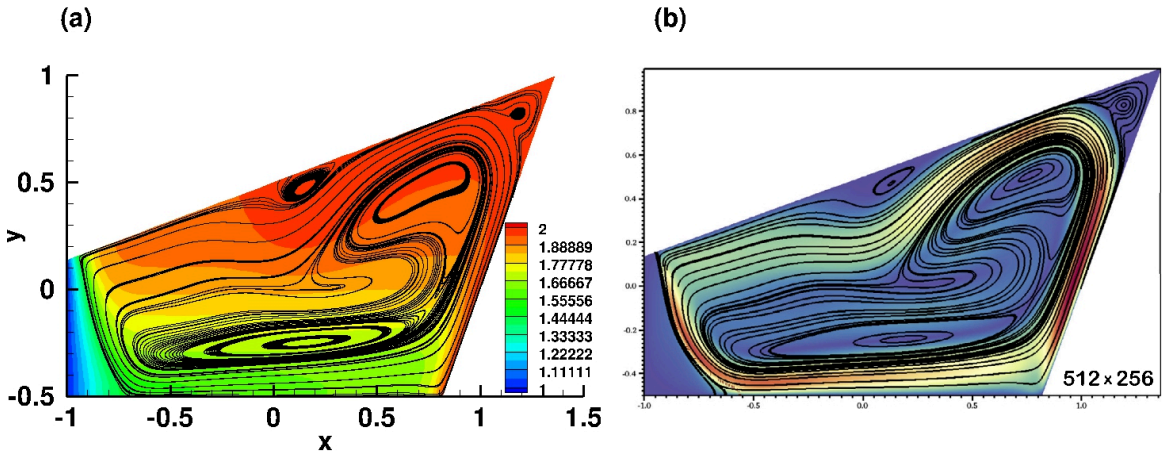

Figure 5.12: Solid crust formation in a distorted mesh. Temperature field and streamlines in our simulation (a) and Nourgaliev et al. (2016) (b).

5.6 Water freezing

We finally consider the difficult case of water freezing in a square cavity. After achieving the convection steady pattern in the cavity (see Fig. 4.6), freezing starts by dropping progressively the temperature of the cold (right) wall from $T_c = 0\,^{\circ}\text{C}$ to $T_c = -10\,^{\circ}\text{C}$. The dimensionless parameters describing the problem are: $\mathcal{R}a = 2.518084 \cdot 10^6$, $\mathcal{P}r = 6.99$ and $\mathcal{S}te = 0.125$.

Besides the complex fluid flow and the non-linear time evolution of the solid-liquid interface, the code have to handle the non-linear variation of the density presented in Eq. (4.4). Moreover, one can note that in addition to the non-linear formulation of $f_B(\theta)$ in Eq. (4.5), the coefficient $\mathcal{R}a \times 1/(\beta\delta T)$ is very large since the Boussinesq approximation imposes a value of $\beta\delta T \ll 1$. Since the assumption of constant conductivity is not accurate in the frame of water phase-change, $K(\theta)$ is regularized as:

$$K(T) = 1 + \frac{1}{2}\left(\frac{k_s}{k_l} - 1\right)\left\{1 + \tanh\left(\frac{T_f - T}{R_k}\right)\right\}, \tag{5.4}$$

with $k_s = 2.26$ and $k_l = 0.578$ and $R_k = 0.0075$. We also define $\varepsilon_1 = 0$ and $\varepsilon_2 = 0.0075$, to ensure a very thin mushy zone (see also Danaila et al. (2014)).

Figure 5.13a superimposes the experimental image from Kowalewski and Rebow (1999) with our numerical results for the same physical time $t_\varphi = 2340[s]$. The flow pattern in the liquid phase also corresponds very well qualitatively to the experimental image. Since a good agreement with the experiment was sought, the simulation was performed with very small time steps ($\delta t = 10^{-5} \approx 0.014[s]$), but still reasonable grids ($2,500$ triangles) were generated due to the efficiency of the adaptivity algorithm. The discrepancy between the experimental interface and the current simulation comes principally from the model, which neglects the three-dimensional effects, the supercooling of water and realistic boundary conditions (see Giangi et al. (2000); Kowalewski and Rebow (1999); Michalek and Kowalewski (2003)).

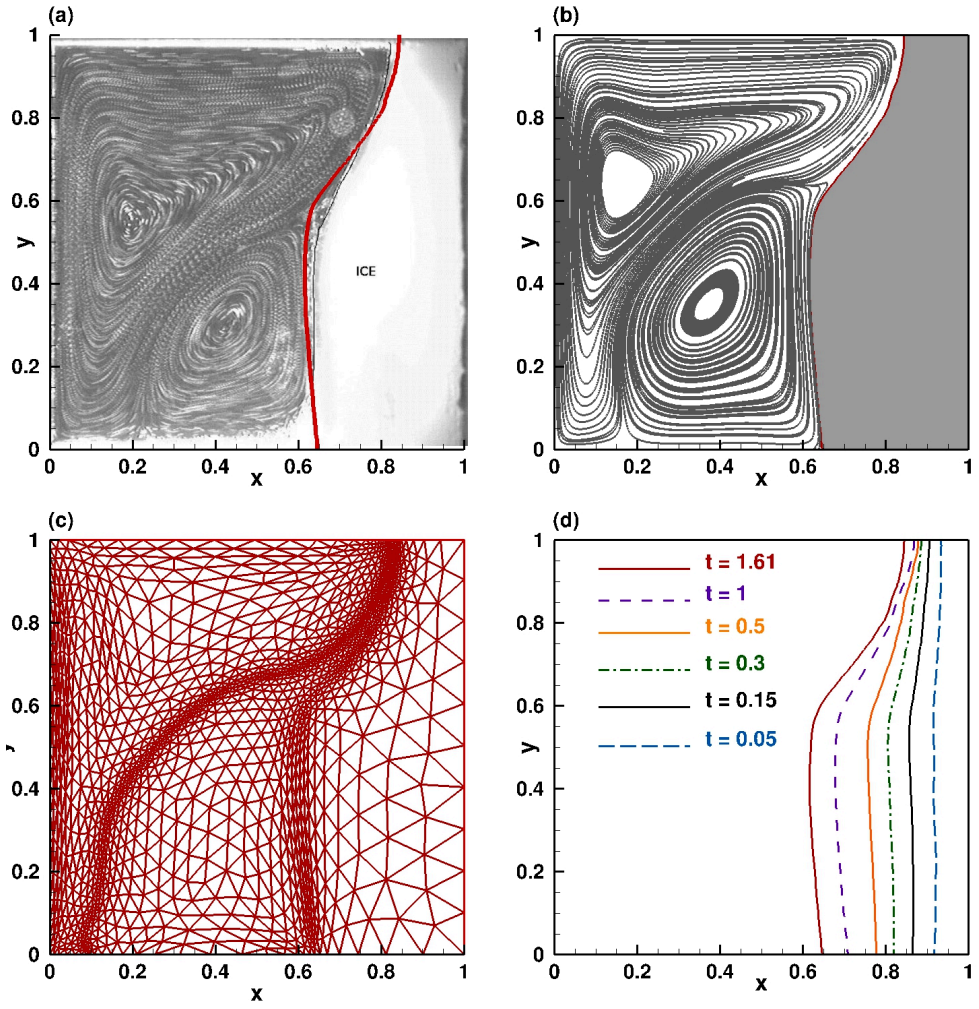

Figure 5.13: Freezing of pure water. Configuration at physical time $t_\varphi = 2340[s]$ (t = 1.61): (a) experimental image from Kowalewski and Rebow (1999); the thick red line represents the solid-liquid interface computed with the present method, (b) computed streamlines showing the two recirculating zones in the fluid phase, (c) finite-element mesh refined along the solid-liquid interface ($T = 0^oC$) and also along the line of maximum water density ($T = 4^oC$) (d) location of the solidification front for several time instants: from $t = 0.05$ (corresponding to physical time $t_\varphi = 70[s]$) to $t = 1.61$ ($2340[s]$)

The source term $S(\theta)$ is added to the metrics calculation presented in Sec. 4.2 to track the solidification front. The mesh is thus refined along the line θ_m through the function $\Phi(\theta)$ defined in Eq. (4.7), the solid-liquid interface defined by $\theta = 0$ and in the boundary layer regions. We use both $\Phi(\theta^n)$ and $\Phi(\theta^{n+1})$ and $S(\theta^n)$ and $S(\theta^{n+1})$ in the adaptivity procedure. The final mesh is displayed in Fig. 5.13c, clearly showing that the mesh is refined along the line $\theta = \theta_m$ and the solid-liquid interface ($\theta = 0$). This allows to accurately capture the structure and the extent of the two recirculating zones, features that are difficult to obtain with fixed meshes (see discrepancies described in Giangi et al. (2000); Kowalewski and Rebow (1999); Michalek and Kowalewski (2003)).

The time evolution of the solid-liquid interface is depicted in Fig. 5.13d for several time instants from $t = 0.05$ ($t_\varphi = 70[s]$) to final time $t = 1.61$ ($2340[s]$). We observe first a straight shape of the front from $t = 0$ to $t = 0.05$. Then, the top and bottom of the freezing front move at different rates from $t = 0.3$ due to the competing effects of positive and negative buoyancy forces in the liquid water. The upper clockwise circulation has indeed the task to transport the hot liquid to the top wall and back along the extremum of the density variation (localized at the temperature isoline $\theta = \theta_m$), and slows down consequently the growth of the solid layer. In the same time, the abnormal recirculation traps the cold liquid water at the bottom part of the cavity, enhancing thus the solidification rate at this region as one can note in Fig. 5.13d.

5.7 Concluding remarks

In this chapter, we demonstrated the capability of our numerical method to produce highly accurate solutions of difficult multiphysics problems on several geometrical configurations. The complexity of the problem comes from the non-linear time evolution of the solid-liquid interface that could be highly deformed by the strong convection flow in the fluid phase. Linear and non-linear expressions of the buoyancy force were investigated.

For a linear Boussinesq force f_B, melting of pure paraffin (n-octadecane) and metal (Gallium) were simulated in a rectangular cavity heated from the side. The choice of these materials is motivated by their physical properties relatively equal in both solid and liquid phases, and the existence of many numerical and experimental investigations in the literature. Differences between the time evolution of the heat transfer for high and low $\mathcal{P}r$ configurations were investigated. Comparisons with existing benchmarks showed for each case a very good agreement. The unsteadiness of the flow for the Gallium was observed in our simulations by showing multi-cellular structure of the liquid flow and the high oscillating time evolution of the Nusselt number. The performance of the sequential code was also proven by simulating complex geometrical configurations. The melting of a cylindrical PCM including inner heated pipes and the solidification of a liquid PCM inside a distorted cavity showed good agreement with existing numerical data.

The total CPU time and the typical number of triangles corresponding to each PCM cases are summarized in Tab. 5.5. Noticeable is the fact that less than 2 CPU hours are necessary for most of the simulations, even when a sequential algorithm is used. The interest and the power of mesh adaptivity was highlighted by the simulation of the melting of the Gallium, since only 4 CPU hours are necessary to perform this case, while 980 CPU hours were reported by Hannoun et al. (2003) using a fixed-grid algorithm.

Case		CPU time (s)	Number of triangles
N-octadecane	Bench #1	2876.39	2,900
	Bench #2	19231	4,198
	Bench #3	40522.7	7,000
Gallium		14621.2	4,820
Cylindrical PCM		2060.42	3,076
Highly distorted PCM		6657.58	2,769

Table 5.5: Summary of simulations for the melting PCM: number of triangles and CPU times.

A non-linear expression of f_B was considered for the solidification of pure water. Besides the high $\mathcal{R}a$ and $\mathcal{S}te$ considered in our simulations, the efficiency of the mesh adaptivity was demonstrated by its capability to track simultaneously the interface $\theta = \theta_f$ and the line $\theta = \theta_m$ separating the two recirculating liquid regions. Qualitative comparison with the experimental image exhibited good agreement. The vortical structures in the liquid water were accurately captured and the density inversion interface was precisely solved.

A more comprehensive description of the melting process will be presented in the next chapter. Numerical and analytical tools will be developped to analyse and compare the melting of PCM heated either from the side or from below.

6 Numerical comparison of basal and lateral melting of a phase change material

We performed extensive validations of our numerical method in Chapters 4 and 5. Very good agreements were obtained for all validation tests against well-known benchmark cases. The robustness of the algorithm was proven by simulating challenging configurations. We now use the code as an investigation tool to analyse the phase-change process during the melting stage. We consider a square cavity of height H filled with n-octadecane PCM and pay a closer attention to the temporal evolution of different physical parameters of the system. Two classes of convective melting systems are of interest in this chapter: **(i)** lateral melting (LM) or **(ii)** basal melting (BM). As far as **(i)** is concerned, the PCM is subject to heating from the left side of the cavity, whereas for BM case the PCM is heated from the bottom generating a top melting boundary. The comparison of both cases is interesting since the dynamics of the melting is known to be fundamentally different for each of the two cases. The investigated configuration, the shape of the interface and the streamlines in the liquid phase are illustrated in Fig. 6.1. LM case (top) exhibits a mono cellular pattern while Rayleigh-Bénard-like convection cells are observed in the BM case (bottom).

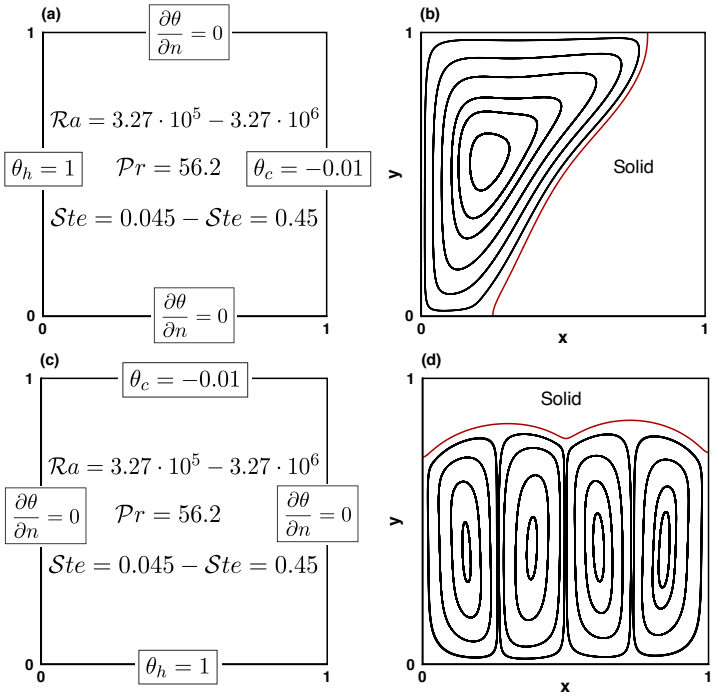

Figure 6.1: Comparison between lateral (LM) and basal melting (BM). Sketch of the computational domain and boundary conditions for LM (top) and BM (bottom) cases. Streamlines (panels b and d) and solid-liquid interfaces (solid red lines).

LM case could be representative for building applications, solar collectors or other thermal energy storage systems. In the frame of building applications, bricks made of PCM melt because of differences between outdoor and indoor temperatures and store the energy in the form of latent heat. Barreneche et al. (2016) showed that a wall made of PCMs reduces the temperature peak of about 20%. With regard to LM configurations, analytical investigation of Bejan (1989) and scaling analysis of Jany and Bejan (1988) permitted to describe the heat transfer during the melting by the mean of $\mathcal{N}u$-$\mathcal{R}a$ correlation. Their approach will be used in the present work. The BM case refers to passive temperature control for electronic devices or for a long list of geophysical problems, such as lava lakes, thermal convection in magma chambers, or ice-melt lakes. In contrast with LM case, notwithstanding linear and weakly non-linear instability analysis based on a vanishingly small Stefan number assumption (Vasil and Proctor, 2011), exact theoretical expressions of $\mathcal{N}u$ and L_f are not available during the convective regime because of the important non-linearities in the dynamics. Some comparisons with theory (Malkus, 1954; Grossmann and Lohse, 2000) made in the frame of Rayleigh-Bénard convection flow have been however carried out (Esfahani et al., 2018; Madruga and Curbelo, 2018; Favier et al., 2019). In this work, we develop a scale analysis for the so-called 'linear regime', which occurs between the onset of convective and oscillating flows.

In this chapter, we offer a comprehensive comparison between LM and BM configurations. We analyse first the time evolution of the LM process through a scale analysis in Sec. 6.1. Second, the BM case is studied in Sec. 6.2 with theoretical descriptions of the heat transfer involved during the melting. Finally, a comparison between the two cases is presented in Sec. 6.3 where we suggest some practical applications based on our analysis.

6.1 Lateral melting of n-octadecane PCM. Case LM.

We consider the physical properties of n-octadecane given in Tab. 5.1 and investigate different heights H of the cavity and different values of δT, to assess on the influence of the $\mathcal{R}a$ number. The numerical configuration is sketched in Fig. 6.1a. $\mathcal{R}a$ numbers ranging from $3.27{\cdot}10^5$ to $3.27{\cdot}10^6$ are investigated. We note that for the range of interest for $\mathcal{R}a$ and $\mathcal{S}te$ numbers, the assumption that $(\beta \times \delta T) \ll 0.01$ for the Boussinesq approximation is satisfied. A second dimensionless time τ related to the analytical correlation of Jany and Bejan (1988) is introduced:

$$\tau = \mathcal{S}te \times \mathcal{F}o = \mathcal{S}te \times \frac{\alpha t_\varphi}{H^2} = \frac{\mathcal{S}te}{\mathcal{P}r} \times t, \tag{6.1}$$

where $\mathcal{F}o$ is the Fourier number.

6.1.1 Analysis of the time evolution of the melting process

We start by describing the time evolution of the melting process for the lowest value of the Stefan and Rayleigh numbers, *i. e.* $\mathcal{S}te = 0.045$ and $\mathcal{R}a = 3.27 \cdot 10^5$. We are interested in a slow melting of the PCM to capture the transitions between the regimes described by Jany and Bejan (1988), mainly the onset of the convective regime.

At $\tau = 0$, the material is solid and the initial temperature is set to $\theta_0 = -0.01$ everywhere inside the cavity. Then, the temperature of the left wall is progressively increased to $\theta_h = 1$, while the right wall is maintained at the same cold temperature $\theta_c = -0.01$. The material starts to melt, with a melting front (identified by the iso-line $\theta = \theta_f = 0$) propagating from the left to the right side of the domain. Snapshots of the time evolution of the phase-change system are given in Fig. 6.2 for representative

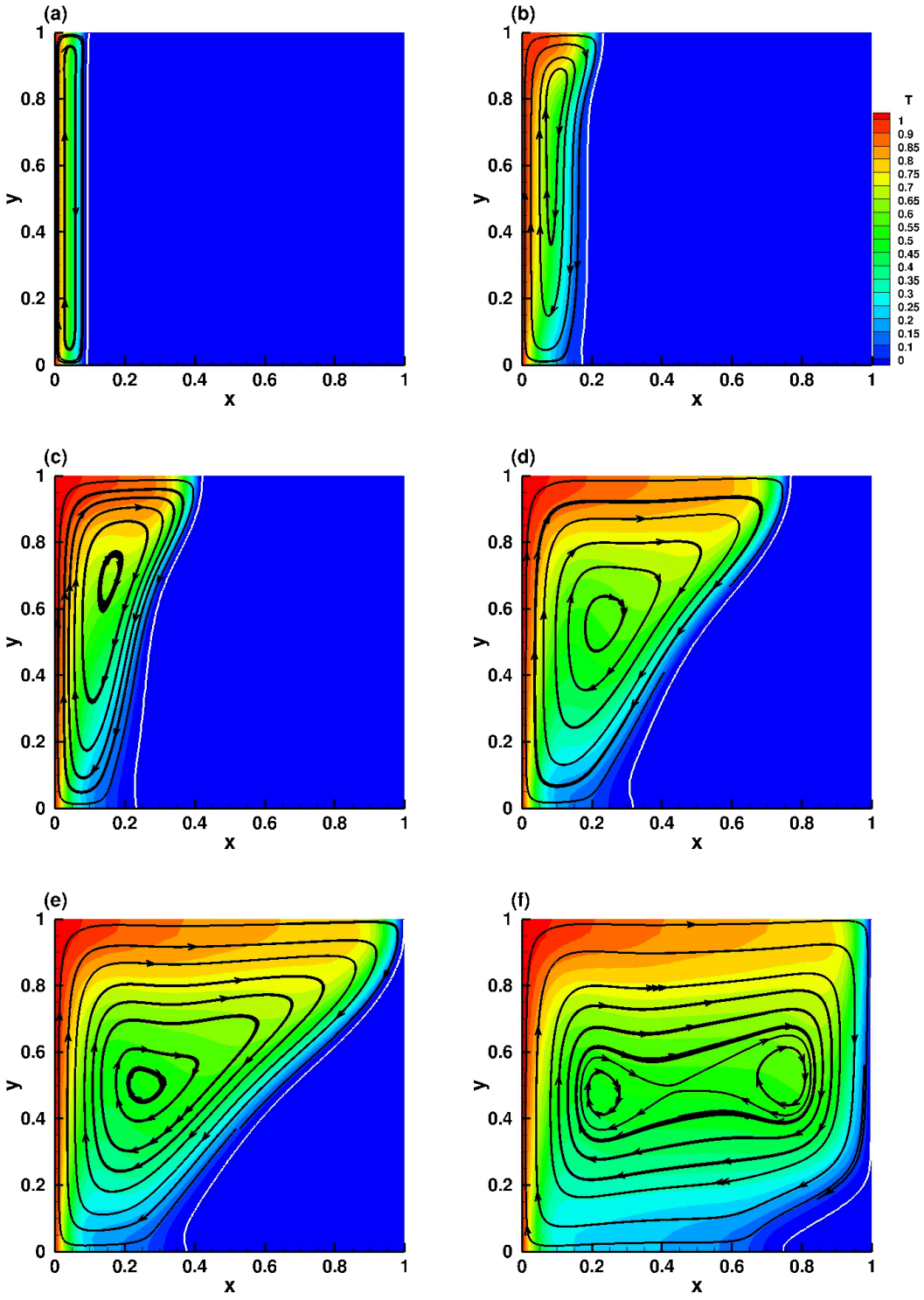

Figure 6.2: Temperature iso-lines, streamlines in the fluid phase, and phase-change interface. The solid part is represented in blue and corresponds to the region of temperature $\theta \leq \theta_f = 0$. Time instants (panels a to f): $\tau = 0.004; 0.016; 0.032; 0.063; 0.08; 0.2$. $\mathcal{R}a = 3.27 \cdot 10^5$, $\mathcal{P}r = 56.2$ and $\mathcal{S}te = 0.045$.

time instants. Panels (a) to (f) depict the flow streamline showing the clockwise recirculation of the fluid, the melting front, and the temperature distribution (the solid phase is denoted by the blue region). We can easily identify three different regimes describing the time evolution of the melting process.

- From $\tau = 0$ to $\tau = 0.004$ (Fig. 6.2a), we note the vertical shape of the melting front, well predicted by the classical conduction model of Stefan (1891). This indicates that, at this stage, heat transfer is dominated solely by conduction.
- Between $\tau = 0.016$ to $\tau = 0.032$ (Fig. 6.2b), the natural convection in the fluid phase starts to alter the shape of the melting front. A mixed conduction and convection regimes rule the heat transfer. Convective flow mainly affects the upper part of the fluid motion, while conduction is still dominating in the lower part. As the volume thermal expansion coefficient β is positive, we expect a clockwise circulation of the liquid inside the convection cell, as noted by Jany and Bejan (1988). This also makes the liquid-solid interface to move faster at the top of the cavity, explaining the deformed shape of the melting front, which is a signature of the convection effects (see also Kowalewski and Gobin (2004)).
- After $\tau = 0.032$ (Fig. 6.2c-d), natural convection dominates the heat transfer process and impacts radically the solid-liquid interface shape and motion. The melting front line exhibits four distinct regions characterized by different slopes with respect to the vertical axis. The largest slope is observed at the top of the cavity and is related to the particular shape of the convection cell. Note that top and bottom parts of the interface are normal to the cavity boundaries because of the imposed adiabatic boundary conditions.
- After $\tau = 0.08$ the melting front is nearly touching the right wall of the cavity, firstly at the top (Fig. 6.2e) of the cavity. The melting process continues and the fluid progressively fills the cavity, with a melting front deforming to a vertical line. The simulation of the melting process is stopped at $\tau = 0.2$ (Fig. 6.2f), when it is numerically difficult to separate the melting front from the right wall boundary. At this time instant, the fluid fraction reaches the value of 0.95 and the melting of the PCM is considered to be complete, even though a small region of solid PCM remains at the lower right bottom of the cavity. Note from Fig. 6.2f the existence in the fluid of two recirculating zones instead of a single one observed during previous stages.

6.1.2 Scale analysis of the melting

We further analyse each of the three regimes cited previously and identify the proper scales of the phenomenon. The (dimensionless) location of the interface will be denoted by Γ_i. Immediately after the melting starts (see Fig. 6.2a), the melted PCM occupies a thin enclosure of height H and width Γ_i. In this configuration, the temperature varies linearly between the two sidewalls and the heat transfer is essentially ruled by conduction. The fluid phase is almost motionless and the horizontal heat fluxes across the incipient melting PCM is balanced by the enthalpy absorbed at the interface. At the solid-liquid interface, the energy balance condition which takes into account the released latent heat and the discontinuity of heat fluxes between the solid and the liquid can be expressed by the following Stefan condition:

$$\begin{aligned} \theta(x = \Gamma_i) &= \theta_f = 0, \\ \frac{\partial \Gamma_i}{\partial t} &= -\frac{\mathcal{S}te}{\mathcal{P}r}\frac{\partial \theta}{\partial x}. \end{aligned} \tag{6.2}$$

Since the temperature field during the conduction regime is quasi-steady, Eq. (6.2) which is linear

could be approximated by

$$\frac{\partial \Gamma_i}{\partial t} \approx -\frac{\mathcal{S}te}{\mathcal{P}r}\frac{\theta_f - \theta_h}{\Gamma_i} \approx \frac{\mathcal{S}te}{\mathcal{P}r}\frac{1}{\Gamma_i}. \tag{6.3}$$

The location Γ_i of the interface is consequently given by

$$\Gamma_i = \sqrt{2 \times \frac{\mathcal{S}te}{\mathcal{P}r} t} = \sqrt{2\tau}. \tag{6.4}$$

Moreover, the Nusselt number can be evaluated using the same assumption:

$$\mathcal{N}u = \int_0^1 \left.\frac{\partial \theta}{\partial x}\right|_{x=0} dy = \frac{1}{\Gamma_i} = (2\tau)^{-1/2}. \tag{6.5}$$

To summarize, during the very first stage of the melting, when the heat transfer is led by conduction, the time evolution of the liquid fraction (depending on the location of the interface) and the Nusselt number could be approximated as:

$$L_f \sim (2\tau)^{1/2}, \tag{6.6}$$

$$\mathcal{N}u \sim (2\tau)^{-1/2}. \tag{6.7}$$

While the melting continues to expand to the right side of the domain, a natural convection flow emerges from the top of the cavity since we have a clockwise recirculation of the flow in the liquid phase (see Fig. 6.3). Turning back to the energy Eq. (2.14) in the liquid phase (*i. e.* $C = K = 1$), three distinct effects could be identified:

$$\underbrace{\frac{\delta\theta}{t}}_{Inertia}, \quad \underbrace{v\frac{\delta\theta}{H}}_{Convection}, \quad \underbrace{\frac{\delta\theta}{\Gamma_i^2}}_{Conduction}. \tag{6.8}$$

As t increases, the inertia decreases while the convection effect increases since it is proportional to v. The conduction becomes more and more negligible with the increasing value of Γ_i with time. Jany and Bejan (1988) described the convective heat transfer contributing during this regime by defining a Rayleigh number based on y^* as $\mathcal{R}a_{y^*} = \mathcal{R}a \times y^{*3}$, with y^* the height of the melted zone altered by the convection flow as shown in Fig. 6.3. At the bottom part of the cavity, the interface remains vertical by the effect of the conductive heat transfer. The total Nusselt number during the mixed conduction-convection regime could be therefore approximated by (Jany and Bejan, 1988):

$$\mathcal{N}u \sim (2\tau)^{-1/2} + (2\tau)^{3/2} \times \mathcal{R}a. \tag{6.9}$$

Equation (6.9) indicates that the contribution of the conduction $\left(\sim 1/\sqrt{2\tau}\right)$ decreases with the time while the convection contribution is increasing.

Finally, when the natural convection flow is fully developed and dominates the heat transfer along the vertical heated wall, using the correlation of Bejan (2013), the dimensionless thickness of thermal boundary layer is $\delta_\theta \sim \mathcal{R}a^{1/4}$ (see also Jany and Bejan (1988)) and therefore the Nusselt number scales as:

$$\mathcal{N}u \sim \mathcal{R}a^{1/4}. \tag{6.10}$$

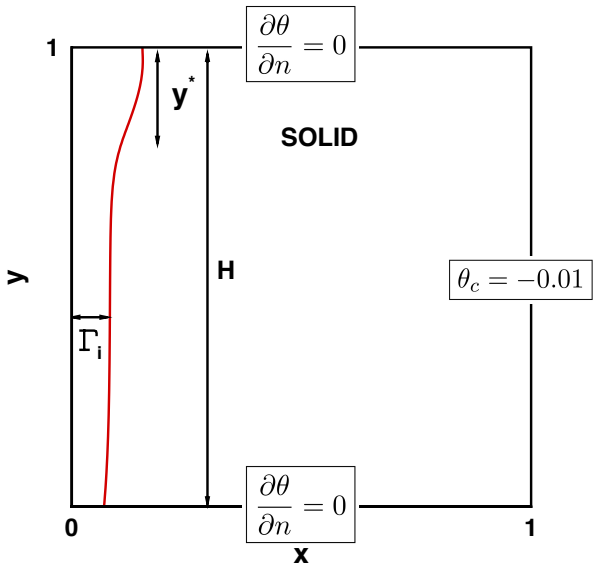

Figure 6.3: Illustration of the mixed regime by Jany and Bejan (1988). Solid red line is the solid-liquid interface, Γ_i represents the location of the interface and y^* denotes the height of fluid impacted by the emerging convective flow.

Jany and Bejan (1988) have proposed a more general single correlation, combining the regimes described previously:

$$\mathcal{N}u(\tau) = \frac{1}{\sqrt{2\tau}} + \left[c_1 \mathcal{R}a^{1/4} - \frac{1}{\sqrt{2\tau}}\right]\left[1 + \left(c_2 \mathcal{R}a^{3/4}\tau^{3/2}\right)^n\right]^{1/n}. \tag{6.11}$$

The values of the constants were fitted from numerical data: $c_1 = 0.27$, $c_2 = 0.0275$, and $n = -2$.

Okada (1984) has also suggested from his experimental data the following correlation for $\mathcal{N}u$:

$$\mathcal{N}u = \begin{cases} \dfrac{1}{\sqrt{2\tau}}, & \text{if} \quad \tau \leq \tau_t, \\ \dfrac{1}{\sqrt{2\tau_t}}\left\{1 + C(\tau - \tau_t)\right\}, & \text{if} \quad \tau > \tau_t, \\ c_1 \mathcal{R}a^{0.266}, & \text{otherwise}, \end{cases} \tag{6.12}$$

with the constant $c_1 = 0.234$ and the exponent 0.266 fitted from experimental data, and τ_t the transition time from conduction to convection as discussed previously.

Predictions of Eqs. (6.12) and (6.11) are compared with our numerical results in Fig. 6.4 showing the time evolution of the Nusselt number at the left wall. Our results perfectly fit with the theoretical prediction of Jany and Bejan (1988) and are also in good agreement with the experimental correlation of Okada (1984). The gap between the current simulation and the results of Okada (1984) could be explained by the experimental heat loss mentioned by the author and the uncertainties of the experimental measurements. The regimes described by the shape of the interface in Sec. 6.1.1 could be followed in the temporal evolution of $\mathcal{N}u$:

1. **The pure conduction regime** ($\mathcal{N}u \sim (2\tau)^{-1/2}$) for $\tau \gtrsim 0$ to $\tau \sim \mathcal{R}a^{-1/2} = 0.02$ (corresponding to Fig. 6.2a). Since the temperature gradient has initially huge values because of the increase of the temperature of the left wall, the Nusselt number rapidly decreases during the first

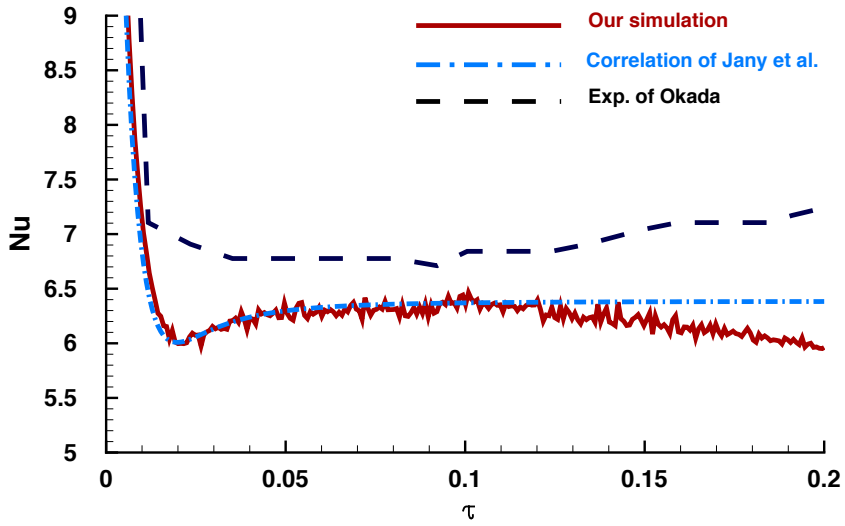

Figure 6.4: Complete melting of the PCM. Time evolution of the average Nusselt number defined at the hot (left) wall (cf. Eq. (2.24)) (solid line). Comparison with the experimental results of Okada (1984) (dashed line) and the predictions using the correlation in Eq. (6.11) suggested by Jany and Bejan (1988) (dash-dot line). $\mathcal{R}a = 3.27 \cdot 10^5$, $\mathcal{P}r = 56.2$ and $\mathcal{S}te = 0.045$.

stage of the flow evolution. The signature of this conduction regime is the slow heat transfer characterized by a monotonic decrease of the Nusselt number.

2. **The mixed conduction-convection regime** ($\mathcal{N}u \sim \tau^{-1/2} + \mathcal{R}a\,\tau^{3/2}$) for $0.02 \leq \tau \leq 0.05$ (illustrated in Fig. 6.2b).

3. **The convection dominated regime** ($\mathcal{N}u \sim \mathcal{R}a^{1/4}$) for $\tau > Ra^{-1/2}$ (corresponding to Figs. 6.2c-e). The plateau at the value of $\mathcal{R}a^{1/4}$ corresponds to the pure convective transfer and is observed in Fig. 6.4 for $0.05 \leq \tau \leq 0.1$. Numerical results show a slight decrease of $\mathcal{N}u$ in the final stage ($\tau \geq 0.1$), when the melting front starts to touch the right wall of the cavity (see Figs. 6.2e-f). The correlation model is not valid for this late evolution of the melting process.

Another important basic quantity describing the melting process is the liquid fraction L_f. The time evolution of the liquid fraction (Fig. 6.5a) displays three regimes during the melting process. L_f initially grows as $\tau^{1/2}$, which is a typical law for a conduction-dominated heat transfer. Then, a linear temporal evolution is observed, until the melting front reaches the right wall. This linear regime corresponds to the quasi-steady state observed in the evolution of the Nusselt number (Fig. 6.4).

Using the asymptotic limits of Eq. (6.11) for $\tau \to 0$ (pure conduction) and $\tau \to \infty$ (pure convection), Jany and Bejan (1988) suggested the following correlation law for the time evolution of the liquid fraction:

$$L_f(\tau) = \left[\left(\sqrt{2\tau}\right)^5 + \left(c_1 \mathcal{R}a^{1/4}\tau\right)^5\right]^{1/5}, \tag{6.13}$$

where $c_1 = 0.27$ is the same constant as in Eq. (6.11). We compare in Fig. 6.5b our numerical results with the predictions based on Eq. (6.13) within the validity domain of the analysis, *i. e.* before the melting front reaches the right wall of the cavity. A very good agreement is found with theoretical predictions and also with previously published numerical results (Wang et al., 2010a).

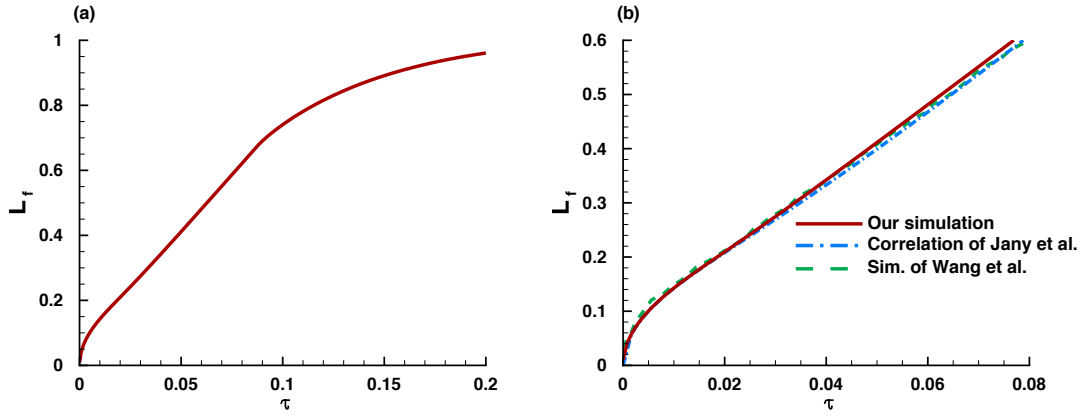

Figure 6.5: Complete melting of the PCM. (a) Time evolution of the liquid fraction for the complete melting of the PCM. (b) Comparison of our results (solid line) with the numerical results of Wang et al. (2010a) (dashed line) and the predictions using the correlation (6.13) suggested by Jany and Bejan (1988) (dash-dot line).

6.1.3 Influence of the Rayleigh number

To investigate the influence of the Rayleigh number on the evolution of the melting process, we performed different simulations by multiplying the initial value of $\mathcal{R}a = 3.27 \cdot 10^5$ by a factor of 5 and 10, respectively. The exact values are: $\mathcal{R}a = 1.62 \cdot 10^6$ and $\mathcal{R}a = 3.27 \cdot 10^6$. First, we increase the height H of the cavity by a factor of $\sqrt[3]{5}$ and $\sqrt[3]{10}$ and consider the same δT. Thus the $\mathcal{S}te$ number is kept constant. Second, we increase the temperature difference parameter δT by keeping H constant. It corresponds to an increased value of the Stefan number by a factor of 5 and 10: $\mathcal{S}te = 0.223$ and $\mathcal{S}te = 0.45$.

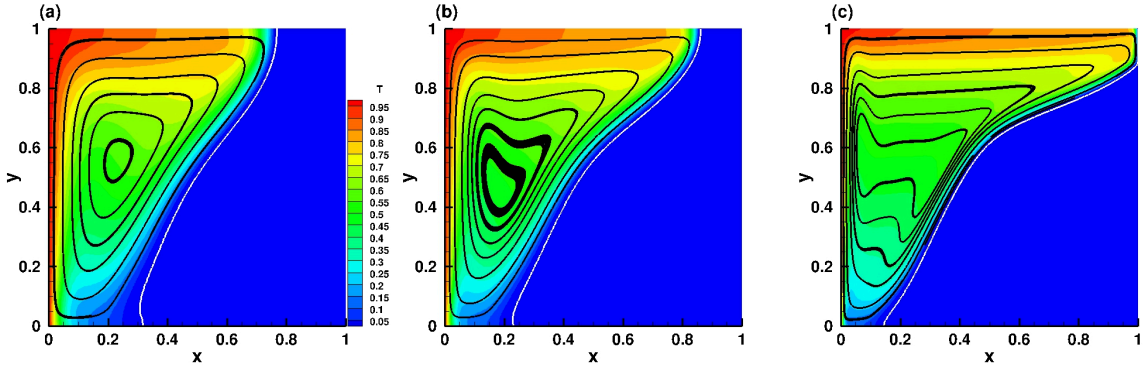

Figure 6.6: PCM melting at $L_f = 0.5$. Illustration of the temperature field, streamlines, and melting front for three $\mathcal{R}a$ numbers: (a) $\mathcal{R}a = 3.27 \cdot 10^5$, (b) $\mathcal{R}a = 1.62 \cdot 10^6$, and (c) $\mathcal{R}a = 3.27 \cdot 10^6$. The $\mathcal{P}r$ and $\mathcal{S}te$ numbers are kept constant: $\mathcal{P}r = 56.2$ and $\mathcal{S}te = 0.045$.

Snapshots of numerical solutions for $\mathcal{R}a = 3.27 \cdot 10^5$, $\mathcal{R}a = 1.62 \cdot 10^6$ and $\mathcal{R}a = 3.27 \cdot 10^6$ at constant $\mathcal{S}te$ number are shown in Fig. 6.6. The colours correspond to the temperature distribution, the black lines correspond to streamlines and the white lines correspond to the solid-liquid interface.

Panels (a) to (c) depict the dynamics of the convective melting flow when half of the initial solid PCM ($L_f = 0.5$) have melted. The top part of the interface moves faster while the bottom one is slowed by the increasing value of $\mathcal{R}a$. According to the Stefan interface condition in Eq. (6.2), at constant $\mathcal{S}te$ and $\mathcal{P}r$ numbers, the interface velocity is proportional to $\partial\theta/\partial n$, which is maximum at the top of the cavity because of the clockwise recirculation of the fluid. This explains the observed trends.

Figures 6.7 and 6.8 plot the temporal evolution of the liquid fraction L_f (panel a), and the average Nusselt number defined at the hot wall (panel b). The same heat transfer regimes described previously are observed for each case: conduction, mixed conduction-convection and convection. We note that results are plotted with respect to physical time t_φ instead of τ, because we compare solutions with different values of H. This infers with the definition of the non-dimensional times t and τ, making them not relevant to compare solutions.

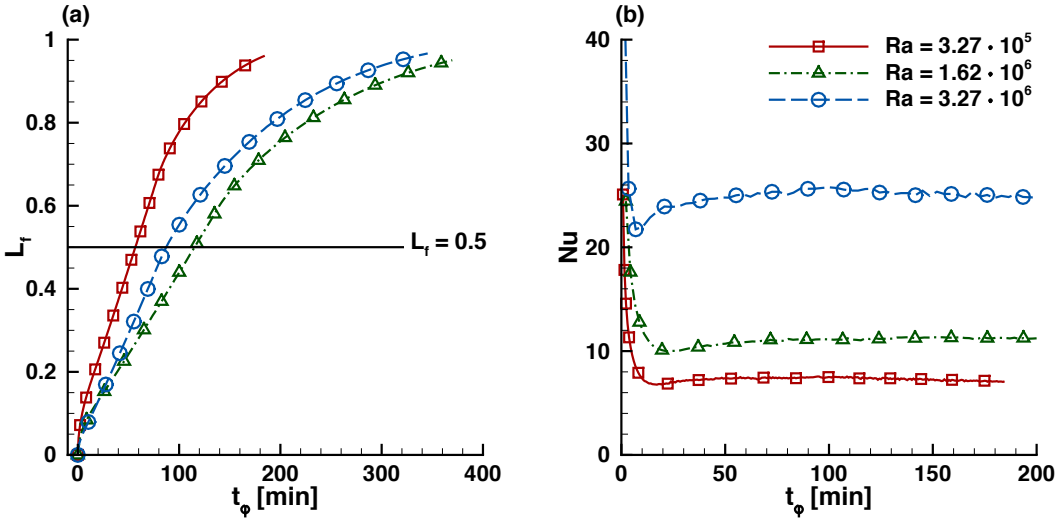

Figure 6.7: Complete melting of the PCM. Influence of the value of the Rayleigh number ($\mathcal{R}a$) on the time evolution of the liquid fraction (a) and the average Nusselt number defined at the hot (left) wall (b). The reference case ($\mathcal{R}a = 3.27 \cdot 10^5$) is represented by red continuous lines. The value of the $\mathcal{R}a$ was increased by a factor of 5 and 10, while the Stefan number $\mathcal{S}te$ is kept constant.

Figure 6.7a indicates that increasing the Rayleigh number by keeping δT constant induces a slower melting rate. This is the expected behaviour since the size of the PCM is increased by a factor of 2, and the velocity $\boldsymbol{u}$ is decreasing to satisfy the condition $\mathcal{R}e = 1$. We note however a non-monotonic variation of the time necessary to melt a fixed value of PCM. For instance, to achieve $L_f = 0.5$ (50% of the volume is melted), an increase of $\mathcal{R}a$ by a factor of 10 leads to a growth of the time by a factor of 1.7. Nonetheless, when $\mathcal{R}a$ is 5 times larger, the necessary time only increases by a factory of 2. This is most likely due to the non-linear intricacies of the problem and requires further investigation. Furthermore, the Nusselt number reported in Fig. 6.7b shows that the higher the Rayleigh number, the higher is the Nusselt number. This is consistent, since the temperature gradient is integrated along a longer heated wall.

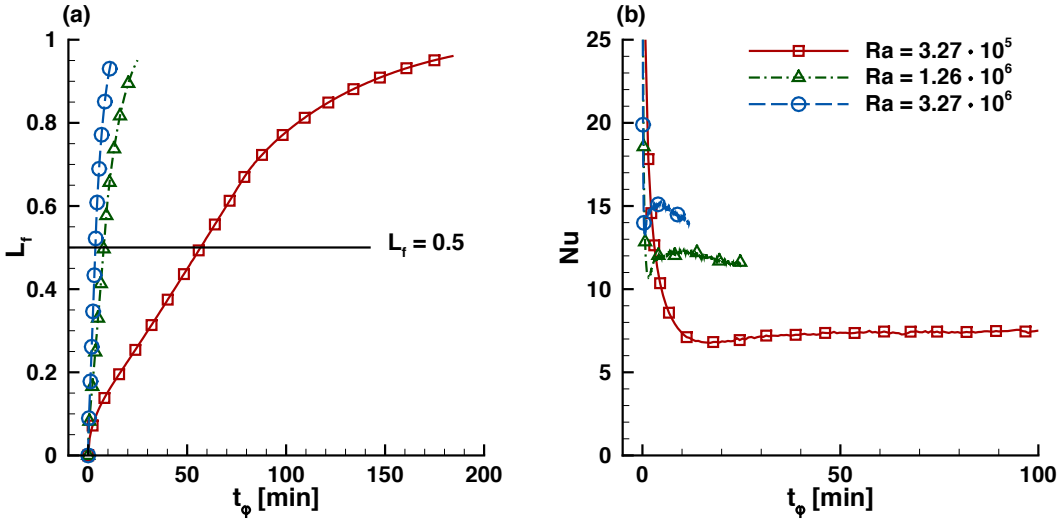

Figure 6.8: Complete melting of the PCM. Influence of the value of the Rayleigh number ($\mathcal{R}a$) on the time evolution of the liquid fraction (a) and the average Nusselt number defined at the hot (left) wall (b). The reference case ($\mathcal{R}a = 3.27 \cdot 10^5$) is represented by red continuous lines. The value of the $\mathcal{R}a$ and $\mathcal{S}te$ were increased by a factor of 5 and 10.

Figure 6.8a shows that by increasing the value of δT, and consequently increasing the Rayleigh number and the Stefan number, the PCM melts faster. We note that the height H of the cavity is kept constant, hence the natural convection flow in the melted PCM is enhanced when the Rayleigh number keep increasing. As a consequence, the convection-dominated regime is reached earlier, as shown in Fig. 6.8b by the shift of the minimum of the $\mathcal{N}u$ to lower values of t_φ. This evolution is also observed for the liquid fraction. As expected, an increase of the Rayleigh number and the Stefan number is followed by an enhancement of the heat transfer during the melting, and consequently an improved efficiency of the PCM.

6.2 Basal Melting of n-octadecane PCM. Case BM.

We now pay attention to the BM case. We investigate the melting of pure n-octadecane PCM in a square enclosure subject to heating from the bottom side. When compared to the lateral melting case, the dynamics of the melting is different for such configuration, in which natural convection develops Bénard cells. We recall that the physical parameters and the numerical configuration are reported in Fig. 6.1. We perform two-dimensional numerical simulations, although Gau et al. (1983) and Gong and Mujumdar (1998) noticed the existence of three-dimensional convection cells during the very first step of the melting process. These three-dimensional convection cells are usually neglected for relatively moderate $\mathcal{R}a$ numbers, particularly for $\mathcal{R}a \leq 10^8$. In this case, three-dimensional cells survive over a very short time compared to the whole melting process. Therefore the two-dimensional model is realistic. A qualitative description of the dynamics of the natural convection flow and its impact on the melting front is first addressed in Sec. 6.2.1. Then, a scale analysis is conducted to describe the heat transfer that occurs during the melting in Sec. 6.2.2. Finally, a comparison between the LM and BM cases is presented in Sec. 6.3.

6.2.1 Temporal evolution of the melting process

Figure 6.9 displays the structure of the natural convection flow after the primary instability through a sequence of panels for temperature isolines and streamlines in the liquid phase, for Rayleigh numbers ranging from $\mathcal{R}a = 3.27 \cdot 10^5$ to $\mathcal{R}a = 3.27 \cdot 10^6$. An array of lengthening plumes (panels a to c) and counter-rotating convective cells (panels d to f) are located in the liquid phase, in which the number of thermal plumes increases with the Rayleigh number. For $\mathcal{R}a = 3.27 \cdot 10^5$, one can observe three equidistant plumes in Fig. 6.9a and five convective cells in Fig. 6.9d, while four and six plumes are observed for $\mathcal{R}a = 1.635 \cdot 10^6$ in Fig. 6.9b and $\mathcal{R}a = 3.27 \cdot 10^6$ in Fig. 6.9c. These observations agree well with the numerical results of Gong and Mujumdar (1998) and Madruga and Curbelo (2018) who studied the correlation between the number of thermal plumes and the size of the domain. The shape of the interface is directly linked to the dynamics of these plumes. The mushroom form of the plumes results from the two symmetric counter-rotating convective cells surrounding each of them. We observe an anti-clockwise recirculation of the left convection cell and a clockwise recirculation of the right one. Thus, the liquid is heated to the highest temperature at the bottom and then floats up, reaches the phase change interface and splits into opposite directions. The liquid is cooled as it flows through the phase-change interface. It results a non-planar front with a peak at the center of each couple of counter-rotating convective cells.

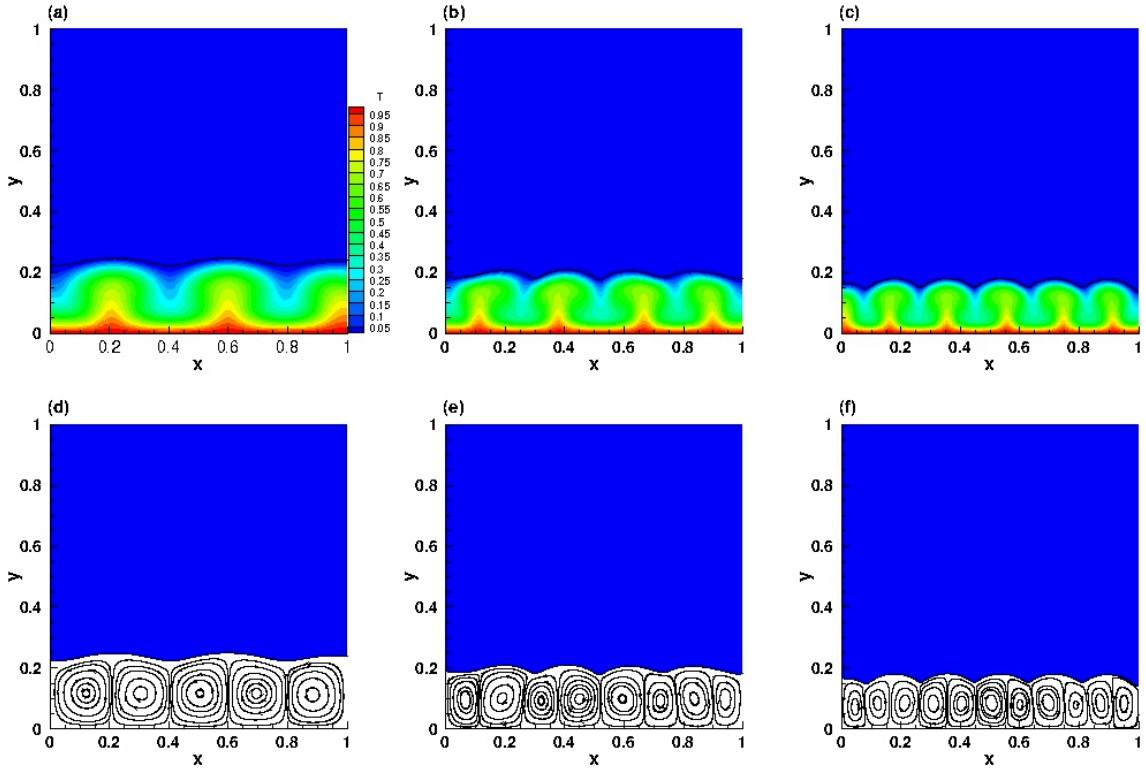

Figure 6.9: Melting of PCM heated from below. Temperature field and solid-liquid interface (top) and streamlines (bottom) in the liquid phase for different Rayleigh numbers (a) $\mathcal{R}a = 3.27{\cdot}10^5$ and $t = 30$, (b) $\mathcal{R}a = 1.635{\cdot}10^6$ and $t = 15$, (c) $\mathcal{R}a = 3.27{\cdot}10^6$ and $t = 10$.

To describe the temporal evolution of the melting, it is useful to introduce the effective Rayleigh and Nusselt numbers of the fluid layer, based on the height of the melted PCM:

$$\mathcal{R}a_e = \mathcal{R}a \times \bar{\delta}_H^3, \tag{6.14}$$
$$\mathcal{N}u_e = \mathcal{N}u \times \bar{\delta}_H, \tag{6.15}$$

with $\bar{\delta}_H$ the non-dimensional averaged fluid height. Note that $\bar{\delta}_H$ could be assimilated to the liquid fraction.

Figure 6.10 depicts in detail the temporal evolution of the melting for $\mathcal{R}a = 6.54 \cdot 10^6$, during which the effective Rayleigh number increases and influences the dynamics of the flow. The temperature field, the location of the interface, and the streamlines are reported in panels (a) to (l).

Before the first instability arises, the melted layer evolves solely by conduction. There is no noticeable fluid flow and the melting front remains straight (panel a). The temperature is distributed linearly in the vertical direction through the incipient liquid layer. The convective regime occurs at $\mathcal{R}a_e \approx 7 \times 10^3$ when the phase-change interface becomes non-planar (panel b). This is in good agreement with the observation of Esfahani et al. (2018); Favier et al. (2019). It is worth noting that, in the framework of the classical Rayleigh-Bénard convection flow, the first instability appears at critical Rayleigh number $\mathcal{R}a_c \approx 1707.76$, in the limit of vanishing $\mathcal{S}te$ number (Chandrasekhar, 2013). This critical value is however higher for large $\mathcal{S}te$ numbers (Vasil and Proctor, 2011). The onset of convection is marked by a change in the shape of the interface from straight to a nearly periodic curve.

As the fluid expands upwards, the effective Rayleigh number increases and we observe 10 convective rolls being stretched vertically (panels c to e). For $\mathcal{R}a_e \leq 2 \cdot 10^5$, one can note that the number of rolls is time-independent. Such behaviour could be compared to the steady convection regime after the onset of primary instability in the Rayleigh-Bénard system (see Chandrasekhar (2013)). This regime will be referred to linear regime in the present study.

After the rolls are elongated vertically, they start to oscillate laterally and then merge to create greater rolls, starting with $\mathcal{R}a_e = 2.9 \times 10^5$ (panel g). The interface loses periodicity and the structure of the rolls becomes disordered. At this stage, neither the mushroom form of the plumes nor the periodic distribution of the convection cells are no longer observed. The main consequence of this observation is that the melting front is modified. The interface is shaped by the new flow pattern.

6.2.2 Scale analysis

Let us now proceed on a scale analysis for the description of the heat transfer processes during melting. The dynamics of the BM case is usually classified in the literature into five regimes, defined following a power law of the $\mathcal{N}u - \mathcal{R}a$ (Esfahani et al., 2018; Madruga and Curbelo, 2018): a conductive regime, a linear regime, an oscillating regime, a turbulent regime, and finally an ultimate regime. The simulations performed in this chapter cover the first three regimes. During the conductive regime, the heat transfer is fully dominated by conduction. The time evolution of the liquid fraction and the Nusselt number could be approximated by the same scaling obtained in Eq. (6.6). Notwithstanding, after the onset of the convection, the quasi-steady evolution of the heat transfer observed in the LM case (see Fig. 6.4), is no longer observed in the BM case because of non-linear instabilities.

When the convective heat transfer is fully developed in the melted PCM, two distinct heat transfer processes could be identified: a bulk heat transfer for low effective Rayleigh number regime, mainly for $\mathcal{R}a_e \leq 10^5$, followed by a boundary layer heat transfer regime, which is predominant when the flow becomes oscillatory or turbulent. We develop in this section a scale analysis for the linear regime, during

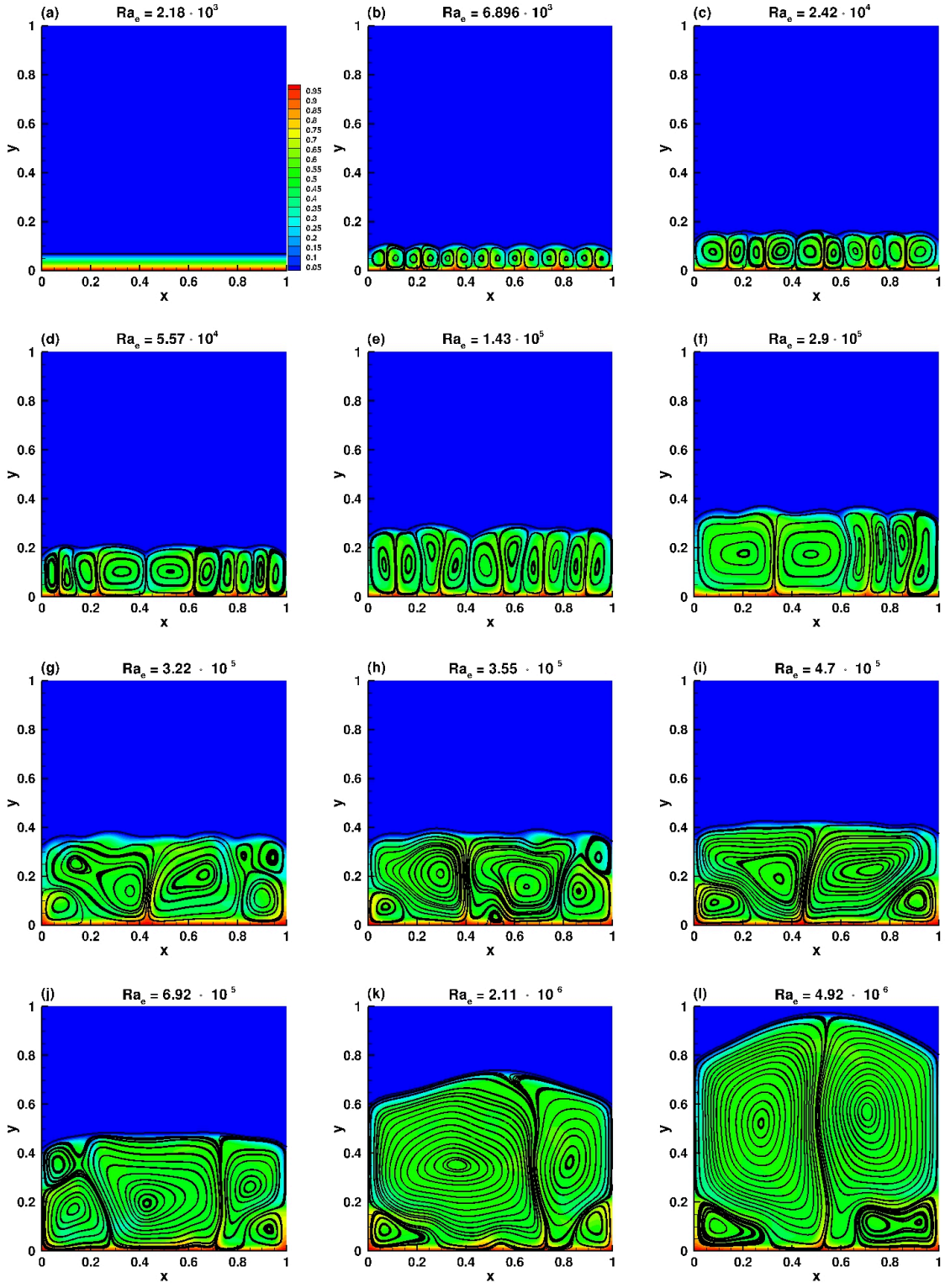

Figure 6.10: Time evolution of the melting of a PCM heated from below at $\mathcal{R}a = 6.54 \cdot 10^6$: temperature field, solid-liquid interface and streamlines. For each time instant, the effective Rayleigh number is indicated.

which bulk heat transfer occurs, to approximate the amount of heat transfer. Beyond this regime, due to the important non-linearities of the dynamics, we rely on theories developed for turbulent Rayleigh-Bénard convection flows (Malkus, 1954; Grossmann and Lohse, 2000).

During the linear regime, the convective cells are elongated vertically and the number of rolls is time-independent. In our scale analysis we focus on a single roll convection pattern to assess the amount of heat transfer through it. A schematic overview of the phenomenon is drawn in Fig. 6.11.

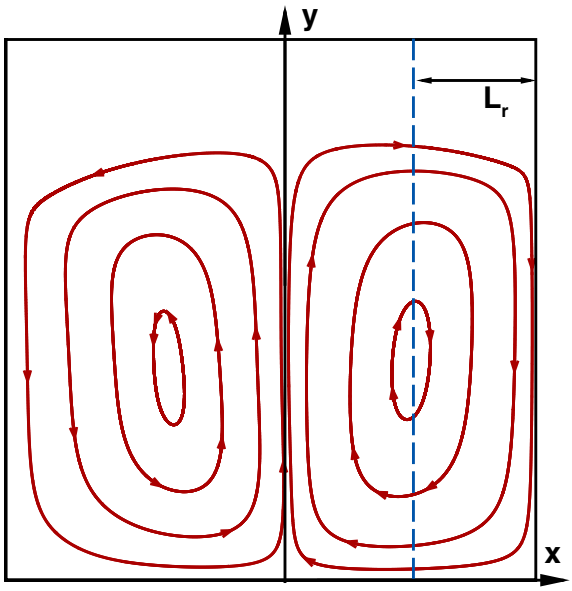

Figure 6.11: Natural convection flow emerging from melting heated from below.

Let us define L_r, the (dimensionless) half-thickness of a cell. An appropriate scaling during this regime is hence

$$x \sim L_r, \quad y \sim \bar{\delta}_H, \tag{6.16}$$

with $L_r < \bar{\delta}_H$. We consider the dimensionless Navier-Stokes-Boussinesq system (2.12) - (2.14) applied to a single cell ($C = K = 1$, and $S(\theta) = A(\theta) = 0$), which could be rewritten as follows (with scaling (4.6), *i. e.* $\mathcal{R}e = 1$):

$$\frac{\partial u}{\partial x} + \frac{\partial v}{\partial y} = 0, \tag{6.17}$$

$$\frac{\partial u}{\partial t} + u\frac{\partial u}{\partial x} + v\frac{\partial u}{\partial y} = -\frac{\partial p}{\partial x} + \left(\frac{\partial^2 u}{\partial x^2} + \frac{\partial^2 u}{\partial y^2}\right), \tag{6.18}$$

$$\frac{\partial v}{\partial t} + u\frac{\partial v}{\partial x} + v\frac{\partial v}{\partial y} = -\frac{\partial p}{\partial y} + \left(\frac{\partial^2 v}{\partial x^2} + \frac{\partial^2 v}{\partial y^2}\right) + \frac{\mathcal{R}a}{\mathcal{P}r}\theta, \tag{6.19}$$

$$\frac{\partial \theta}{\partial t} + u\frac{\partial \theta}{\partial x} + v\frac{\partial \theta}{\partial y} = \frac{1}{\mathcal{P}r}\left(\frac{\partial^2 \theta}{\partial x^2} + \frac{\partial^2 \theta}{\partial y^2}\right). \tag{6.20}$$

The pressure p is first eliminated by deriving Eq. (6.18) with respect to y and deriving Eq. (6.19) with respect to x. One may refer to the book Bejan (2013) for more details, in the frame of the Rayleigh-Bénard convection flow. Substracting one from the other, we get

$$\frac{\partial}{\partial y}\left(\frac{\partial u}{\partial t}+u\frac{\partial u}{\partial x}+v\frac{\partial u}{\partial y}\right)-\frac{\partial}{\partial x}\left(\frac{\partial v}{\partial t}+u\frac{\partial v}{\partial x}+v\frac{\partial v}{\partial y}\right) \\ =\left[\frac{\partial}{\partial y}\left(\frac{\partial^2 u}{\partial x^2}+\frac{\partial^2 u}{\partial y^2}\right)-\frac{\partial}{\partial x}\left(\frac{\partial^2 v}{\partial x^2}+\frac{\partial^2 v}{\partial y^2}\right)\right]-\frac{\mathcal{R}a}{\mathcal{P}r}\frac{\partial\theta}{\partial x}. \tag{6.21}$$

Since we have $L_r \ll \bar{\delta}_H$ (consequently $\partial^2 v/\partial y^2 \ll \partial^2 v/\partial x^2$), three terms are dominant in Eq. (6.21):

$$\sim \underbrace{\frac{\partial^2 v}{\partial x \partial t}}_{inertia}; \quad \sim \underbrace{\frac{\partial^3 v}{\partial x^3}}_{friction}; \quad \sim \underbrace{\frac{\mathcal{R}a}{\mathcal{P}r}\frac{\partial\theta}{\partial x}}_{buoyancy}. \tag{6.22}$$

In terms of characteristic scales, this reduced momentum balance reads

$$\sim \underbrace{\frac{v}{L_r t}}_{inertia}; \quad \sim \underbrace{\frac{v}{L_r^3}}_{friction}; \quad \sim \underbrace{\frac{\mathcal{R}a}{\mathcal{P}r}\frac{\delta\theta}{L_r}}_{buoyancy}. \tag{6.23}$$

Equation (6.23) could be hence simplified by normalising Eq. (6.23) with respect to the friction scale, leading to

$$\underbrace{\frac{1}{\mathcal{P}r}}_{inertia}; \quad \underbrace{1}_{friction}; \quad \underbrace{\frac{\mathcal{R}aL_r^2}{v\mathcal{P}r}}_{buoyancy}. \tag{6.24}$$

For high-Prandtl fluids, the momentum balance is between buoyancy and friction (see *e. g.* Bejan (2013); Le Quéré and Gobin (1999)) and we obtain

$$v \sim \frac{\mathcal{R}aL_r^2}{\mathcal{P}r}. \tag{6.25}$$

Next, we turn attention back to the energy Eq. (6.20). During the pure conductive regime, the velocity is very small and negligible. The characteristic scale is therefore:

$$\frac{\delta\theta}{t} \sim \frac{\delta\theta}{\mathcal{P}rL_r^2}, \tag{6.26}$$

leading to

$$L_r \sim \left(\frac{t}{\mathcal{P}r}\right)^{1/2}. \tag{6.27}$$

At this earlier stage, the thermal layer thickness is of the same order as L_r, *i. e.* $\delta_\theta \sim L_r$. When the convection arises, we can identify three distinct effects

$$\underbrace{\frac{1}{t}}_{Inertia}; \quad \underbrace{\frac{v}{\bar{\delta}_H}}_{Convection}; \quad \underbrace{\frac{1}{L_r^2\mathcal{P}r}}_{Conduction}. \tag{6.28}$$

When the melting evolves (*i. e.* time increases), the inertia decreases in importance. There comes an effective time t_e when the energy equation expresses a balance between the convection and the conduction heat transfer (see Bejan (2013)):

$$\frac{v}{\bar{\delta}_H} \sim \frac{1}{\delta_\theta^2 \mathcal{P}r}. \tag{6.29}$$

Equations (6.29) and (6.25) lead to

$$\frac{\bar{\delta}_H}{\delta_\theta^2 \mathcal{P}r} \sim \frac{\mathcal{R}a \delta_\theta^2}{\mathcal{P}r}. \tag{6.30}$$

Since $\delta_\theta^2 \sim t/\mathcal{P}r$, we obtain

$$t_e \sim \left(\frac{\bar{\delta}_H}{\mathcal{R}a_e}\right)^{1/2} \times \mathcal{P}r. \tag{6.31}$$

At this effective time t_e, during which the inertia becomes negligible and the convection effects increase, the thermal layer thickness is

$$\delta_\theta \sim \left(\frac{t_e}{\mathcal{P}r}\right)^{1/2} \sim \left(\frac{\bar{\delta}_H}{\mathcal{R}a_e}\right)^{1/4} \sim \left(\bar{\delta}_H\right)^{-1/2} \mathcal{R}a^{-1/4}. \tag{6.32}$$

Accordingly, before the flow oscillates, the scaling for $\mathcal{N}u$ could be written as:

$$\mathcal{N}u \sim \bar{\delta}_H^{1/2} \times \mathcal{R}a^{1/4}. \tag{6.33}$$

Equation (6.33) highlights that the heat transfer through a single convection cell depends on the height of the melted PCM layer during the linear regime. Correlations pertaining to basal melting case in the literature do not distinguish between this contribution of the bulk and the boundary layer heat transfers after the onset of convection and relies directly on empirical correlations for turbulent Rayleigh-Bénard flows. It should be noted that Eq. (6.33) rely on only one cell of the system.

$\mathcal{R}a$	linear regime	oscillating regime
$3.27 \cdot 10^5$	0.286299	-
$1.635 \cdot 10^6$	0.274789	0.269158
$3.27 \cdot 10^6$	0.279616	0.283658
$6.54 \cdot 10^6$	0.274043	0.294528

Table 6.1: Exponent of the power laws of the linear and the oscillating regimes.

The exponents of the power laws obtained by our numerical simulations for four Rayleigh numbers are given in Tab. 6.1 during the linear and the oscillating regime. An exponent of 0.28 is observed for the linear regime and decreases with increasing Rayleigh number, which overestimates slightly the predicted scaling exponent of $1/4$. This is mostly due to the number of convection cells in the melted PCM and the effect of the non-planar solid-liquid interface, not taken into account in our analysis. However, our numerical results match better with the Grossmann-Lohse theory (Grossmann and Lohse,

2000), which predicts a scaling exponent of $2/7$, within the framework of natural convection flow. Furthermore, during the oscillating regime the exponent increases with the Rayleigh number and tends to the empirical value of $1/3$.

Concerning the temporal evolution of the liquid fraction L_f, one can introduce the following scaling, from Favier et al. (2019), obtained by a balance between the total rate of change of the enthalpy in the system and the heat fluxes entering and leaving the domain:

$$L_f(t) = \left[\sqrt{2t}^{(2-3\beta)} + c\mathcal{R}a^{\beta}t\right]^{1/(2-3\beta)}, \tag{6.34}$$

with β the exponent in the $\mathcal{N}u - \mathcal{R}a$ power law, $c = \frac{(2-3\beta)\gamma}{2+\mathcal{S}te}$ and γ a constant fitted from numerical data. For the conductive regime, by taking $\gamma = \beta = 0$, the well-known behavior $L_f \sim t^{1/2}$ is obtained. Replacing β by the exponent value $1/4$ for the convective regime, we obtain $L_f \sim t^{4/5}$.

The time evolution of the liquid fraction is illustrated in Fig. 6.12a. As expected, the purely diffusive stage displays the scaling $L_f \sim t^{1/2}$. Our simulations exhibit a power-law evolution of $L_f \sim t^{0.82}$ when the convection is fully developed in the fluid, in good agreement with $L_f \sim t^{4/5}$.

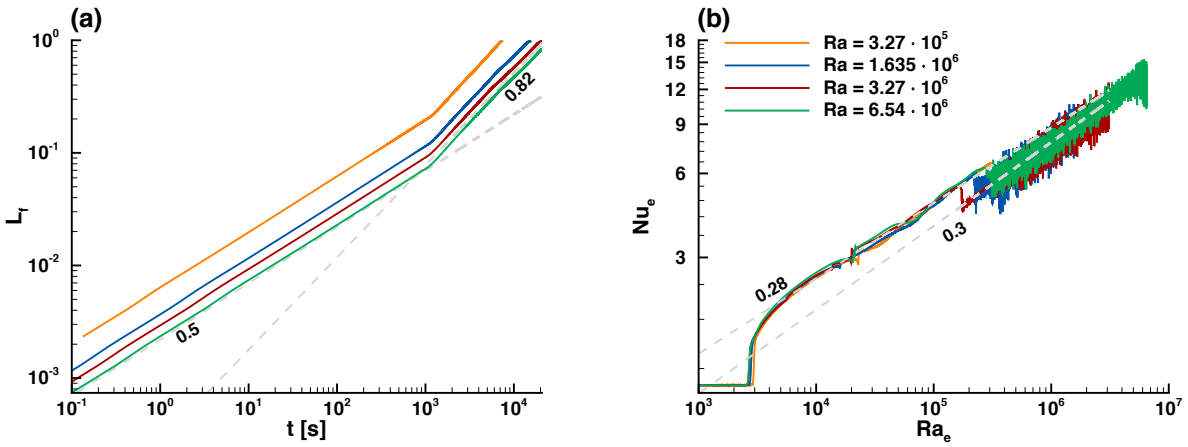

Figure 6.12: BM case for three Rayleigh numbers: $\mathcal{R}a = 3.27 \cdot 10^5$, $1.62 \cdot 10^6$, and $3.27 \cdot 10^6$. Time evolution of the liquid fraction (a) and Nusselt number (b).

Figure 6.12b shows the temporal evolution of the heat flux, represented by the Nusselt number, and the strength of buoyancy, represented by the Rayleigh number, when the melting evolves. The onset of the convection arises around $\mathcal{R}a_e = 2 \times 10^3$, when a sudden jump in the evolution of $\mathcal{N}u_e$ is observed. Vasil and Proctor (2011) have investigated a weakly non-linear stability analysis and have highlighted a super-exponentional amplitude growth when the Rayleigh number becomes close to the traditional critical value in the limit of vanishing Stefan number. This super-exponential growth is moreover followed by a rapid pattern readjustment. The trend of $\mathcal{N}u_e$ at the onset of convection is in total agreement with the prediction of Vasil and Proctor (2011). The results of Esfahani et al. (2018); Madruga and Curbelo (2018); Favier et al. (2019) exhibit the same trend despite the different boundary conditions (periodic lateral boundary conditions, adiabatic boundary conditions at the top of the cavity, and a low value of $\mathcal{P}r$ for Esfahani et al. (2018) and Favier et al. (2019)). The rapid growth of $\mathcal{N}u_e$ is followed by a power law with averaged exponent $\mathcal{N}u \sim \mathcal{R}a^{0.28}$, for $10^3 \leq \mathcal{R}a \leq 10^5$. Finally, the transition from steady pattern of the convective rolls to oscillating pattern, followed by cell merging, as it is clearly shown in Fig. 6.10(d-f), is also illustrated by a decrease of $\mathcal{N}u$ at $\mathcal{R}a \sim 10^5$, followed

by high oscillations in the temporal evolution of the heat transfer. The power-law relation $\mathcal{N}u - \mathcal{R}a$ is bounded in this stage by the average exponent of $2/7$.

6.3 Comparison between LM and BM cases

A comparison of the liquid fraction L_f, the Nusselt number $\mathcal{N}u$, and the accumulated heat input Q_0 is offered in Fig. 6.13. Blue lines denote the LM case and red lines the BM case. Different values of the $\mathcal{R}a$ number, ranging from $\mathcal{R}a = 3.27 \cdot 10^5$ to $\mathcal{R}a = 6.54 \cdot 10^6$ are investigated.

The temporal evolution of L_f (left panels) displays a similar trend of both curves up to $L_f = 0.6$ for all cases. For instance, for $\mathcal{R}a = 3.27 \cdot 10^5$ (panel a), LM and BM cases evolve at the same rate from $t = 0$ to $t = 100$, corresponding to 60% of melted PCM. Then, for greater Rayleigh numbers, the gap keeps increasing, albeit slightly. This result agrees with the scaling analysis that predicts the same trend of both systems as long as the number of convective cells is close to one. Since the number of rolls is increasing with the Rayleigh number, an enhancement of the melting rate is thus consistent. Furthermore, differences are noticeable for $L_f \geq 0.6$, when the interface of the LM case reaches the right (cold) interface. Increasing the Rayleigh number induces a faster advancement of the top of the LM front, which touches the cold wall earlier, slowing hence the evolution of the melting. One can observe during this period a decrease of the slope of the blue curve with respect to the vertical axis. Linear evolution of L_f is however noticed throughout the basal melting time since the interface touches the top cold wall very late.

Regarding the time evolution of the heat transfer (middle panels), red and blue curves match perfectly well during the conductive regime (see for *e. g.* Fig. 6.13 from $t = 0$ to $t = 18$ for $\mathcal{R}a = 3.27 \cdot 10^5$). This was expected since the contribution of the convective heat transfer is still negligible at this stage. Differences occur from the emergence of the natural convection flow. The evolution of $\mathcal{N}u$ is relatively smooth for the LM case, while the BM case exhibits a sudden increase due to the hydrodynamical instabilities. Significant gap between both curves arises during the oscillating regime: $\mathcal{N}u$ displays a highly oscillating value for the BM case when the liquid layer expands upward, while the LM case reaches an asymptotic value. Note that for higher and higher Rayleigh numbers, the Nusselt number increases accordingly.

The evolution of the accumulated heat input Q_0 is consistent with the foregoing remarks. Q_0 is defined as follows:

$$Q_0(t) = \int_0^t Nu(\tau)\, d\tau, \tag{6.35}$$

The decrease of the heat transfer monitored by the cell merging process in the BM case leads to a lower accumulated heat input. It follows that a more important thermal energy is stored when compared with the LM case.

These observations are of particular importance for PCM design for a specific application. If a fast melting is sought, the BM case is advised. It could be the case for example during quick temperature peak in electronic components. Conversely, when the PCM is expected to melt in a longer period, the LM case is more appropriate.

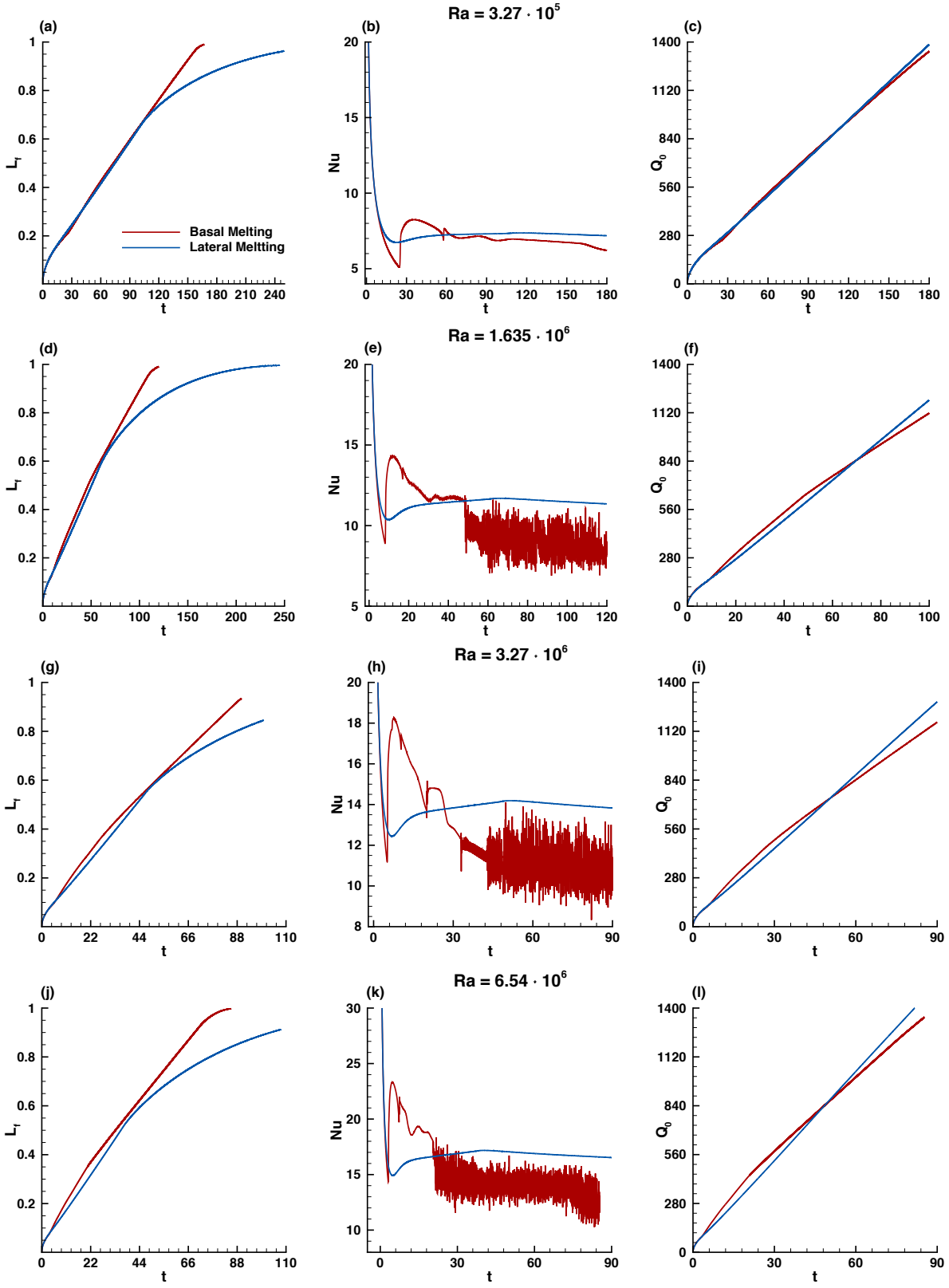

Figure 6.13: Comparison between LM and BM cases. Rayleigh numbers ranging from $\mathcal{R}a = 3.27 \cdot 10^5$ to $\mathcal{R}a = 6.54 \cdot 10^6$. Liquid fraction(left), Nusselt number (middle), and accumulated heat input (right).

6.4 Concluding remarks

The high accuracy of our numerical method permitted to simulate in this chapter lateral and basal melting cases. Numerical and theoretical comparisons of both cases were performed and have exhibited many differences, mainly on the dynamics of the flow and the heat transfer processes. A main question related to convective melting processes is to predict the temporal evolution of the melting rate, which is correlated to the heat-flux dynamics determined by the flow in the system. Since the dynamics of the flow is completely different for LM and BM systems, we have performed simulations for both cases and compared the evolution of some physical parameters.

We have investigated first the LM case, by simulating the melting of n-octadecane inside a square enclosure heated from the vertical wall. Three principal regimes were identified to describe the dynamics of the melting: conductive regime, mixed regime, and convective regime. The influence of the Rayleigh and the Stefan parameters on the flow was also assessed and indicated clearly that increasing $\mathcal{R}a$, by increasing either H or δT, enhances the heat transfer. Since stronger convection flow occurs in the liquid region with increasing Rayleigh number, the shape of the phase-change front is altered consequently. The top of the interface moves faster while the bottom part is rather slowed down, resulting in a curved shape of the melting front.

Concerning the simulations of the BM case, simulations for a large range of Rayleigh numbers, $\mathcal{R}a = 3.27 \cdot 10^5$ to $\mathcal{R}a = 6.54 \cdot 10^6$, were carried out for a comprehensive description of the dynamics of the melting. Effective Rayleigh and Nusselt numbers, depending on the fluid height were introduced to describe the flow. The melted fluid layer was shown to be thermally unstable. It quickly develops convective motion of progressively higher intensity as the depth of the melted layer increases. The onset of these instabilities were observable either on the dynamics of the melting flow or the temporal evolution of the Nusselt number. The novelty is the theoretical description of the convective heat transfer during the linear regime, *i. e.* $\mathcal{R}a_e \leq 10^5$, through a scale analysis by separating the contribution of the bulk and the boundary layer heat transfers. For higher $\mathcal{R}a_e$ numbers, we used the knowledge acquired on turbulent natural convection system to understand convective melting.

We have finally compared the time evolution of the liquid fraction L_f, the heat transfer rate represented by the $\mathcal{N}u$ number, and the accumulated heat input Q_0. We showed that PCM melts faster when heated from below compared to the lateral melting, since the last case reaches the cold wall earlier, slowing accordingly the melting rate. However, the lateral oscillation of the convective cells in the BM case, yielding to cell merging processes, reduces the heat transfer rate. In the following chapter, we investigate the full melting-solidification cycle for a better understanding of the complete PCM cycle.

7 Numerical simulation of complete melting-solidification cycle of a phase-change material

This chapter presents an accurate numerical description of the alternate melting and solidification of a PCM. Square and cylindrical PCMs, that were simulated in Chapters 5 and 6 are considered in this chapter to investigate the solidification process. The fundamental operational mode of latent thermal energy storage (LTES) systems based on phase-change materials (PCM) is made of alternate melting and solidification cycles that are not necessarily periodic.

The natural convection occurring in the melting PCM is driven by the temperature difference $\delta T = T_h - T_f$. The dimensionless number that depicts the ratio between the forces creating and those refraining the motion is the Rayleigh number, which appears in the dimensionless form of the Navier-Stokes equations with Boussinesq approximation (Sec. 2, Eq. (2.16)). The higher is its value, the more intense is the heat transfer. Conversely, during the solidification, the phase-change is handled by the discharged temperature $T_{co} < T_f$, where the subscript 'co' stands for 'cooling'. For the square geometry discussed first in Sec. 7.1, this represents the temperature of the left wall, and for the cylindrical geometry presented in Sec. 7.2, it consists of the inner tube temperature. Thus, the relevant temperature difference in the solid phase of the PCM is $\delta T_{co} = T_f - T_{co}$ and the dimensionless temperature in the solid phase should be defined with respect to this δT_{co}. It is then obvious, from Eqs. (2.15) and (2.16), that the Rayleigh number should be defined using the same temperature difference. However, because the Rayleigh number amounts for the motion created by the hot temperature difference, we choose to keep the same definition for the Rayleigh number as for the melting case. This is still relevant for the melted core of the flow, where the persisting motion acts as a boundary condition for the solidification process. Under these conditions, in regard with the solidification process, we introduce a new parameter, $r_\delta = \delta T_{co}/(T_h - T_f)$, the normalised temperature with respect to $T_f - T_{co}$ and the relevant Rayleigh number will be then $\mathcal{R}a_{co} = r_\delta \times \mathcal{R}a$, where $\mathcal{R}a_{co}$ is the pseudo-Rayleigh number for solidification with a melted boundary. In the following, we will describe the process of solidification using three different values of r_δ. A new scaling is moreover introduced:

$$V_{ref} = \frac{\alpha_l}{H} \Rightarrow t = t_\varphi \frac{\nu_l}{H^2\,\mathcal{P}r} \Rightarrow \mathcal{R}e = \frac{1}{\mathcal{P}r}. \tag{7.1}$$

The solidification stage is indeed a slower process compared to the melting, therefore the use of an adapted scaling is more relevant. This leads to a different time scaling for each part of the cycle.

In Sec. 7.1, we perform two operating cases for the solidification process of melted PCM in a differentially heated square cavity. In the first study case the solidification starts after a complete melting of the PCM (liquid fraction of 95%), while in the second case after a partial melting (liquid fraction of 50%). Several practical implications for the two operating modes are drawn. In Sec. 7.2, we investigate the solidification of a cylindrical PCM with an inner obstacle. We provide temporal evolution of solid-liquid interface, liquid fraction, Nusselt number and accumulated heat input.

7.1 Melting-solidification cycle of a phase-change material with complete or partial melting in a square cavity

The sketch of the computational domain and boundary conditions are illustrated in Fig. 7.1a, corresponding to the melting of octadecane PCM presented in Sec. 5.2 of Chapter 6. Starting from a melted PCM (Fig. 7.1b), the simulation of the solidification process starts by imposing at the left-wall a constant (cold) temperature θ_{co} as it is shown in Fig. 7.1c. We consider two cases:

– case CM: solidification after a Complete Melting of the material ($L_f = 0.95$, Fig. 6.2f) and
– case PM: solidification after a Partial Melting ($L_f = 0.5$, Fig. 6.2d).

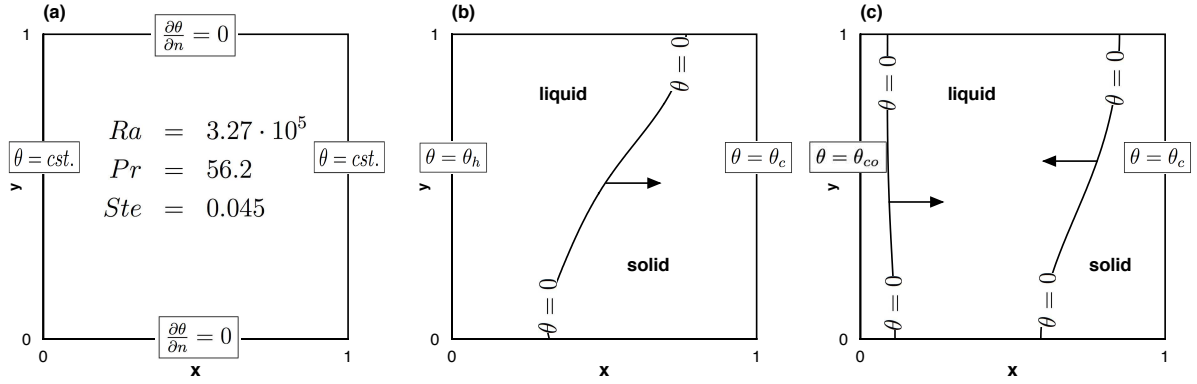

Figure 7.1: Sketch of the computational domain and boundary conditions. General configuration (panel a) with isothermal ($\theta = cst.$) vertical ($x = 0$ and $x = 1$) walls and adiabatic ($\partial\theta/\partial n = 0$) top and bottom walls. Configuration for the melting phase (panel b) with a hot left wall ($\theta = \theta_h > 0$) and a cold right wall ($\theta = \theta_c < 0$), followed by a solidification phase (panel c), when the temperature of the left wall is cooled to $\theta = \theta_{co} < 0$.

The solid phase will propagate into the cavity from both left and right sides (Fig. 7.1c), which makes this case computationally challenging. The mesh adaptivity capabilities of our numerical code made possible to accurately track the two solidification fronts identified by the iso-line $\theta = 0$. In the discussion below, the results will be presented using the physical time t_φ for the same reason mentioned above (note the influence of the size of the domain, since the scaling in Eq. (7.1) uses the height of the cavity).

The solidification process starts at physical time $t_\varphi = 185$ min (corresponding to $t = 250$) for the case CM and at $t_\varphi = 59$ min ($t = 78.8$) for the case PM.

7.1.1 Solidification after a complete melting (case CM)

The solidification follows after a complete melting corresponding to Fig. 6.2 at $t_\varphi = 185$ min ($t = 250$). The dynamics of the PCM during the solidification process is reported in Fig. 7.2, with the evolution of temperature distribution and solidification fronts.

At $t_\varphi = 185$ min (Fig. 7.2a), the liquid fraction is $L_f = 0.95$ and the melting/solidification front is close to the right wall of the cavity. Setting smoothly a low temperature $\theta_{co} = -1$ at the left wall, while the right wall is maintained at a constant temperature ($\theta_{right} = -0.01 \leq \theta_f$), triggers the formation of a second solidification front, propagating from the left side of the domain. Figures 7.2b and 7.2c illustrate that the left part of the cavity is solidifying at a faster rate because of the very low temperature imposed at the left wall, inducing a non symmetric evolution of solid-liquid interfaces. The solid part is represented in blue and corresponds to the region of temperature $\theta \leq 0$. The signature of the conductive heat transfer is characterized by the vertical shape of the left front. Inside the liquid, the initial convection cells facilitate the heat transfer from the boundaries, resulting in a very rapid decrease of the fluid temperature. Temperature gradients being smoothed out during this first stage, the influence of the convection inside the liquid region is considerably reduced. As a result, the velocity inside the liquid is reduced to very low values.

Starting with $t_\varphi = 430$ min (Fig. 7.2d), the shape of both interfaces is almost symmetrical. This is a signature of a conduction dominated process. At $t_\varphi = 510$ min (Fig. 7.2e) the liquid region starts to shrink at the bottom side of the cavity. This process is accelerated and finally the liquid is trapped in a thin pocket and finally disappears completely through the top of the cavity (Fig. 7.2e). The complete solidification ends at $t_\varphi = 530$ min, when the liquid fraction is $L_f = 0$.

The adapted mesh, refined along the two solidification fronts, at $t_\varphi = 300$ min is reported in Fig. 7.2f, illustrating the efficiency of the adaptive mesh tool.

7.1.2 Solidification after a partial melting (case PM)

In this case, the solidification starts from the state corresponding to Fig. 7.3a at $t_\varphi = 59$ min ($t = 78.8$), when the liquid fraction is $L_f = 0.5$. The temperature of the left wall is progressively lowered at $\theta_{co} = -1$, as in the previous solidification simulation.

The time evolution of the process is illustrated in Figs. 7.3a-e, while the adapted mesh corresponding to $t_\varphi = 90$ min is plotted in Fig. 7.3f. As in the previous case, a second solidification front starts to propagate from the left side of the cavity. The straight shape of the left solid front is always observed while the right solid front is impacted by the convection cell present in the central liquid region (Fig. 7.3b). The stronger convective effect is most likely due to the huge temperature difference that occurs over a smaller space distance (almost half of the volume is occupied by the solid state). This leads to stronger temperature gradients in the liquid region, and consequently to a stronger heat transfer. The two fronts merge to form a pocket of fluid which is connected to the top of the cavity (Fig. 7.3c-e).

It is interesting to note that, as in the previous solidification case, the left part is solidifying at a faster rate, hence the pocket of melted PCM disappears completely from the right at the top side of the cavity (Figs. 7.3c-e).

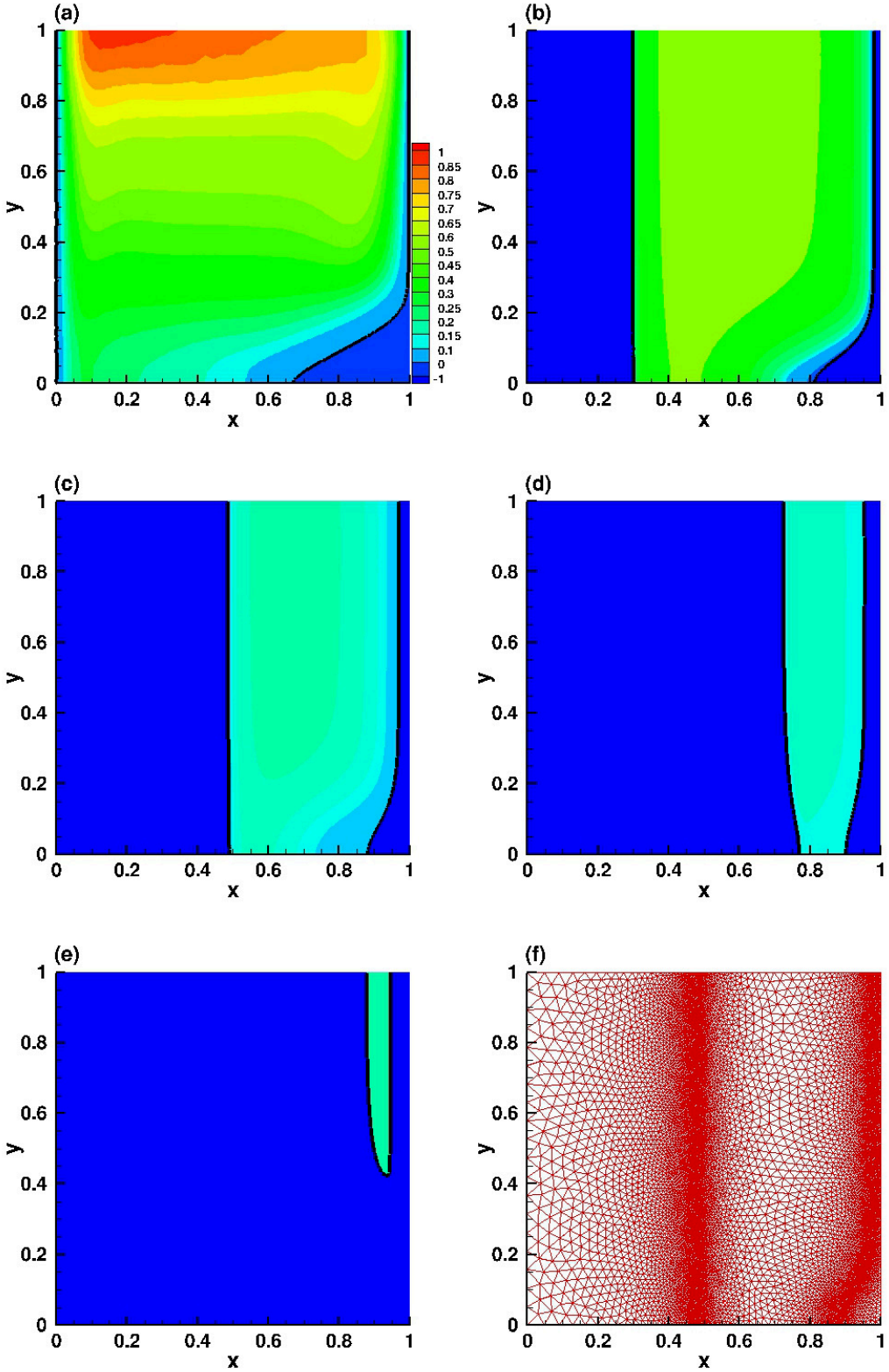

Figure 7.2: Solidification of the PCM: case CM. Temperature iso-lines in the liquid phase. The solid part is represented in blue and corresponds to the region of temperature $\theta_{co} \leq \theta_f = 0$. Time instants (panels a to e): $t_\varphi = 185$ min, $t_\varphi = 231$ min, $t_\varphi = 300$ min, $t_\varphi = 430$ min and $t_\varphi = 510$ min. The adapted mesh corresponding to $t_\varphi = 300$ min is plotted in panel (f). $\mathcal{R}a_{co} = 3.27 \cdot 10^5$.

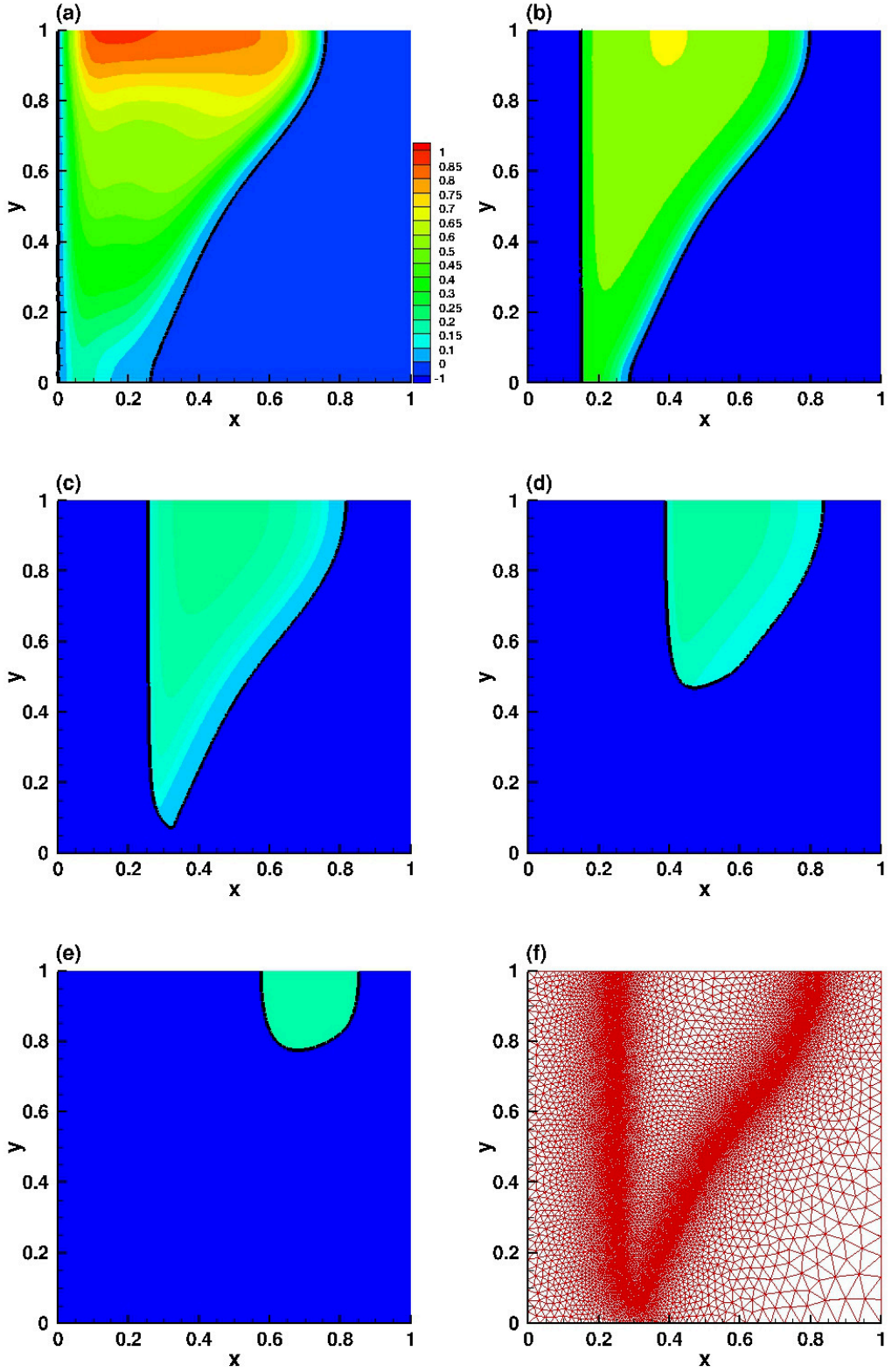

Figure 7.3: Solidification of the PCM: case PM. Temperature iso-lines in the liquid phase. The solid part is represented in blue and corresponds to the region of temperature $\theta_{co} \leq \theta_f = 0$. Time instants (panels a to e): $t_\varphi = 59$ min, $t_\varphi = 70$ min, $t_\varphi = 90$ min, $t_\varphi = 131$ min and $t_\varphi = 200$ min. The adapted mesh corresponding to $t_\varphi = 90$ min is plotted in panel (f). $\mathcal{R}a_{co} = 3.27 \cdot 10^5$.

7.1.3 Analysis of the solidification cycle from two different initial conditions: complete (case CM) and partial melting (Case PM)

The aim of this section is to investigate the temporal evolution of some physical properties of the solidification process, from two different initial conditions: **i)** completely melted volume (case CM) and **ii)** partially melted volume (50% of the fluid is melted, case PM). Figure 7.4 represents the temporal evolution of the liquid fraction L_f, the Nusselt number Nu, and the accumulated heat input Q_0 (Eq. (6.35)), for the two investigated cases. Note that the average Nusselt number is calculated at the cooled wall, defined similarly to Eq. (2.24), but it can be negative in this case. Simulations for three values $r_\delta = 1$, $r_\delta = 5$ and $r_\delta = 10$ were carried out.

Figure 7.4a illustrates the temporal evolution of the liquid fraction L_f for the CM case. Complete melting occurs for $t_\varphi = 185$ min, after which solidification starts, with a continuous decrease of L_f untill complete solidification is achieved. For the lowest value of r_δ, corresponding to $\mathcal{R}a_{co} = 3.27 \cdot 10^5$, the solidification process ends at $t_\varphi = 530$ min. Then, the higher the value of r_δ, the faster the discharge process. Final times for solidification are $t_\varphi = 260$ min and $t_\varphi = 230$ min for cases $\mathcal{R}a_{co} = 1.62 \cdot 10^6$ and $\mathcal{R}a_{co} = 3.27 \cdot 10^6$. These values of $\mathcal{R}a_{co}$ correspond to a drop of the cold boundary temperature by a factor of 5 and 10, respectively. The solidification speed, quantified by dL_f/dt_φ is nearly constant during almost the whole process for each case. This uniformity of the process indicates that the natural convection flow vanishes rapidly during the solidification, and conduction remains the only heat transfer mode. Figure 7.4b plots the temporal evolution of L_f for the PM case. As previously discussed, 50% of the volume is melted, at time $t_\varphi = 59$ min, when solidification starts. Furthermore, despite that solidification process is started, L_f continues to increase slightly at the very beginning of the discharge stage. Then it decreases monotonically towards 0 at $t_\varphi = 240$ min. The heat stored in the melted PCM continues to melt the remaining solid PCM until the convection becomes negligible. It is worth noticing that this behavior is not observed in the complete melting case because of the imposed temperature at the right wall.

Let us now pay attention to the transfers occurring at the left wall, progressively submitted to a lower temperature. This is done through the temporal evolution of the Nusselt number and the accumulated heat input. Panels (c) and (d) of Fig. 7.4 illustrate the Nusselt number for the CM and PM cases. The three investigated Rayleigh numbers are shown, with clear differences between them. This difference corroborates with that already reported for the melting case, over shorter times scales. This indicates that the heat transfer during the solidification process is fundamentally different from the melting one. For the CM case, for $\mathcal{R}a_{co} = 3.27 \cdot 10^5$, the Nusselt number first decreases sharply, for $t_\varphi \leq 18$ min, then it reaches a plateau at $\mathcal{N}u = 7$ during the complete melting. At $t_\varphi = 185$ min, solidification starts and $\mathcal{N}u$ suddenly decreases over very short times, reaching negative values ($\mathcal{N}u \approx -15$). It follows an increase of $\mathcal{N}u$ with time, up to reaching an asymptotic value close to 0 (zero temperature gradients, *i. e.* uniform temperature at the left wall). The same mechanism is observed over a shorter time interval when $\mathcal{R}a_{co}$ is increased. For the PM case, the Nusselt number also decreases sharply to a negative value when the solidification starts. However, the convection flow remaining in the melted region influences the heat transfer at the very beginning of the solidification process. The hot fluid in the middle of the melted PCM is advected by the natural convection flow to the boundaries and induces a temperature gradient at the left wall, resulting into an oscilating behavior of the Nusselt number before reaching an asymptotic value. This is in agreement with the previous comment about the melting continuing in the right part of the cavity, despite that solidification has started, and the slight increase of the liquid fraction at the very first time steps of the discharging process.

Both charge and discharge cycles are better illustrated by the time evolution of the accumulated heat

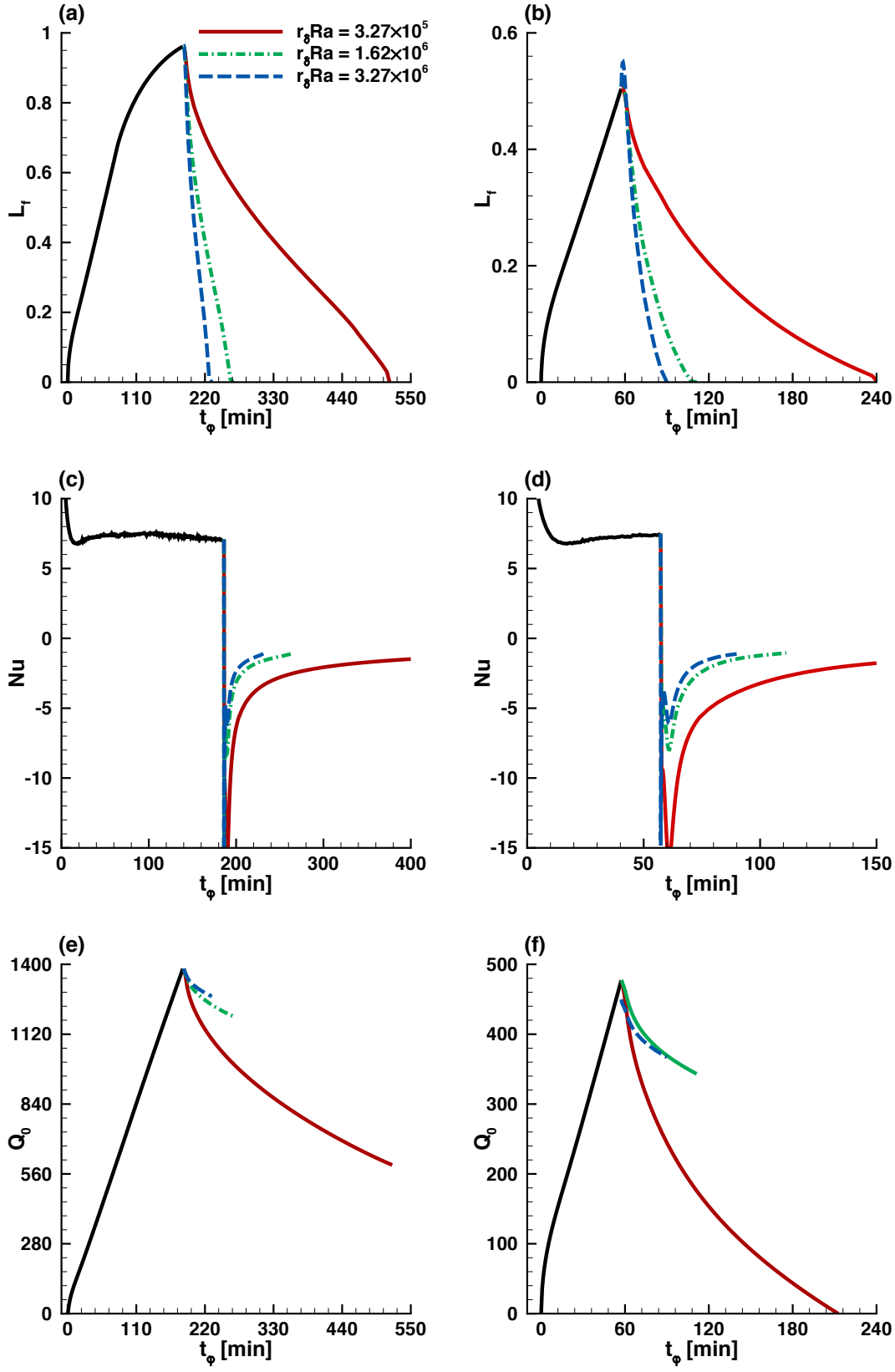

Figure 7.4: Temporal evolution of the liquid fraction (L_f), the Nusselt number $\mathcal{N}u$, and the accumulated heat input Q_0 during the entire melting-solidification cycle. Case CM (left) and case PM (right).

Q_0 defined in Eq. (6.35), as it is shown in panels (e) and (f) of Fig. 7.4. Heat is first stored during the melting stage, corresponding to $t_\varphi \leq 185$ min for CM (Fig. 7.4d) and $t_\varphi \leq 59$ min for PM (Fig. 7.4e). It is then restored during the solidification stage. The CM case indicates higher value of Q_0 ($Q_0 = 1400$, for $\mathcal{R}a_{co} = 3.27 \cdot 10^5$) compared to the PM case ($Q_0 = 500$), meaning that the PCM is more efficient in terms of heat storage. However, the PM case exhibits well balanced characteristic times between the solidification and the melting stages for $\mathcal{R}a_{co} = 3.27 \cdot 10^5$. Besides, when the $\mathcal{R}a$ number increases, the stored heat is discharged faster. Moreover, the temperature and the velocity profiles drop sharply during the first step of the cooling process and become almost equal to zero very early in the whole domain. This means that conduction dominates the solidification process, and the convection becomes rapidly negligible. As a consequence, the melting fronts are vertical and have a symmetric position with respect to the center of the cavity.

7.2 Melting-solidification cycle of a cylindrical PCM

We are focusing in this section on the solidification of cylindrical PCM of radius $R = 1$ with an inner cooled tube. This configuration is used for heat storage systems. The simulation of the solidification process starts by imposing progressively at the inner tube a constant cooling temperature $\theta_{co} = -1$. The outer tube is adiabatic and a no-slip boundary condition is applied for the velocity. The solidification part of the cycle occurs at $t = 2.5$ when 80% of the initial solid PCM is melted. A solid layer grows around the tube and joins the remaining solid PCM.

Figure 7.5 shows the time evolution of the solidification process for $r_\delta = 1$. The simulation resumes from the melting state presented in Fig. 5.10. The low temperature at the inner tube triggers a second solid-liquid interface, propagating from the center to the outer tube (see panels a and b). Both solidification fronts merge at $t = 4.34$ (panel c), followed by a shrinking process of the liquid (panel d and e) which disappears completely at $t = 6.7$ (panel d). We note that, as emphasised in Sec. 7.1, the heat transfer is dominated by conductive transfer during the solidification cycle, explaining the circular evolution of the solidification front. The adapted mesh corresponding to $t = 3.16$ is shown in panel (f), illustrating the refined mesh along the two interfaces $\theta = 0$.

From the scaling analysis (6.4), the radial expansion δ_r of the solidification front from the center could be approximated by

$$\delta_r = \sqrt{\frac{\mathcal{S}te}{\mathcal{P}r} \times t}. \tag{7.2}$$

The solidification time could be thus predicted by

$$t_{sol} = \delta_r^2 \frac{\mathcal{P}r}{\mathcal{S}te}. \tag{7.3}$$

In our case, by taking into account the remaining solid located at $\delta_r = 0.8$, the theoretical solidification time is $t_{sol} = 6.4$, which is in relatively good agreement with our numerical results. Increasing the Stefan number should hence result in a lower value of the solidification time.

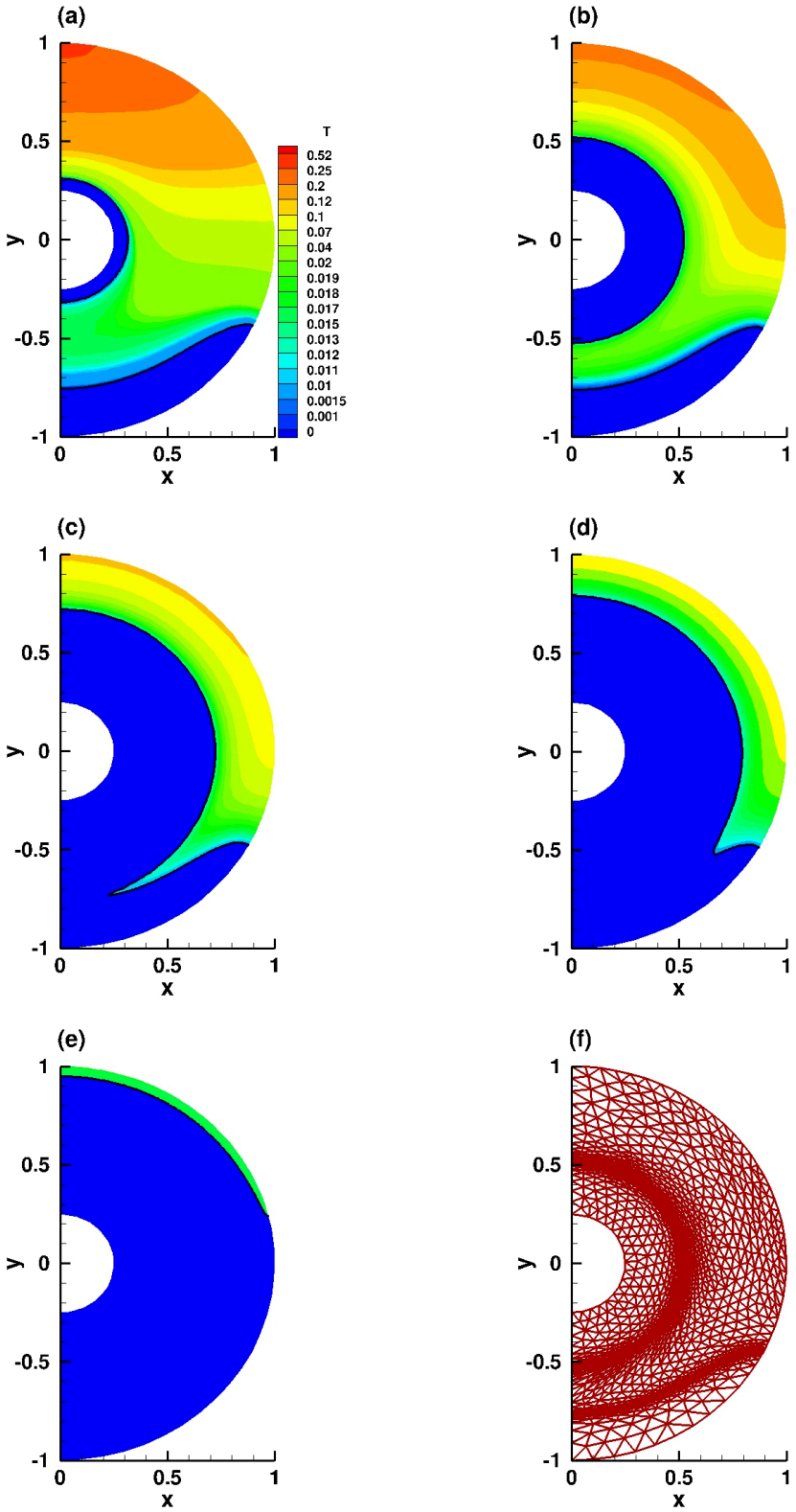

Figure 7.5: Solidification of a cylindrical PCM. Temperature iso-lines in the liquid phase. The solid part is represented in blue and corresponds to the region of temperature $\theta_{co} \leq \theta_f = 0$. Time instants (panels a to e): $t = 2.69$, $t = 3.16$, $t = 4.34$, $t = 4.94$ and $t = 6.66$. The adapted mesh corresponding to $t = 3.16$ is plotted in panel (f). $\mathcal{R}a_{co} = 5 \cdot 10^4$.

7.2.1 Concluding remarks

The choice of simulating the complete cycle melting-solidification of n-octadecane PCM in this chapter is motivated by the fact that this material is generally used for buildings applications, due to its phase change temperature of 28^oC. Zhu et al. (2009) and Kalnæs and Jelle (2015) listed various applications, starting from free cooling, peak load shifting, passive building systems and solar energy storage. For each case, the PCM is assumed to melt during day-time and to solidify during the night-time.

It was noticed that, when the same Rayleigh number is considered to compare the melting and solidification cycles, meaning that the charge and the discharge modes occur at the same δT, the solidification is always slower than the melting. This behavior is linked to the heat transfer mode leading each part of the cycle. Convective heat transfer dominates indeed the melting process, enhancing thus the heat transfer, while conduction is the main heat transfer mode during solidification, resulting into a slower operating process. However, when the discharge temperature is decreased by a factor of 5, i.e both $\mathcal{R}a_{co}$ and $r_\delta \times \mathcal{S}te$ are increased, the solidification and the melting occur over similar times.

A first issue that has been brought up by Ascione et al. (2014) is the difficulty of the PCM systems to completely discharge during night-time. Though, if the PCM does not solidify entirely, the effectiveness of the system may be considerably reduced. In this case, to have a shorter cooling period, it is not advised to melt the PCM completely.

However, for solar energy storage applications, full melting of the PCM is needed to utilize its latent heat storage capacity. Hence, a partial melting is not optimal. For other applications, when a shorter discharge time is desired, the use of external cooling techniques is needed to ensure a colder discharge temperature.

8 Numerical simulation of 3D convection and PCM configurations using domain decomposition methods

Several sections of this chapter are from the paper [G. Sadaka, A. Rakotondrandisa, F. Luddens, C. Lothodé, P-H. Tournier, I. Danaila, *Parallel finite-element codes for the simulation of solid-liquid phase-change systems with natural convection*, to be submitted, 2019].

We present in this chapter parallel computations of three-dimensional liquid-solid phase-change systems involving natural convection. We use the recent library `ffddm` that makes available in FreeFem++ a state-of-the-art scalable Schwarz domain decomposition method (DDM). Our motivation to expand our numerical model to 3D configurations is drawn by the lack of publications in the literature presenting accurate 3D simulations of phase-change materials. Also, experimental investigations against which we have validated our numerical method in previous chapters involve three-dimensional effects that we have assumed to be negligible in our comparisons. The latter assumption is however not valid for high $\mathcal{R}a$ numbers.

The main feature of our numerical approach is the use of 3D adaptive mesh, performed using *mmg3d* library. *Mmg3d* is a 3D software developed by Dobrzynski (2012), which allows to remesh an initial mesh made of tetrahedra. The metrics for the mesh adaptation are computed using *mshmet* library, which provides anisotropic metrics based on solution variations. Since the mesh adaptivity procedure is based on a sequential algorithm, we compute first the metrics with respect to the coarse mesh. Then, finer meshes are generated before the mesh decomposition step in order to reach the desired level of refinement for the subdomains. We use *Metis* library to split the domain into subdomains. The number of layers of mesh elements in the overlap region between subdomains is set to 2 for all subsequent simulations. For three-dimensional applications, direct solvers used in the framework of 2D problems are not appropriate and iterative methods must be employed since memory requirements for the *LU* decomposition would rapidly exceed the capacity of available computers. The linear system of equations resulting from the Newton linearization are thus solved using a parallel *GMRES* Krylov method. Since it is well known that iterative methods can suffer from convergence problems, we adapt the number of subdomain in such a way that each processor could handle $1,000$ tetrahedra. The Optimized Restricted Additive Schwarz (ORAS) preconditioned *GMRES* solver proved to be extremely efficient since around 30 iterations were necessary to get a residual of 10^{-9} for each Newton iteration.

The remainder of this chapter is as follows. In Sec. 8.1, we validate the 3D convection of air in a cubic cavity against the numerical benchmark by Wakashima and Saitoh (2004), and compare together the solutions obtained using the parallel and the sequential algorithms. The convection of water is investigated in Sec. 8.2. Then, the melting of n-octadecane PCM inside 3D enclosures is addressed in Sec. 8.3. We finally present in Sec. 8.4 the challenging numerical simulation of water freezing.

8.1 Numerical simulation of the natural convection of air in a cubic cavity

Following the same argument of increasing gradually the complexity of computed cases, that was outlined in Chapters 4 and 5, we start by presenting the natural convection of air. This case involves a linear buoyancy force f_B. The physical parameters are the same that used in the 2D simulations ($\mathcal{P}r = 0.71$) and we investigate Rayleigh numbers ranging from $\mathcal{R}a = 10^4$ to $\mathcal{R}a = 10^6$. The walls are rigid and impermeable. The vertical walls at $x = 0$ and $x = 1$ are isothermal and have different temperatures $\theta_h = 1$ and $\theta_c = 0$, respectively. The other walls are considered adiabatic. The fluid is initially at rest and the temperature is linearly distributed from the cold to the hot walls. We solve the steady Eq. (3.14) by increasing smoothly the parameter α in front of the Boussinesq term (which can be assimilated to a Rayleigh continuation step) with a maximum of 6 steps for $\mathcal{R}a = 10^6$.

We first compare the current simulation with the numerical data of Wakashima and Saitoh (2004). These authors used a forth order finite difference method, with a vorticity-stream function formulation with different uniform meshes of $120 \times 120 \times 120$ grid nodes. Our results were obtained using uniform grids of $40 \times 40 \times 40$. Since the converged flow pattern and temperature distributions are symmetrical with respect to the center of the cavity for the investigated Rayleigh number, we display in Fig. 8.1 the temperature field at the mid section ($y = 0.5$), for each of the three Rayleigh numbers $\mathcal{R}a = 10^4$ (top), $\mathcal{R}a = 10^5$ (middle), $\mathcal{R}a = 10^6$(bottom). On the left we display the numerical results of Wakashima and Saitoh (2004) and on the right the present simulation. The comparison with the benchmark solution exhibits a good qualitative agreement. The higher the Rayleigh number, the finer the thermal boundary layer thickness is in the vicinity of the vertical walls. One can also notice the stagnant fluid with stratified temperature in the center of the domain in both numerical solutions.

A more accurate comparison is presented in Tab. 8.1 between the present simulation and numerical data from the literature.

	u_{max} (z_{max})	w_{max} (x_{max})
$\mathcal{R}a = 10^4$	0.198094 (0.826772)	0.220973 (0.11811)
Wakashima and Saitoh (2004)	0.1984 (0.8250)	0.2216 (0.1177)
Moglan (2013)	0.1859 (0.8230)	0.2234 (0.1172)
$\mathcal{R}a = 10^5$	0.140367 (0.850394)	0.245454 (0.0629921)
Wakashima and Saitoh (2004)	0.1416 (0.8500)	0.2464 (0.0677)
Moglan (2013)	0.1461 (0.8540)	0.2459 (0.0703)
$\mathcal{R}a = 10^6$	0.0809247 (0.858268)	0.257719 (0.0393701)
Wakashima and Saitoh (2004)	0.08111 (0.8603)	0.2583 (0.0323)
Moglan (2013)	0.0830 (0.8550)	0.2553 (0.03905)

Table 8.1: Natural convection of air in a 3D differentially heated cavity. Maximum values u_{max} and w_{max} of the velocity profiles at mid-domain ($x = 0.5$ and $z = 0.5$, respectively) and their locations z_{max} and x_{max}. Comparison with benchmark solutions of Wakashima and Saitoh (2004) and numerical data of Moglan (2013) for $\mathcal{R}a = 10^4$, $\mathcal{R}a = 10^5$, $\mathcal{R}a = 10^6$.

We compare the maximum velocity values and their corresponding location with benchmark solution of Wakashima and Saitoh (2004) and numerical results of Moglan (2013). Our results show a good

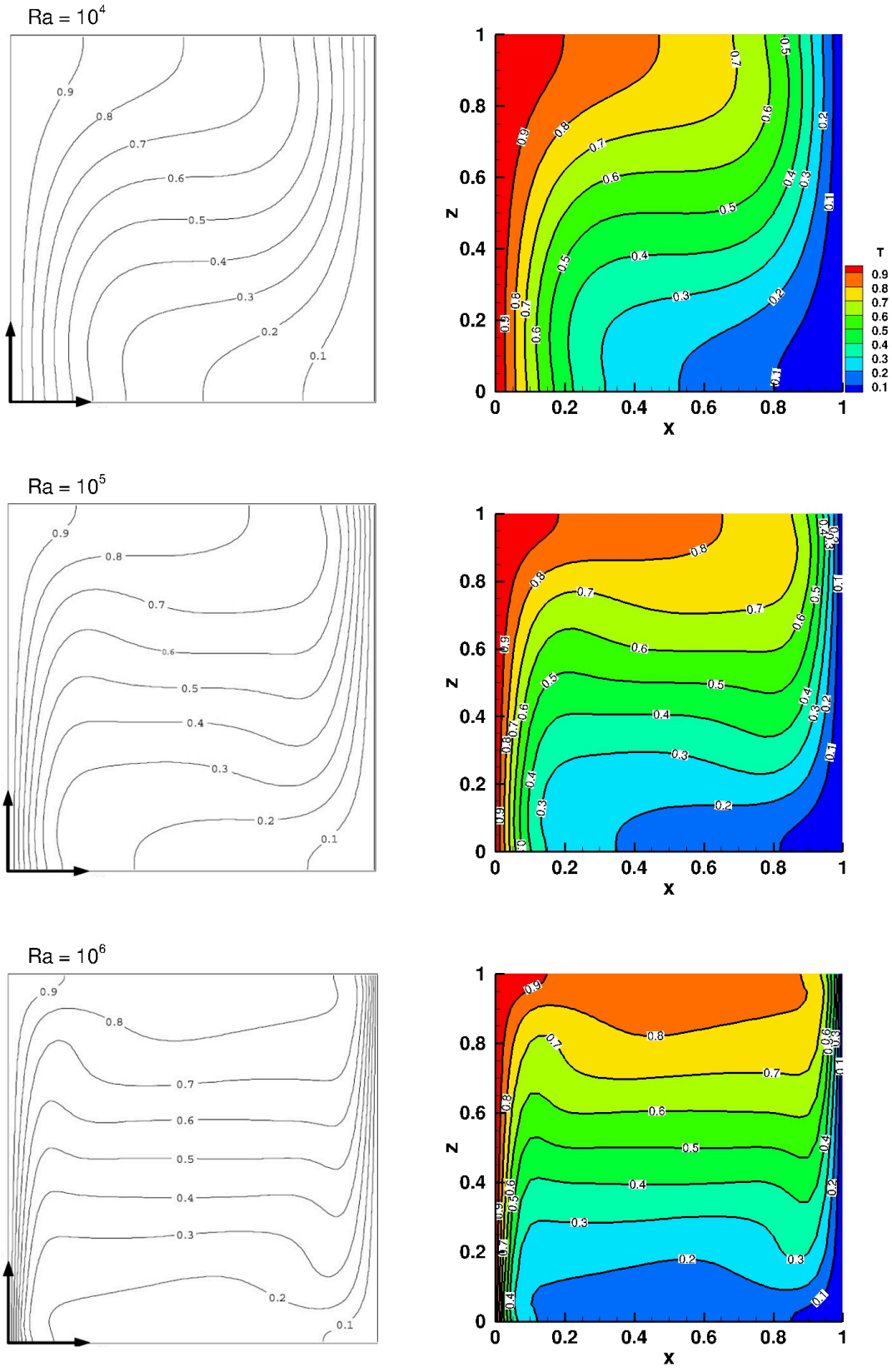

Figure 8.1: Natural convection of air in a 3D differentially heated cavity. Temperature contours at the mid-plane of ($y = 0.5$). Comparison with the results of Wakashima and Saitoh (2004) (left images).

convergence on a mesh 3 times coarser than the one proposed by Wakashima and Saitoh (2004). A good agreement is found for all values of the Rayleigh number. For $\mathcal{R}a = 10^4$ the current simulation shows a relative difference of 0.15% for u_{max} and 0.28% for v_{max}. Larger differences of 6.55% is found with the results reported by Moglan (2013). We recall that Moglan (2013) used a second-order finite difference scheme on a $64\times64\times64$ grid. For $\mathcal{R}a = 10^5$ and 10^6 the results are in good agreement with both references.

Further comparison of the parallel solver with the sequential algorithm is offered in Tab. 8.2 for all cases. We compute L^2 and L^∞ norms for the velocity and the temperature. The number of subdomains varies from 28 to 70 for 1.8 millions of unknowns. The difference between the two algorithms is of order of 10^{-6} and we do not observe a large variation of the error when the number of subdomains is increased. The comparison with the sequential algorithm was limited to the $40 \times 40 \times 40$ grid, since the simulations are highly demanding in CPU time. For the highest value of the Rayleigh number, the steady state computation required 57 CPU hours and 3 runs (restarts) with 120 Go of memory for the sequential algorithm. The computational time is considerably reduced using DDM in 3D simulations. This becomes affordable since only 21 CPU minutes were necessary with 70 processors to compute the same case with an error of $6.02152 \cdot 10^{-6}$ on $\boldsymbol{u}$ and $4.50094 \cdot 10^{-6}$ on θ.

$\mathcal{R}a$	*nb proc*	$\|\|u\|\|_2$	$\|\|u\|\|_\infty$	$\|\|T\|\|_2$	$\|\|T\|\|_\infty$
10^4	28	$1.12496 \cdot 10^{-6}$	$3.1 \cdot 10^{-6}$	$3.09966 \cdot 10^{-6}$	$7 \cdot 10^{-6}$
	42	$1.53698 \cdot 10^{-6}$	$5.1 \cdot 10^{-6}$	$3.23352 \cdot 10^{-6}$	$8 \cdot 10^{-6}$
	56	$1.55576 \cdot 10^{-6}$	$5.1 \cdot 10^{-6}$	$3.4342 \cdot 10^{-6}$	$8 \cdot 10^{-6}$
	70	$1.25622 \cdot 10^{-6}$	$3.6 \cdot 10^{-6}$	$3.56048 \cdot 10^{-6}$	$8 \cdot 10^{-6}$
10^5	28	$1.73254 \cdot 10^{-6}$	$6.1 \cdot 10^{-6}$	$2.40467 \cdot 10^{-6}$	$7 \cdot 10^{-6}$
	42	$2.84973 \cdot 10^{-6}$	$7.78 \cdot 10^{-6}$	$3.53003 \cdot 10^{-6}$	$9 \cdot 10^{-6}$
	56	$3.00832 \cdot 10^{-6}$	$7.39 \cdot 10^{-6}$	$4.17769 \cdot 10^{-6}$	$1.1 \cdot 10^{-5}$
	70	$3.68118 \cdot 10^{-6}$	$9 \cdot 10^{-6}$	$4.70846 \cdot 10^{-6}$	$1.2 \cdot 10^{-5}$
10^6	28	$6.61804 \cdot 10^{-6}$	$1.826 \cdot 10^{-5}$	$3.46504 \cdot 10^{-6}$	$1.1 \cdot 10^{-5}$
	42	$5.93966 \cdot 10^{-6}$	$1.5 \cdot 10^{-5}$	$3.98082 \cdot 10^{-6}$	$1.2 \cdot 10^{-5}$
	56	$7.05144 \cdot 10^{-6}$	$1.9247 \cdot 10^{-5}$	$5.0044 \cdot 10^{-6}$	$2 \cdot 10^{-5}$
	70	$6.02152 \cdot 10^{-6}$	$1.68 \cdot 10^{-5}$	$4.50094 \cdot 10^{-6}$	$1.8 \cdot 10^{-5}$

Table 8.2: Natural convection of air in a 3D differentially heated cavity. Comparison between sequential and DDM algorithms for uniform grids of $40 \times 40 \times 40$ points.

8.2 Numerical simulation of the natural convection of water in a cubic cavity

In this section, we simulate the natural convection of water inside a cubic cavity using adaptive 3D meshes. The dimensionless parameters are the same that used in Chapter 4.2 ($\mathcal{R}a = 2.518084 \cdot 10^6$ and $\mathcal{P}r = 6.99$). We impose cold dimensionless temperature $\theta_c = 0$ at $x = 1$ (right wall), hot temperature $\theta_h = 1$ at $x = 0$ (left wall), and a homogeneous Neumann boundary condition at the other walls. Dirichlet boundary condition $\boldsymbol{u} = 0$ is prescribed over the whole boundary $\partial\Omega$. In view of anomalous thermal variation of water density, we adapt the mesh along $\theta = 0.4$ to capture correctly the flow structure. The main limitation of 3D simulations of water convection in the literature is the size of the mesh resolution when fixed grid models are used. As an example, Giangi et al. (2000) and Michalek and Kowalewski (2003) presented a mesh sensitivity analysis, and concluded that even by using 81^3 grid points, the variation of the velocity was still significant, making the problem computationally expensive.

The temperature distribution and the corresponding adapted mesh for the steady state computation is shown in Fig. 8.2a. The blue region denotes the cold water trapped by the abnormal fluid recirculation and the red region the hot fluid driven by the upper clockwise circulation. A zoom of the mesh at the mid-plane is also offered in Fig. 8.2b. Smaller tetrahedra are clearly observed in the vicinity of the walls, where a spiral movement of the fluid occurs along the walls, and between the two counter-rotating circulation patterns. A minimum edge length $h_{min} = 3.33 \cdot 10^{-3}$ is used along the maximum density variation, and $h_{max} = 0.15$ in the stagnant fluid region. The combined mesh adaptation strategy and the efficient parallel algorithm, allow us to reduce considerably the computational time. Only 5012.04 CPU seconds were necessary to compute the steady solution with $500,000$ tetrahedra using 56 processors, while Michalek et al. (2005) needed 3.6×10^5 CPU seconds to compute the steady solution with a 81^3 fixed grid.

In many cases, it is convenient to perform two-dimensional numerical simulations, to reduce the computational effort and allow many simulations to be achieved in a realistic time. However, Fig. 8.2b shows that the three-dimensionality of the flow in a cube shape cavity affects the topology of the iso-surface $\theta = 0.4$. Giangi et al. (2000) assessed on the effect of three-dimensionality in both convection and freezing of water and they noted that only the flow in the symmetry plane can be considered as two-dimensional. The no-slip velocity and the adiabatic thermal boundary conditions at the side walls enhance the three-dimensional effect near the walls. Furthermore, these authors noted that, even though the temperature profiles at the central cross-section of the cavity match well for both 2D and 3D simulations, important differences between two and three-dimensional velocity profiles are present.

In Figs. 8.2d-f, we plot the velocity profiles along the vertical line passing through the velocity saddle point, where normal and abnormal convection streams collide in the vicinity of the cold wall. For the $\boldsymbol{e}_z$ component of the velocity, the profile along the $z-$direction at $x = 0.93$, for both two and three-dimensional simulations is compared with the 3D simulation of Michalek and Kowalewski (2003). Triangular symbols denote the reference solution, obtained with a 3D finite difference code using vorticity-vector potential formulation of the Navier-Stokes and energy equations. 3D (red solid line) profile agrees well with the benchmark solution with a maximum difference of 3%. The 2D (green dashed line) solution exhibits higher discrepancies in the vicinity of the anomalous density variation, where the three-dimensional effect is maximum. However, as noted by Giangi et al. (2000) in their experimental observations, larger differences between 2D and 3D solutions could be observed at $x = 0.1$ and $x = 0.5$. Panels (e) and (f) exhibit discrepancies greater than 10% between both solutions, in agreement with the foregoing observation.

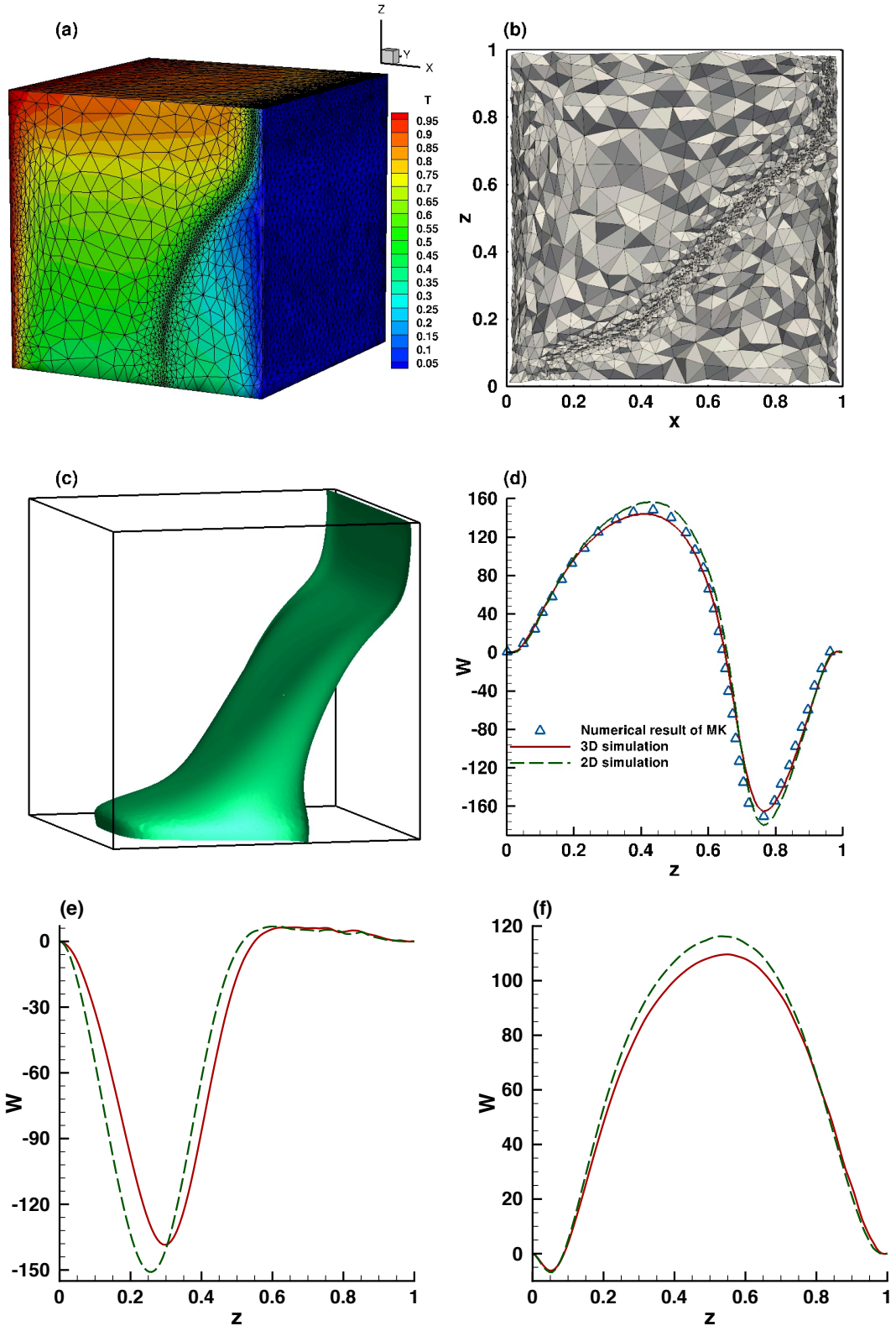

Figure 8.2: Natural convection of water in a cube-shape cavity. (a) Temperature distribution and adapted mesh. (b) Zoom of the 3D adapted mesh at mid-plane. (c) Iso-surface $\theta = \theta_m$. Comparison of the profile of the vertical velocity along the $z-$direction with the numerical benchmark by Kowalewski and Rebow (1999) at the mid-plane ($y = 0.5$) and $x = 0.93$ (d); $x = 0.1$ (e); $x = 0.5$ (f).

8.3 Numerical simulations of melting PCM with convection in a 3D configuration

We now proceed to the 3D simulation of solid-liquid phase-change problems, starting with the melting of a PCM in a cube-shape domain. The three-dimensionality of the fluid flow can lead to major differences with the two-dimensional solution in some configurations, as in the example of the melting of Gallium. Nikrityuk (2012) showed that the controversial multi-cellular flow occurs only at the beginning of the melting process in two-dimensional simulations. Three-dimensional simulations exhibit the absence of a multi-cellular structure at any time step. They explained these differences by the presence of walls in the third direction, which suppresses the flow. Also, the occurrence of weak turbulence in the bulk of the melt prevents the formation of the long-living multicellular flow pattern known from 2D simulations. The three-dimensional geometry allows the fluid movement in all directions and the friction effect provided by no-slip walls in the transverse direction influences the flow. Nikrityuk (2012) highlighted the existence of a secondary flow in the transverse direction, as shown in Fig. 8.3, which has its maximal intensity near the side walls.

We expand the 2D simulations presented in Chapter 5 to 3D configurations. Solutions obtained by both configurations are compared to assess on the three-dimensional effects that occur during the melting process. The configuration of the numerical simulation is sketched in Fig. 8.3. The physical parameters of the run are: $\mathcal{R}a = 3.27 \cdot 10^5$, $\mathcal{P}r = 56.2$, and $\mathcal{S}te = 0.045$. The PCM is set initially solid throughout the whole domain. As the heating progresses, the natural convection intensifies enough to have a pronounced influence on the shape of the interface. The shape of the phase-change front at $t = 78.7$ is displayed in Fig. 8.3, showing a nonuniform melting front receding from the top to the bottom of the domain.

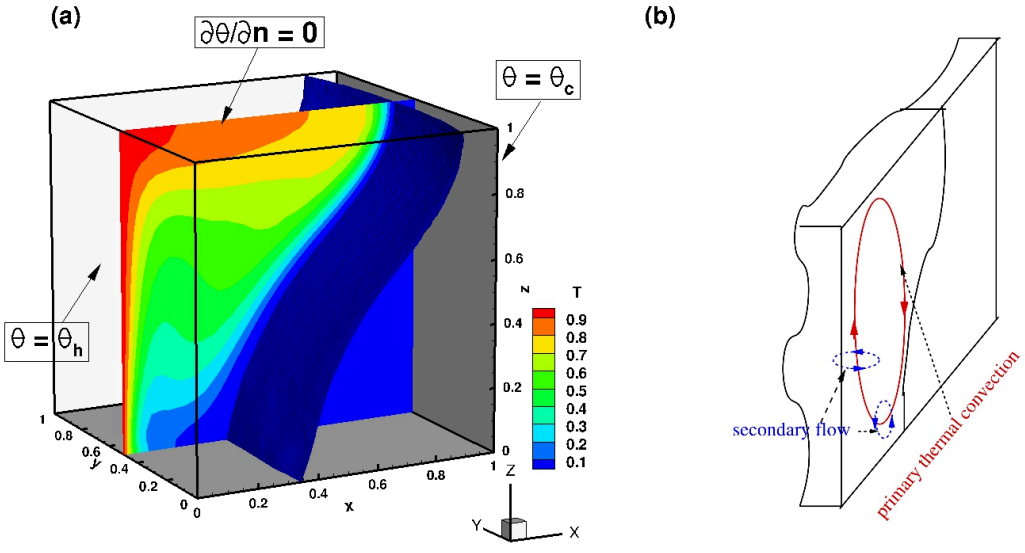

Figure 8.3: Melting of a phase-change material. Problem definition, shape of the solid-liquid interface at $t = 78.8$, and temperature distribution in the symmetry plane (a). Scheme of 3D convection flow near the side wall by Nikrityuk (2012) (b).

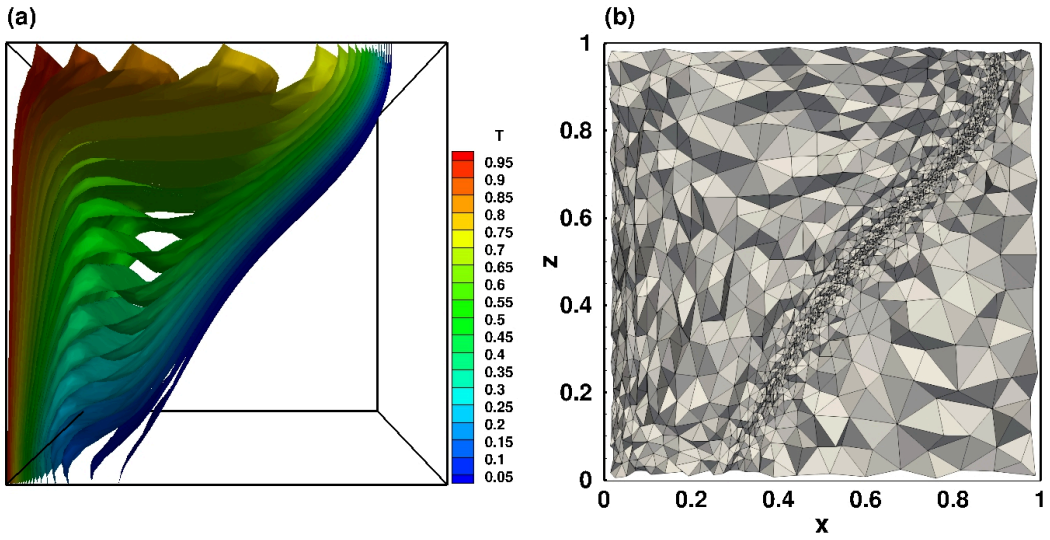

Figure 8.4: Melting of a phase-change material. Temperature iso-surfaces (a) and the corresponding adapted mesh (b) at $t = 78.8$.

Iso-surfaces of the temperature at $t = 78.8$ are offered in panel (a) of Fig. 8.4. The melting front is influenced by the flow which rises along the hot wall and moves down along the solid-liquid interface, where it is cooled. The influence of the secondary flow, defined by Nikrityuk (2012), is apparent with respect to the curved shape of the interface in the vicinity of the side-walls in the transverse direction. The adapted mesh at $t = 78.8$, refined along the iso-surface $\theta = 0$, is shown in Fig. 8.4b.

The location of the solid-liquid interface at the mid-plane and the time evolution of the Nusselt number for two and three-dimensional configurations are plotted in Fig. 8.5. The position of the interface in panel (a) displays discrepancies between both melting fronts, but the shape remains in good agreement. These differences are caused by the increase of the velocity in the liquid flow, induced by the three-dimensional effects, as shown by Nikrityuk (2012), who compared the volume-averaged velocity U_{xyz}, defined as follows:

$$U_{xyz} = \int_{\Omega} \sqrt{u_1^2 + u_2^2 + u_3^2}\, dV. \tag{8.1}$$

In our simulations, at $t = 78.7$, we obtained $U_{xyz} = 0.548208$ for 3D simulations and $U_{xy} = 0.519576$ for 2D. However, the time evolution of the heat transfer in panel (b) matches well for 2D and 3D simulations, with a maximum difference lower than 1% at the onset of the convection time, and overlap during all the simulation time. From an engineering point of view, the latter observation means that if only an assessment of the heat transfer during the phase-change process is sought, a 2D simulation is enough since it could be performed in a reasonable computational time. The 3D simulation required 2 days of CPU time with 200 processors, while 45 minutes on a personal computer is enough for the 2D configuration, for the investigated Rayleigh number.

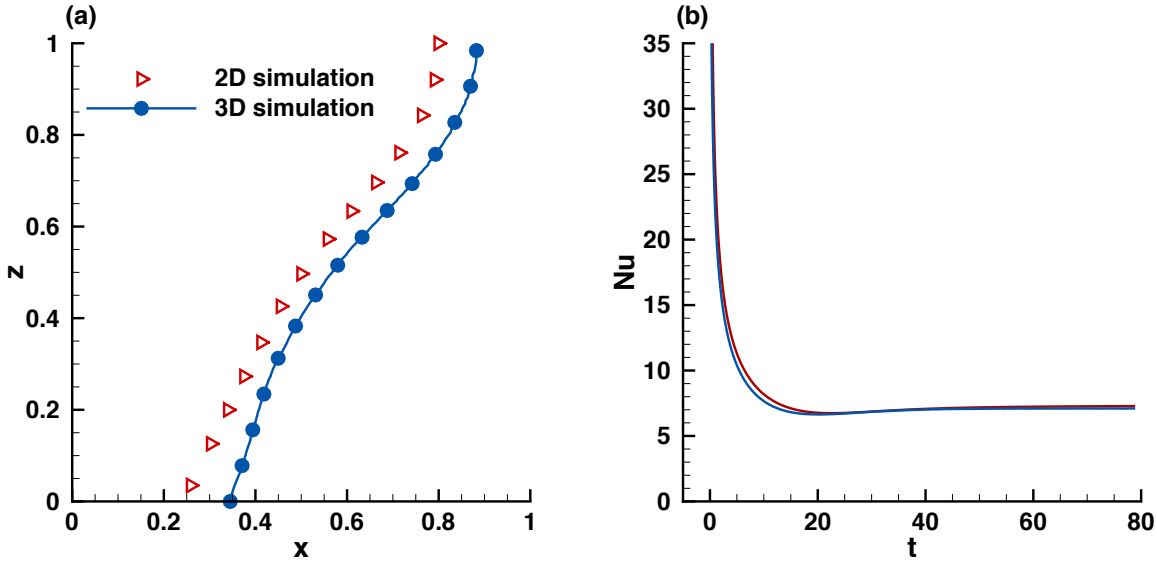

Figure 8.5: Comparison between 2D and 3D solutions. Location of the interface at $t = 78.7$ (a) and the Nusselt number at $x = 0$ (b).

8.4 Numerical simulation of water freezing in a cubic cavity

In this section, we present a 3D simulation of the challenging case of ice formation inside a differentially heated cubic cavity. Starting from the steady solution shown in Fig. 8.2, we drop the cold temperature at the right wall from $\theta_c = 0$ to $\theta_c = -1$, under the temperature of fusion (which correspond to physical temperatures $T = 0\,^oC$ and $T = -10\,^oC$, respectively). Solid crust arises thus from the cold wall and expands towards the left wall.

The temperature distribution and the adapted mesh at final time $t_\varphi = 2340$ s ($t = 1.61$) are displayed in Figs. 8.6a and 8.6b. When compared with the natural convection case in Sec. 8.1, the mesh is additionally adapted along the solid moving front, localized by the temperature iso-surface $\theta = 0$. For the visual identification of flow structures during the ice formation, panel (c) plots the snapshots of velocity vectors, the iso-surface $\theta = 0.4$ along the anomalous density variation, and the phase-change front at time instant $t = 1.61$. The effect of the secondary flow, discussed in Sec. 8.3, is also visible on the curved shape of the iso-surface $\theta = \theta_m$ in the transverse $y-$ direction. One can note however, that the solidification front is almost 2D. The buoyancy-induced fluid motion in the abnormal recirculation region is too weak to influence the solid front. Finally, the overlay of the experimental image of Kowalewski and Rebow (1999) and the current simulation exhibits good agreement for the location of the solid-liquid interface. Differences come mainly from the fact that the undercooling phenomenon during the solidification stage is not taken into account in our model. However, the global shape of the interface agrees qualitatively with the experimental observation.

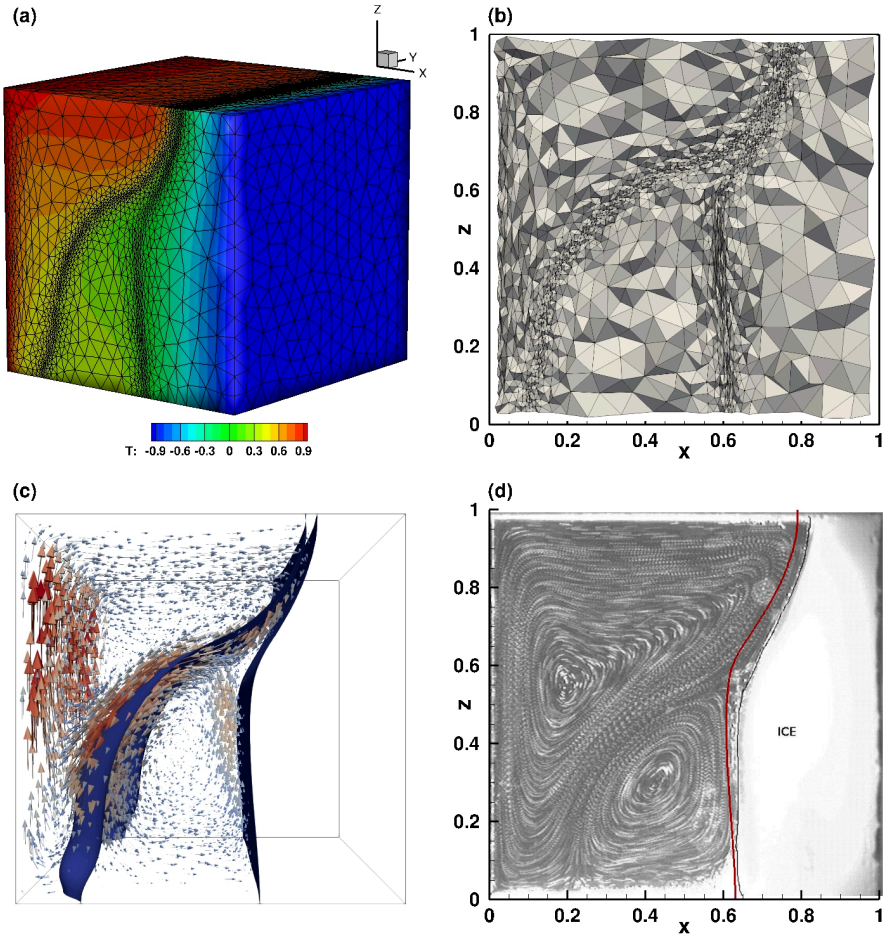

Figure 8.6: Freezing of pure water in a 3D cubic cavity. (a) Temperature distribution and adapted mesh at $t_\varphi = 2340[s]$. (b) Zoom of the adapted mesh at the mid-plane. (c) Temperature iso-surfaces $\theta = 0.4$ and $\theta = 0$ with velocity vectors in the liquid phase. (d) Superimposition of the interface obtained in the present simulation (red line) on the experimental image of Kowalewski and Rebow (1999).

8.5 Concluding remarks

We developed parallel 3D tools using domain decomposition methods to simulate natural convection flows involving melting or solidification boundary conditions. The numerical simulations performed with the recent library `ffddm` in FreeFem++ showed good agreement with the benchmark solutions and the sequential algorithm for all simulated cases. The qualitative behavior and the topology of the interface for phase-change problems were discussed in detail. Three-dimensional effects in the flow were exhibited by the deformed shape of the interface in the transverse direction. The adaptive 3D mesh procedure proved very efficient to capture several interfaces, as in the example of the water freezing. Grid refinement effort was concentrated only in regions displaying high gradients of the computed variables, and 10 times larger tetrahedra were generated elsewhere.

9 Conclusion and perspectives

In this thesis, we presented numerical simulations of natural convection with melting boundary. We developed numerical tools for simulating 2D and 3D configurations of solid-liquid phase-change systems involving natural convection, using adaptive finite elements method.

The buoyancy-induced fluid motion in the liquid phase was modeled by the incompressible Navier-Stokes equations with Boussinesq approximation. The phase-change was modeled by an enthalpy-porosity model using a temperature-based formulation for the energy conservation equation. A single-domain method, solving the same system of equations in both phases, including a Carman-Kozeny-type penalty term in the momentum equation, was implemented with the FreeFem++ software.

In the numerical approach, the coupled momentum and energy equations were integrated in time using a fully implicit second-order GEAR scheme. The space discretization was based on a Taylor-Hood triangular finite elements, approximating the velocity and the pressure with $\mathbb{P}_2$ and $\mathbb{P}_1$ finite elements, respectively. Since we noticed from the literature review that the published numerical simulations required considerable high computer resources and CPU time, the main feature of our numerical method was the use of a mesh adaptivity algorithm using metrics control to adapt the mesh every time step. We concentrated the grid refinement effort only in regions displaying high gradients of the computed variables, and prescribed coarser meshes in the solid phase and stagnant regions. This reduced considerably the number of degrees of liberty, while keeping high accuracy. The accuracy of the numerical method was tested using manufactured solutions: the expected second-order accuracy in both space and time was obtained.

As a first purpose of the study, we organized the programs as a toolbox for the software FreeFem++. The toolbox was designed to be an easy-to-use tool to handle phase-change problems. All technical issues related to the implementation of the finite element method were hidden, allowing to focus on numerical algorithms and their performance. A sequence of validation tests was performed, and presented by increasing gradually the level of complexity. Using the provided examples, the user could implement easily similar problems involving phase-change phenomena.

We first tested the capability of the Navier-Stokes solver to deal with natural convection problems, without enthalpy and porosity terms in the system of equations. We started by simulating the natural convection of air and water inside differentially heated square enclosures. We validated our results against classical benchmarks of natural convection. Rayleigh numbers up to 10^8, at the limit of the steadiness for the natural convection of air, were considered. Additionally, we investigated the thermal driven problem including a heated obstacle, to assess for the robustness of the code.

We also computed the natural convection of water, which implies a non-linear variation of the density in the expression of the buoyancy force. The comparison with existing numerical data in the literature showed very good agreement. The mesh adaptivity algorithm proved very efficient, allowing to capture accurately the anomalous variation of the density around $T = 4\,^oC$. For all simulations presented in the framework of natural convection problems, the steady state regimes were reached at most after 50 CPU seconds of computation.

We validated extensively the code by simulating the problem of melting and solidification of a PCM.

To compare our simulation with available experimental and numerical results in the literature, we first considered the melting of n-octadecane and Gallium inside vertically heated rectangular enclosures. A mesh convergence test was performed to ensure the grid-convergence of the solution.

Three Rayleigh numbers ranging from 10^5 to 10^8 were considered for the n-octadecane PCM melting. Our simulations were compared with three different benchmarks. A good agreement was found for the comparison with existing experimental and numerical results. Concerning the controversial melting of Gallium in 2D configurations, our simulations showed multi-cellular structures of the melted flow and highly oscillating values of the Nusselt number, in agreement with many observations from the literature.

We also simulated complex geometries, such as highly distorted domain or cylindrical PCM including inner heated pipes. For all considered cases, a variable mesh in the vicinity of the walls and along the phase-change front ensured a good capture of the boundary layer region and the location of the interface. The simulation of the melting of Gallium showed that our simulations run 245 times faster when compared with the simulations of Hannoun et al. (2003).

We finally presented the challenging case of water freezing inside a differentially heated cavity. A qualitative agreement with the experimental results for the solidification front was obtained. The efficiency of our numerical algorithm allowed us to perform simulations for melting problems, within 45 minutes for the lowest value of $\mathcal{R}a$ to 5 hours for $\mathcal{R}a = 10^8$. After a thorough investigation, we could conclude that our numerical method was validated for the natural convection of air and water and for the solid-liquid phase change problems including melting and solidification by providing a good agreement with the benchmarks presented in the literature.

The second purpose of the study was to provide a thorough analysis of the melting and the solidification process and compare with numerical results.

We first compared the behavior of the melting PCM when the latter is subject to heating from the side or from below (lateral or basal melting). For the lateral melting case, we assessed on the influence of the Rayleigh number on the heat transfer, by computing several configurations using different values of H and δT. It was shown that increasing the Rayleigh number by keeping δT constant induces a slower melting rate and a higher heat transfer. However, increasing both Rayleigh and Stefan numbers induced an earlier onset of the convection-dominated regime, improving thus the efficiency of the PCM.

For the basal melting case, we developed a scale analysis for the linear regime and provided a comprehensive description of the heat transfer processes during the melting process. Differences between lateral and basal melting were drawn, mainly for the structure of the flow and the time evolution of the Nusselt number. A mono-cellular flow was observed for the lateral melting case at any investigated Rayleigh numbers, while natural convection developed in the form of Bénard cells for the basal melting case. Moreover, the quasi-steady evolution of $\mathcal{N}u$ for the vertical heating is not observed when the PCM is heated from below, since high oscillating evolutions were exhibited.

Further investigation of the solidification process was done by simulating alternate melting and solidification cycles. Solidification after either complete or partial melting was simulated, with an assessment of the melting rate, the heat transfer and the accumulated heat input. It was observed that the convective heat transfer dominated the melting process, enhancing thus the heat transfer. Conduction was the main heat transfer mode during the solidification, resulting into a slower operating process. However, when the discharge temperature was decreased by a factor of 5, the solidification and the melting occur over similar time intervals. The challenging task for the mesh adaptivity procedure was to track the two moving interfaces during the solidification cycle.

The third purpose of the thesis was to expand the numerical simulation to 3D configurations. Parallel

3D tools for melting or solidification involving natural convection flows, using domain decomposition methods were presented. Numerical simulations were carried out using the recent library `ffddm` in FreeFem++ . The originality of our numerical approach was the use of 3D adaptive meshes, performed every time step, using *mmg3d* library. We used *Metis* library to split the domain into subdomains. The linear system of equations resulting from the Newton linearization was solved using parallel *GMRES* Krylov methods.

We simulated the natural convection of air and water inside cubic enclosures and found good agreement with classical benchmarks. We also simulated the melting of n-octadecane PCM and the difficult case of water freezing inside a differentially heated cubic cavity. The influence of the three-dimensional effects on the flow, that was neglected in 2D simulations, was highlighted by presenting the 3D shape of the solid-liquid interface. Iso-surfaces of the temperature were also impacted by the secondary flow in the vicinity of the side walls. The adaptive 3D mesh procedure proved very efficient to capture several interfaces, as in the case of the water freezing.

Future work

One of the major limitations of the present physical model is that we neglected the undercooling phenomenon, since we assumed that the temperature of fusion and the temperature of solidification were the same. Though, the liquid could solidify at a temperature significantly lower than the melting temperature, because of a problem of nucleation at the microscopic scale. An enthalpy-based formulation of the enthalpy-porosity model should be implemented to this end, since the undercooling problem can not be implemented in the current temperature-based approach. Additionally, a microsegregation model and a coupling relation between thermal and solute equations could be implemented in the code, in order to be able to simulate solidification or melting of binary mixtures. Such models would allow us to simulate more complex configurations such as dendritic formations during the solidification process.

While the Boussinesq approximation proved to be robust for the considered configuration in this study, the assumption of constant thermo-physical properties limits the range of materials that could be simulated by our code. A variable density code could be a valuable tool to investigate a larger type of PCMs and more industrial configurations.

Concerning the numerical model, the second order GEAR scheme provided accurate solutions for all the considered simulations. Furthermore, a variable time step scheme would increase the robustness of the numerical method. The simulation of the melting PCM requires for example a very small time step during the initialization stage, while larger time steps could be prescribed later in the simulation. Adapting automatically this procedure will increase considerably the efficiency of the code. For the solidification problem, new boundary conditions could be further developed by using some models that take into account realistic boundary conditions.

For the parallel algorithm, other preconditionners and solvers should be investigated. This is not a difficult task with FreeFem++ , since the software is interfaced with popular MUMPS, PETSc, or HPDDM solvers.

Bibliography

F. Agyenim, N. Hewitt, P. Eames and M. Smyth. A review of materials, heat transfer and phase change problem formulation for latent heat thermal energy storage systems (LHTESS). *Renewable and sustainable energy reviews*, 14(2):615–628, 2010.

R. Aldbaissy, F. Hecht, G. Mansour and T. Sayah. A full discretisation of the time-dependent Boussinesq (buoyancy) model with nonlinear viscosity. *Calcolo*, 55(4):44, 2018.

P. Angot, C.-H. Bruneau and P. Fabrie. A penalization method to take into account obstacles in incompressible viscous flows. *Numer. Math.*, 81(4):497–520, 1999.

F. Ascione, N. Bianco, R. F. De Masi, F. de Rossi and G. P. Vanoli. Energy refurbishment of existing buildings through the use of phase change materials: Energy savings and indoor comfort in the cooling season. *Applied Energy*, 113:990–1007, 2014.

S. N. Atluri and S. Shen. *The meshless local Petrov-Galerkin (MLPG) method*. Crest, 2002.

C. Barreneche, L. Navarro, A. de Gracia, A. I. Fernández and L. F. Cabeza. In situ thermal and acoustic performance and environmental impact of the introduction of a shape-stabilized PCM layer for building applications. *Renewable energy*, 85:281–286, 2016.

A. Bejan. Analysis of melting by natural convection in an enclosure. *International Journal of Heat and Fluid Flow*, 10(3):245–252, 1989.

A. Bejan. *Convection heat transfer*. John Wiley & sons, 2013.

Y. Belhamadia, A. Fortin and E. Chamberland. Anisotropic mesh adaptation for the solution of the Stefan problem. *Journal of Computational Physics*, 194(1):233–255, 2004a.

Y. Belhamadia, A. Fortin and E. Chamberland. Three-dimensional anisotropic mesh adaptation for phase change problems. *Journal of Computational Physics*, 201(2):753–770, 2004b.

Y. Belhamadia, A. S. Kane and A. Fortin. An enhanced mathematical model for phase change problems with natural convection. *International Journal of Numerical Analysis and Modeling*, 3(2):192–206, 2012.

O. Bertrand, B. Binet, H. Combeau, S. Couturier, Y. Delannoy, D. Gobin, M. Lacroix, P. Le Quéré, M. Médale, J. Mencinger et al. Melting driven by natural convection A comparison exercise: first results. *International Journal of Thermal Sciences*, 38(1):5–26, 1999.

A. Bhattacharya, A. Kiran, S. Karagadde and P. Dutta. An enthalpy method for modeling eutectic solidification. *Journal of Computational Physics*, 262:217–230, 2014.

W. J. Boettinger, J. A. Warren, C. Beckermann and A. Karma. Phase-field simulation of solidification. *Annual review of materials research*, 32(1):163–194, 2002.

H. Borouchaki, M. J. Castro-Diaz, P. L. George, F. Hecht and B. Mohammadi. Anisotropic adaptive mesh generation in two dimensions for CFD. In *5th Inter. Conf. on Numerical Grid Generation in Computational Field Simulations*. Mississipi State Univ., 1996.

G. Brandeis and B. D. Marsh. The convective liquidus in a solidifying magma chamber: a fluid dynamic investigation. *Nature*, 339(6226):613, 1989.

A. D. Brent, V. R. Voller and K. J. Reid. Enthalpy-porosity technique for modeling convection-diffusion phase change: Application to the melting of a pure metal. *Numerical Heat Transfer*, 13:297–318, 1988.

Y. Cao and A. Faghri. A numerical analysis of phase change problem including natural convection. *ASME Journal of Heat Transfer*, 112:812–815, 1990.

Y. Cao, A. Faghri and W. S. Chang. A numerical analysis of Stefan problems for generalized multi-dimensional phase-change structures using the enthalpy transforming model. *International Journal of Heat and Mass Transfer*, 32(7):1289–1298, 1989.

M. Castro-Diaz, F. Hecht and B. Mohammadi. Anisotropic Grid Adaptation for Inviscid and Viscous Flows Simulations. *Int. J. Numer. Methods Fluids*, 25:475–491, 2000.

M. M. Cerimele, D. Mansutti and F. Pistella. Numerical modelling of liquid/solid phase transitions: Analysis of a gallium melting test. *Computers & fluids*, 31(4):437–451, 2002.

C. Chabot and L. Gosselin. Solid-liquid phase change around a tube with periodic heating and cooling: Scale analysis, numerical simulations and correlations. *International Journal of Thermal Sciences*, 112:345–357, 2017.

S. Chandrasekhar. *Hydrodynamic and hydromagnetic stability*. Courier Corporation, 2013.

F. M. Chiesa and R. I. L. Guthrie. Natural convective heat transfer rates during the solidification and melting of metals and alloy systems. *Journal of Heat Transfer*, 96(3):377–384, 1974.

I. Danaila and F. Hecht. A finite element method with mesh adaptivity for computing vortex states in fast-rotating Bose-Einstein condensates. *J. Comput. Physics*, 229:6946–6960, 2010.

I. Danaila, R. Moglan, F. Hecht and S. Le Masson. A Newton method with adaptive finite elements for solving phase-change problems with natural convection. *J. Comput. Physics*, 274:826–840, 2014.

J. A. Dantzig. Modelling liquid–solid phase changes with melt convection. *International Journal for Numerical Methods in Engineering*, 28(8):1769–1785, 1989.

A. Davaille and C. Jaupart. Thermal convection in lava lakes. *Geophysical Research Letters*, 20(17): 1827–1830, 1993.

G. de Vahl Davis. Natural convection of air in a square cavity: a benchmark numerical solution. *International Journal for numerical methods in fluids*, 3(3):249–264, 1983.

L. A. Diaz and R. Viskanta. Visualization of the solid-liquid interface morphology formed by natural convection during melting of a solid from below. *International Communications in Heat and Mass Transfer*, 11(1):35–43, 1984.

C. Dobrzynski. *MMG3D: User Guide*. Technical Report RT-0422, INRIA, March 2012. URL https://hal.inria.fr/hal-00681813.

B. Dudley. BP statistical review of world energy 2016. *London, UK*, 2018.

C. M. Elliott. Error analysis of the enthalpy method for the Stefan problem. *IMA journal of numerical analysis*, 7(1):61–71, 1987.

B. R. Esfahani, S. C. Hirata, S. Berti and E. Calzavarini. Basal melting driven by turbulent thermal convection. *Physical Review Fluids*, 3(5):053501, 2018.

N.R. Eyres, D. R. Hartree, J. Ingham, R. J. Sarjant, J. B. Wagstaff et al. The calculation of variable heat flow in solids. *Phil. Trans. R. Soc. Lond. A*, 240(813):1–57, 1946.

M. Fabbri and V. R. Voller. The phase-field method in the sharp interface limit: a comparison between model potential. *Journal of Computational Physics*, 130:256–265, 1997.

B. Favier, J. Purseed and L. Duchemin. Rayleigh–Bénard convection with a melting boundary. *Journal of Fluid Mechanics*, 858:437–473, 2019.

P. J. Frey and P. L. George. *Maillages*. Hermès, Paris, 1999.

D.K. Gartling. Finite element analysis of convective heat transfer problems with change of phase. In K. Morgan, C. Taylor and C.A. Brebbia, editors, *Computer Methods in Fluids*, pages 257–284. Pentech, London, 1980.

C. Gau and R. Viskanta. Melting and solidification of a metal system in a rectangular cavity. *International Journal of Heat and Mass Transfer*, 27(1):113–123, 1984.

C. Gau, R. Viskanta and C-J. Ho. Flow visualization during solid-liquid phase change heat transfer II. Melting in a rectangular cavity. *International Communications in Heat and Mass Transfer*, 10(3): 183–190, 1983.

B. Gebhart and J.C. Mollendorf. A new density relation for pure and saline water. *Deep Sea Res.*, 24: 831–848, 1977.

P. L. George and H. Borouchaki. *Delaunay triangulation and meshing*. Hermès, Paris, 1998.

F. Giangi and M. Stella. Melting of a pure metal on a vertical wall: numerical simulation. *Numerical Heat Transfer: Part A: Applications*, 38(2):193–208, 2000.

M. Giangi, T. A. Kowalewski, F. Stella and E. Leonardi. Natural convection during ice formation: numerical simulation vs. experimental results. *Computer Assisted Mechanics and Engineering Sciences*, 7:321–342, 2000.

V. Girault and P.-A. Raviart. *Finite element methods for Navier-Stokes equations*. Springer Verlag, Berlin, 1986.

D. Gobin and P. Le Quéré. Melting from an isothermal vertical wall. Synthesis of numerical comparison exercise. *Computer Assisted Mechanics and Engineering Sciences*, 7(3):289–306, 2000.

W. Gong, K. Johannes and F. Kuznik. Numerical simulation of melting with natural convection based on lattice Boltzmann method and performed with CUDA enabled GPU. *Communications in Computational Physics*, 17(5):1201–1224, 2015.

Z-X. Gong and A. S. Mujumdar. Flow and heat transfer in convection-dominated melting in a rectangular cavity heated from below. *International Journal of Heat and Mass Transfer*, 41(17):2573–2580, 1998.

S. Grossmann and D. Lohse. Scaling in thermal convection: a unifying theory. *Journal of Fluid Mechanics*, 407:27–56, 2000.

S. C. Gupta. A moving grid numerical scheme for multi-dimensional solidification with transition temperature range. *Computer methods in applied mechanics and engineering*, 189(2):525–544, 2000.

J. N. W. Hale and R. Viskanta. Solid-liquid phase-change heat transfer and interface motion in materials cooled or heated from above or below. *International Journal of Heat and Mass Transfer*, 23(3):283–292, 1980.

N. Hannoun, V. Alexiades and T. Z. Mai. Resolving the controversy over tin and gallium melting in a rectangular cavity heated from the side. *Numerical Heat Transfer: Part B: Fundamentals*, 44(3): 253–276, 2003.

N. Hannoun, V. Alexiades and T. Z. Mai. A reference solution for phase change with convection. *International Journal for Numerical Methods in Fluids*, 48(11):1283–1308, 2005.

F. Hecht. New developments in Freefem++. *Journal of Numerical Mathematics*, 20:251–266, 2012.

F. Hecht and B. Mohammadi. Mesh Adaptation by Metric Control for Multi-scale Phenomena and Turbulence. *AIAA paper*, 97:0859, 1997.

F. Hecht, O. Pironneau, A. Le Hyaric and K. Ohtsuke. *FreeFem++ (manual)*. www.freefem.org, 2007.

C. J. Ho and C. H. Chu. Periodic melting within a square enclosure with an oscillatory surface temperature. *International journal of heat and mass transfer*, 36(3):725–733, 1993.

C-J. Ho and R. Viskanta. Inward solid-liquid phase-change heat transfer in a rectangular cavity with conducting vertical walls. *International journal of heat and mass transfer*, 27(7):1055–1065, 1984.

M. J. Hosseini, M. Rahimi and R. Bahrampoury. Experimental and computational evolution of a shell and tube heat exchanger as a PCM thermal storage system. *International Communications in Heat and Mass Transfer*, 50:128–136, 2014.

P. Jany and A. Bejan. Scaling theory of melting with natural convection in an enclosure. *International Journal of Heat and Mass Transfer*, 31(6):1221–1235, 1988.

S. Kalnæs and B. Jelle. Phase change materials and products for building applications: a state-of-the-art review and future research opportunities. *Energy and Buildings*, 94:150–176, 2015.

A. C. Kheirabadi and D. Groulx. The Effect of the Mushy-Zone Constant on Simulated Phase Change Heat Transfer. In *Proceedings of CHT-15, ICHMT International Symposium on Advances in Computational Heat Transfer, Ichmt Digital Library Online*. Begel House Inc., 2015.

A. König-Haagen, E. Franquet, E. Pernot and D. Brüggemann. A comprehensive benchmark of fixed-grid methods for the modeling of melting. *International Journal of Thermal Sciences*, 118:69–103, 2017.

T. Kousksou, M. Mahdaoui, A. Ahmed and A. A. Msaad. Melting over a wavy surface in a rectangular cavity heated from below. *Energy*, 64:212–219, 2014.

A. Kowalewski and D. Gobin. *Phase change with convection: modelling and validation*. Springer, 2004.

T. A. Kowalewski and M. Rebow. Freezing of water in differentially heated cubic cavity. *International Journal of Computational Fluid Dynamics*, 11:193–210, 1999.

S. Laizet and E. Lamballais. High–order compact schemes for incompressible flows: A simple and efficient method with quasi–spectral accuracy. *Journal of Computational Physics*, 228(16):5989–6015, 2009.

G. Lamé and B. P. Clapeyron. Mémoire sur la solidification par refroidissement d'un globe liquide. In *Annales Chimie Physique*, volume 47, pages 250–256, 1831.

P. Le Queré. Accuratte solutions to the square thermally driven cavity at high Rayleigh number. *Computational Fluids*, 20:24–41, 1991.

P. Le Quéré and M. Behnia. From onset of unsteadiness to chaos in a differentially heated square cavity. *Journal of fluid mechanics*, 359:81–107, 1998.

P. Le Quéré and T. A. De Roquefortt. Computation of natural convection in two-dimensional cavities with Chebyshev polynomials. *Journal of Computational Physics*, 57(2):210–228, 1985.

P. Le Quéré and D. Gobin. A note on possible flow instabilities in melting from the side. *International journal of thermal sciences*, 38(7):595–600, 1999.

C.H. Li. A finite-element front-tracking enthalpy method for Stefan Problems. *IMA Journal of Numerical Analysis*, 3:87–107, 1983.

C. Liu and D. Groulx. Experimental study of the phase change heat transfer inside a horizontal cylindrical latent heat energy storage system. *International Journal of Thermal Sciences*, 82:100–110, 2014.

K. Luo, F-J. Yao, H-L. Yi and H-P. Tan. Lattice Boltzmann simulation of convection melting in complex heat storage systems filled with phase change materials. *Applied Thermal Engineering*, 86: 238–250, 2015.

Z. Ma and Y. Zhang. Solid velocity correction schemes for a temperature transforming model for convection phase change. *International Journal For Numerical Methods Heat Fluid Flow*, 16(11): 204–225, 2006.

S. Madruga and J. Curbelo. Dynamic of plumes and scaling during the melting of a Phase Change Material heated from below. *International Journal of Heat and Mass Transfer*, 126:206–220, 2018.

W. V. R. Malkus. The heat transport and spectrum of thermal turbulence. *Proceedings of the Royal Society of London. Series A. Mathematical and Physical Sciences*, 225(1161):196–212, 1954.

K. Mathura and D. J. Krishna. Influence of Mushy Zone Constant on Thermohydraulics of a PCM. *Energy Procedia*, 109:314 – 321, 2017. International Conference on Recent Advancement in Air Conditioning and Refrigeration, RAAR 2016, 10-12 November 2016, Bhubaneswar, India.

T. Michalek, A. T. Kowalewski and B. Sarler. Natural convection for anomalous density variation of water: numerical benchmark. *Progress in Computational Fluid Dynamics, an International Journal*, 5(3-5):158–170, 2005.

T. Michalek and T. A. Kowalewski. Simulations of the water freezing process - Numerical benchmarks. *Task Quarterly*, 7(3):389–408, 2003.

Ministère de la transition écologique et solidaire. Chiffres clés de l'énergie, édition 2018. *Service de la donnée et des études statistiques*, 2018.

R. Moglan. *Modeling and numerical simulation of flow and heat phenomena in a telecommunication outdoor cabinet*. PhD thesis, Université de Rouen Normandie, 2013.

B. Mohammadi and O. Pironneau. *Applied Shape Design for Fluids*. Oxford Univ. Press, 2000.

K. Morgan, R. Lewis and O. Zienkiewicz. An improved algrorithm for heat conduction problems with phase change. *International Journal for Numerical Methods in Engineering*, 12:1191–1195, 1978.

K. Wittigand P. A. Nikrityuk. Three-dimensionality of fluid flow in the benchmark experiment for a pure metal melting on a vertical wall. In *IOP Conference Series: Materials Science and Engineering*, volume 27, page 012054. IOP Publishing, 2012.

R. Nourgaliev, H. Luo, B. Weston, A. Anderson, S. Schofield, T. Dunn and J-P. Delplanque. Fully-implicit orthogonal reconstructed Discontinuous Galerkin method for fluid dynamics with phase change. *Journal of Computational Physics*, 305:964–996, 2016.

M. Okada. Analysis of heat transfer during melting from a vertical wall. *International Journal of Heat and Mass Transfer*, 27:2057–2066, 1984.

A. P. Omojaro and C. Breitkopf. Study on solid liquid interface heat transfer of PCM under simultaneous charging and discharging (SCD) in horizontal cylinder annulus. *Heat and Mass Transfer*, 53 (7):2223–2240, 2017.

O. Pironneau, J. Liou and T. Tezduyar. Characteristic-Galerkin and Galerkin/least-squares space-time formulations for the advection-diffusion equations with time-dependent domains. *Comput. Methods Appl. Mech. Engrg.*, 100:117–141, 1992.

C. Polashenski, D. Perovich and Z. Courville. The mechanisms of sea ice melt pond formation and evolution. *Journal of Geophysical Research: Oceans*, 117(C1), 2012.

A. Quarteroni and A. Valli. *Numerical Approximation of Partial Differential Equations*. Springer-Verlag, Berlin and Heidelberg, 1994.

M. A. Rady and A. K. Mohanty. Natural convection during melting and solidification of pure metals in a cavity. *Numerical Heat Transfer, Part A Applications*, 29(1):49–63, 1996.

A. Rakotondrandisa, I. Danaila and L. Danaila. Numerical modelling of a melting-solidification cycle of a phase-change material with complete or partial melting. *International Journal of Heat and Fluid Flow*, 76:57–71, 2019.

P. J. Roache. *Verification and Validation in Computational Science and Engineering*. Hermosa Publishers, 1998.

M. E. Rose. A method for calculating solutions of parabolic equations with a free boundary. *Mathematics of Computation*, pages 249–256, 1960.

L. Rubinstein. On the solution of Stefan's problem. *Bull. Acad. Sci. URSS. Sér. Géograph. Géophys.(Izvestia Akad. Nauk SSSR)*, 11:37–54, 1947.

T. J. Scanlon and M. T. Stickland. A numerical analysis of buoyancy-driven melting and freezing. *International Journal of Heat and Mass Transfer*, 47:429–436, 2004.

T. M. Shih, C. H. Tan and B. C. Hwang. Effect of grid staggering on numerical schemes. *International Journal for Numerical Methods in Fluids*, 9(2):193–212, 1989.

W. Shyy, H.S. Udaykurnar, M. M. Rao and R.W. Smith. *Computational fluid dynamics with moving boundaries*. Taylor & Francis, 1996.

I. Singer-Loginova and H. M. Singer. The phase field technique for modeling multiphase materials. *Reports on progress in physics*, 71(10):106501, 2008.

E. M. Sparrow, P. V. Patankar and S. Ramadhyani. Analysis of melting in the presence of natural convection in the melt region. *Journal of Heat Transfer*, 99(4):520–526, 1977.

J. Stefan. Uber einige probleme der theorie der warmeletung. *Sitzer. Wien. Akad. Math. Naturw.*, 98: 473–484, 1889.

J. Stefan. Über die Theorie der Eisbildung, insbesondere über die Eisbildung im Polarmeere. *Annalen der Physik*, 278(2):269–286, 1891.

F. Stella and M. Giangi. Modelling Methodologies for Convection-Diffusion Phase-Change Problems. In A. Kowalewski and D. Gobin, editors, *Phase change with convection: modelling and validation*, pages 219–272. Springer, 2004.

C. R. Swaminathan and V. R. Voller. Towards a general numerical scheme for solidification systems. *International journal of heat and mass transfer*, 40(12):2859–2868, 1997.

R. Temam. *Navier-Stokes equations and nonlinear functional analysis*. SIAM, Philadelphia, 1983.

R. T. Tenchev, J. A. Mackenzie, T. J. Scanlon and M. T. Stickland. Finite element moving mesh analysis of phase change problems with natural convection. *International Journal of Heat and Fluid Flow*, 26(4):597–612, 2005.

S. O. Unverdi and G. Tryggvason. A front-tracking method for viscous incompressible, multifluid flows. *Journal of Computational Physics*, 100:25–37, 1992.

G. M. Vasil and M. R. E. Proctor. Dynamic bifurcations and pattern formation in melting-boundary convection. *Journal of Fluid Mechanics*, 686:77–108, 2011.

G. Vergez, I. Danaila, S. Auliac and F. Hecht. A finite-element toolbox for the stationary Gross-Pitaevskii equation with rotation. *Comput. Phys. Comm.*, 209:144–162, 2016.

R. Viskanta. Natural convection in melting and solidification. *Natural Convection: Fundamentals and Applications*, pages 845–877, 1985.

V. R. Voller. An overview of numerical methods for solving phase change problems. In W. J. Minkowycz and E. M. Sparrow, editors, *Advances in Numerical Heat Transfer*, pages 341–375. Taylor & Francis, 1996.

V. R. Voller, M. Cross and N. C. Markatos. An enthalpy method for convection/diffusion phase change. *Int. J. Numer. Meth. Eng.*, 24:271–284, 1987.

V. R. Voller, P. Felix and C. R. Swaminathan. Cyclic phase change with fluid flow. *Int. Journ. of Num. Methods for Heat and Fluid Flow*, 6:57–64, 1996.

V. R. Voller and C. Prakash. A fixed grid numerical modelling methodology for convection-diffusion mushy region phase-change problems. *International Journal of Heat and Mass Transfer*, 30:1709–1719, 1987.

S. Wakashima and T.S. Saitoh. Benchmark solutions for natural convection in a cubic cavity using the high–order time–space method. *International Journal of Heat and Mass Transfer*, 47(4):853 – 864, 2004.

S. Wang, A. Faghri and T. L. Bergman. A comprehensive numerical model for melting with natural convection. *International Journal of Heat and Mass Transfer*, 53:1986–2000, 2010a.

S. Wang, A. Faghri and T. L. Bergman. Numerical modeling of alternate melting and solidification. *Numerical Heat Transfer, Part B: Fundamentals*, 58(6):393–418, 2010b.

J. Woodfield, M. Alvarez, B. Gamez-Vargas and R. Ruiz-Baier. Stability and finite element approximation of phase change models for natural convection in porous media. *Journal of Computational and Applied Mathematics*, 360:117 – 137, 2019.

L. S. Yao and J. Prusa. Melting and freezing. In *Advances in Heat transfer*, volume 19, pages 1–95. Elsevier, 1989.

Y. Zhang and I. Danaila. Existence and numerical modelling of vortex rings with elliptic boundaries. *Applied Mathematical Modelling*, 37:4809–4824, 2013.

N. Zhu, Z. Ma and S. Wang. Dynamic characteristics and energy performance of buildings using phase change materials: a review. *Energy Conversion and Management*, 50(12):3169–3181, 2009.

A.G. Zimmerman and J. Kowalski. Monolithic Simulation of Convection-Coupled Phase-Change: Verification and Reproducibility. In M. Schäfer, M. Behr, M. Mehl and B. Wohlmuth, editors, *Recent Advances in Computational Engineering. ICCE 2017. Lecture Notes in Computational Science and Engineering, vol 124*, pages 177–197. Springer, 2018.

Résumé

Nous développons dans ce travail de thèse un outil de simulation numérique pour les matériaux à changement de phase (MCP), en tenant compte du phénomène de convection naturelle dans la phase liquide, pour des configurations en deux et trois dimensions. Les équations de Navier-Stokes incompressible avec le modèle de Boussinesq pour la prise en compte des forces de flottabilité liées aux effets thermiques, couplées avec une formulation de l'équation d'énergie suivant la méthode d'enthalpie, sont résolues par une de méthode d'éléments finis adaptatifs. Une approche mono-domaine, consistant à résoudre les mêmes systèmes d'équations dans les phases solide et liquide, est utilisée. La vitesse est ramenée à zéro dans la phase solide, en introduisant un terme de pénalisation dans l'équation de quantité de mouvement, suivant le modèle de Carman-Kozeny, consistant à freiner la vitesse à travers un milieu poreux. Une discrétisation spatiale des équations utilisant des éléments finis de Taylor-Hood, éléments finis P2 pour la vitesse et éléments finis P1 pour la pression, est appliquée, avec un schéma d'intégration en temps implicite d'ordre deux (GEAR). Le sytème d'équations non-linéaires est résolu par un algorithme de Newton. Les méthodes numériques sont implémentées avec le logiciel libre FreeFem++ (www.freefem.org), disponible pour tout système d'exploitation. Les programmes sont distribués sous forme de logiciel libre, sous la forme d'une forme de toolbox simple d'utilisation, permettant à l'utilisateur de rajouter d'autres configurations numériques pour des problèmes avec changement de phase. Nous présentons dans ce manuscrit des cas de validation du code de calcul, en simulant des cas tests bien connus, présentés par ordre de difficulté croissant : convection naturelle de l'air, fusion d'un MCP, le cycle complet fusion-solidification, chauffage par le bas d'un MCP, et enfin, la solidification de l'eau.

Mots-clefs : Navier-Stokes, Boussinesq, méthode d'enthalpie mono-domaine, Carman-Kozeny, éléments finis, FreeFem++, maillage adaptatif, matériaux à changement de phase (MCP), convection naturelle, algorithme de Newton, fusion, cycle complet, solidification de l'eau.

Abstract

In this thesis we develop a numerical simulation tool for computing two and three-dimensional liquid-solid phase-change systems involving natural convection. It consists of solving the incompressible Navier-Stokes equations with Boussinesq approximation for thermal effects combined with an enthalpy-porosity method for the phase-change modeling, using a finite elements method with mesh adaptivity. A single-domain approach is applied by solving the same set of equations over the whole domain. A Carman-Kozeny-type penalty term is added to the momentum equation to bring to zero the velocity in the solid phase through an artificial mushy region. Model equations are discretized using Galerkin triangular finite elements. Piecewise quadratic (P2) finite-elements are used for the velocity and piecewise linear (P1) for the pressure. The coupled system of equations is integrated in time using a second-order Gear scheme. Non-linearities are treated implicitly and the resulting discrete equations are solved using a Newton algorithm. The numerical method is implemented with the finite elements software FreeFem++ (www.freefem.org), available for all existing operating systems. The programs are written and distributed as an easy-to-use open-source toolbox, allowing the user to code new numerical algorithms for similar problems with phase-change. We present several validations, by simulating classical benchmark cases of increasing difficulty: natural convection of air, melting of a phase-change material, a melting-solidification cycle, a basal melting of a phase-change material, and finally, a water freezing case.

Keywords : Navier-Stokes, Boussinesq, enthalpy-porosity method, single-domain method, Carman-Kozeny, finite-elements, Taylor-Hood, FreeFem++, mesh adaptivity, phase-change materials (PCM), natural convection, Newton algorithm, GEAR scheme, open-source toolbox, 2D and 3D simulations, melting, solidification, water freezing.